Dissertation

submitted to the

Combined Faculty of Mathematics, Engineering and Natural Sciences

of Heidelberg University, Germany

for the degree of

Doctor of Natural Sciences

Put forward by

Dennis Derewjanko

born in: Simmern/Hunsrück

Oral examination: 04.12.2025

Morphology- and Delocalization-Based Charge Transport Simulations Combining Tight Binding Modelling and Kinetic Monte Carlo Simulations

Referees: Prof. Dr. Martijn Kemerink

Prof. Dr. Maurits Haverkort

Abstract

The inherent chemical and morphological richness and complexity of Organic Semiconductors make the detailed theoretical description almost impossible. This leads to the necessity of simulation-based approaches that should be as detailed and computationally efficient as possible, which turns out to be a far from trivial task. While over the decades, different models of different levels of detail and computational effort have been proposed, there is still ample room for improvement. In this thesis a semi-empirical Tight Binding model of organic semiconductors was developed that is based on user-specified morphologies like Molecular Dynamics morphologies and is combined with kinetic Monte Carlo simulations to obtain a tool that captures different correlations and includes partially delocalized charge carriers. In this thesis, kinetic Monte Carlo simulations are used to describe how anisotropic localization lengths can lead to increased thermoelectric powerfactors, breaking the usual trade-off between Seebeck coefficient and conductivity. The developed numerical model is also used to study the validity of the effective temperature model of the field dependence of the conductivity that assumes a one-to-one relation between thermal- and field-activated charge transport. It is found that the effective temperature model is not always self-consistent and breaks down for inhomogeneous systems. Additionally, other parameters influencing the field dependence are not correctly incorporated in the effective temperature model. The numerical model was also used to explain the experimentally observed superlinear increase of conductivity at high charge carrier concentrations. Delocalization of charges at the Fermi level is found to explain this observation. Lastly, the tight binding model was used to explain the renormalization of the Density of States at intermediate doping levels that is necessary to explain the experimentally observed roll-off in conductivity for intermediate doping in the conductivity dependence of the Seebeck coefficient which is the relevant regime for optimized thermoelectric devices.

Zusammenfassung

Die inhärente chemische und morphologische Vielfalt und Komplexität von Organischen Halbleitern machen deren detaillierte theoretische Beschreibung fast unmöglich. Dies führt zur Benötigung von simulationsbasierten Ansätzen, die so physikalisch exakt als auch numerisch effizient wie möglich sein sollten. Dies stellt sich jedoch als eine alles andere als triviale Aufgabe dar. Über die Jahrzehnte hinweg wurden unterschiedliche Modelle mit unterschiedlicher physikalischer Genauigkeit und Effizienz vorgestellt, jedoch existiert nach wie vor Verbesserungsbedarf. In dieser Thesis wird ein semi-empirisches Tight Binding Modell entwickelt, das auf benutzerspezifischen Morphologien wie Molekulardynamik Morphologien basiert und kombiniert mit kinetischen Monte Carlo Simulationen um ein Werkzeug zu erhalten, das unterschiedliche Korrelationen und teilweise delokalisierte Zustände erfassen kann. Zunächst werden kinetische Monte Carlo Simulationen benutzt um zu erklären wie anisotrope Lokalisierungslängen zu einem erhöhten thermoelektrischen Leistungsfaktor führen können und dabei den üblichen Zielkonflikt zwischen Seebeck Koeffizienten und Leitfähigkeit brechen können. Das entwickelte numerische Modell wird außerdem dazu benutzt, um die Gültigkeit des Modells der effektiven Temperatur für die Feldabhängigkeit der Leitfähigkeit zu studieren. Es zeigt sich, dass dieser Ansatz oft nicht selbstkonsistent ist und u.A. für inhomogene Systeme zusammenbricht. Zusätzlich werden andere physikalische Parameter, die die Feldabhängigkeit beeinflussen, offenbar nicht richtig in das Modell inkludiert. Das Modell wurde des Weiteren dazu verwendet um numerisch den experimentell beobachteten super-linearen Anstieg der Leitfähigkeit bei hohen Ladungsträgerkonzentrationen zu erklären. Dies wird erklärt durch die zusätzliche Delokalisierung von Ladungen bei der Fermi Energie. Zuletzt wird das entwickelte Tight Binding Modell dazu benutzt um die Renormalisierung der Zustandsdichte bei mittleren Doping Levels zu erklären, die nötig ist um den experimentell beobachteten Abfall der Leitfähigkeit im mittleren Doping Regime, dem für optimierte thermoelektrische Anwendungen relevantesten Regime, zu beschreiben.

Inhalt

Introduction

Motivation and State of Research

Organic Electronics is the scientific field of the general electronic properties of (in the chemical sense) organic materials like organic semiconductors or organic ferroelectrics. Its most prominent application is the organic light emitting diode (OLED) which the basis of the arguably currently best screen technology, built into virtually all modern smart phones. The field is in comparison to the physics of inorganic materials very young and had its beginning with the discovery of the first semiconducting material violanthrone by Akamatu and Inokuchi in the year 1950[1]. Unlike for inorganic materials, at this point the charge transport mechanism was completely unclear. Experiments and the inherently disordered nature of these organic materials hinted on Hopping-type conduction, which was originally found in amorphous inorganic materials, but the physically correct formalism was unclear. Around the same time, hopping theories for amorphous inorganic semiconductors were developed by Mott[2,3], Miller and Abrahams[4] and Marcus[5]. Only in the 80s and 90s, Bässler[6] formulated a consistent charge transport theory specifically for organic semiconductors (OSC) with the Gaussian Disorder Model (GDM). However, with the development of ever new OSCs the chemical and physical complexity of the vast material space of possible OSCs became clear. This is due its main constituent carbon, which can form four covalent bounds and almost arbitrarily big and complex structures, especially in connection with different hetero-atoms, making it not only chemically complex, but also from a morphological point of view. Different classifications of OSCs emerged, like small molecules or polymer based, crystalline, semicrystalline, and amorphous OSCs. With that amount of complexity, also the need for more sophisticated theories and models of charge transport (CT) arose. The very diverse microscopic and mesoscopic situation, especially the inherent disorder and therefore lack of symmetry in these materials however make it very hard to yet impossible to treat theoretically in detail, making the use of numerical simulation methods for their understanding and optimization very important. On a microscopic scale, the most important quantities to describe the CT are the electronic couplings between the molecular states like HOMO or LUMO (highest occupied molecular orbital and lowest unoccupied molecular orbital), the reorganization energy being

the energy needed to form a polaron during charge transfer and the chemical and electrostatic environment.

In the last two decades there has been great effort in accurately calculating electronic couplings (or also called transfer integral), reorganization energies and energy levels by different quantum chemical and semi-empirical calculations like Density Functional Theory (DFT), Constrained Density Functional Theory (CDFT), Fragment Orbital DFT (FODFT), Density Functional Tight Binding (DFTB), Generalized Mulliken–Hush (GMH), or Analytic Overlap Method (AOM) to accurately calculate Marcus hopping rates or Marcus-Levich-Jortner hopping rates. The rates are used together with Molecular Dynamics (MD) Morphologies or crystalline Morphologies to perform kinetic Monte Carlo (kMC) Simulations and calculate electronic Mobilities.

For example, Lukyanov and Andrienko [7] calculate transfer integrals directly with DFT and use them with the Marcus rate in kMC simulations on a MD generated morphology. Their approach is though strongly limited in system size because of the expensive direct DFT calculations, leading to dispersive mobilities. They therefore extrapolate the temperature dependence of the mobility to achieve non-dispersive mobilities.

Many other authors used similar approaches for their simulation[8–10]. For this standard multiscale workflow approach, a widely used toolkit named VOTCA[11] was created.

An interesting modulation of VOTCA was implemented from Rühle et al. [10,12], where transfer integrals were not calculated between monomers, but between rigid fragments of e.g. the investigated polymer morphology, which are determined by (not unique) conditions. Similarly, Mladenovic and Vukmirovic[13] performed multiscale simulations on P3HT using a fragmentation method they developed called Overlapping Fragments Method (OFM) [14] to better capture partially delocalized polymer fragments in their simulation.

E.D. Miller et al. [15] use a widely used semi-empirical quantum chemical calculation (ZINDO/S[16]) to calculate orbital energies of P3HT chromophores and approximate the transfer integral by Marcus-Hush two state approximation, which is the quadratic sum of HOMO and HOMO-1 difference and site energy difference, and use it with the Marcus rate to perform kMC simulations with snapshot MD generated morphology. They calculate Diffusion mobility with reasonable values and highlight the importance of tie chains in their morphologies.

Alkan and Yavuz[17] investigate the influence of Alkyl side chains on mobility. They use X-ray crystal structures as starting configuration for a MD simulation for a disordered morphology. They then calculate transfer integrals with ZINDO and site energies with the Thole Model as input for the Marcus Levich Jortner rate to perform kMC simulations and find small side chains lead to worse mobility in comparison to somewhat larger but not too large ones due to reduced electrostatic interactions and advantageous packing of the backbones for longer side chains.

Park et al.[18] studied grain boundary effects in poly-crystalline organic semiconductors generating static perfect OSC lattices and randomly reorienting the crystalline grains during kMC simulations. They extract energies and electronic couplings by DFT based quantum chemical calculations and use it within the Marcus rate for the kMC Simulations. They circumvent the computationally limited simulation box and grain size by a grain-size calibration formula based on AFM images.

For systems with significant dynamical disorder, where snapshot MD morphologies can underestimate its impact, Özdemir et al.[19] make use of the semi-empirical Density Functional Tight Binding (DFTB) to sample a large number of molecule pairs for HOMO energy and hole coupling calculations and consider the time dependence of electronic couplings due to dynamical disorder via time averaging of electronic properties that are used for the Marcus rate in kMC.

To overcome the computational limitations of expensive exact transfer integral calculations, Gajdos et al.[20,21] exploited the already older idea from e.g. Extended Hückel Theory or the Molecular Orbital Overlap (MOO) method that the transfer integrals are proportional to the orbital overlap to find a universal linear scaling law over a wide range of distances with a universal scaling constant for a given donor-acceptor system, reducing the computational effort to just overlap calculations. One can further speed up calculations by parametrizing the orbitals analytically to calculate the overlaps (Analytic Overlap Method). For this purpose, only the constant must be fitted to e.g. results from representative DFT simulations.

With the recent achievements in Machine learning another approach to tackle the limits of computational power won in popularity. Instead of the explicit expensive calculation of transfer integrals researches use Machine Learning techniques to predict transfer rates for larger systems to be able to simulate mesoscopic morphologies. For example, Tan et al.[22] use

this approach to perform multiscale simulations for organic thin films with grain boundaries and polymorphs.

Due to the computational difficulties of larger systems, many authors use their different methods on crystalline or slightly disordered morphologies, but also works exist that use these methods to try to get insight into more complex mesoscale morphologies like strained TIPS-P crystals[23], polycrystalline systems[18], semicrystalline P3HT[24], solution and vacuum deposited OLEDs[25], edge-on P3HT[26], however more or less limited in simulation box size.

Aforementioned previous works mostly focus on low charge carrier concentrations and investigate the field dependence and temperature dependence of the mobility or zero field mobilities, mostly with focus on small molecule organic semiconductors. The simulated box size is dependent on their calculation technique of electronic couplings compromising a bottle neck. More ab initio calculations can only perform on very small systems, whereas other semi-empirical approaches can cover larger systems with retaining mostly accurate couplings. Many of the authors work with snapshot morphologies, while some try to incorporate fluctuation in couplings due to dynamical disorder which can be relevant in small molecule and crystalline OSCs but less in polymeric OSC. However, in virtually all studies the effect of partial delocalization is not captured since Marcus theory is valid only for charge states localized on single monomers or single small molecules. Also, electronic couplings can be underestimated due to commonly used dimer approximation, where electronic couplings are calculated between HOMO frontier orbitals of two monomers. This fails to capture delocalization effects, since charge states often spread over multiple monomers, which leads to an artificial cutoff of the electronic couplings in the dimer approximation. However, this can't be resolved easily, since the calculation of electronic couplings in systems of several monomers is computationally extremely expensive and in addition the degrees of freedom to cover rises exponentially, making the problem even worse, such one is mostly stuck with the dimer approximation. For the transition to more delocalized states, other methods have been proposed and improved, but are still often computationally expensive to use in larger systems and only used in small systems or low dimensional problems.

One approach to try to bridge the problem of partially delocalized states, is delocalized kMC (dkMC)[27] introduced by Balzer et al.. They couple the electronic Hamiltonian to a thermal bath and perform a polar transformation to make the second order perturbative approach of

Secular Redfield Theory usable. It describes the time evolution of polaron populations with a rate equation. The specific rate, called Redfield tensor or rate can be seen as the hopping rate usable in kMC simulations, but requires repeated Hamiltonian diagonalizations and is still expensive albeit of several simplifications made. This method works in the range of hopping transport to transient localization, but so far can only utilize static simple or random lattices, which then again does not capture morphological effects.

A much simpler approach than dkMC by Willson et al.[28] named jumping kMC (jkMC) avoids the many expensive diagonalizations of Hamiltonians by just multiplying a delocalization correction term to the Marcus rate, which is determined by fitting a polaron delocalization radius to an ensemble average of spherical polaron state inverse participation ratios (IPRs). This method is much less expensive, but also works only on simple lattices and has not been combined with realistic morphologies.

In another approach e.g. Giannini et al.[29] or Spencer et al.[30] utilized AOM to develop a surface hopping method based on Fewest Switching Surfacing Hopping, where they expand the charge carrier wavefunction in a basis of fragment orbitals (here SOMOs) and propagating the coefficients using time dependent Schrödinger equation involving the need for repeated Hamiltonian matrix element calculations that can be efficiently calculated via AOM. According to the resulting time-dependent adiabatic electronic states, the decision to switch between two adiabatic surfaces during the simulation is then made probabilistically. This method (Fractal Orbital based Surface Hopping, FOB-SH) can capture a broader spectrum between band-like transport and hopping transport, is however still very computationally expensive for large or higher-dimensional systems.

Ishii et al.[31,32] developed yet another quantum dynamical method to simulate the (diffusion) mobility for partially delocalized states. Their time-dependent wave-packet diffusion (TD-WPD) method uses a time dependent Tight Binding Hamiltonian for the definition of the systems density operator, with which then the time-dependent diffusion coefficient as a velocity correlation function and finally the mobility via Einstein relation is calculated. This method however also suffers from high computational cost and was applied only for 2D systems as was FOB-SH.

Despite the great effort for high level mobility calculations made for OSC, multi-scale studies with focus on thermoelectric Simulations based on realistic Morphologies as done with

mobilities are rarer. Specific morphology-related kMC studies focus rather on random or simple lattice-like morphologies than realistic morphologies by MD, while others use a Boltzmann-Transport-Equation approach to calculate the Seebeck coefficient and use MD morphologies only for the thermal conductivity calculations.

For example, Zozoulenko et al.[33,34] used a multi-scale approach for PEDOT:ToS morphology from MD, calculated the transfer integrals using ZINDO and used Miller-Abrahams rate with the transfer integral as tunneling term for kMC simulations and thereby also simulated the Seebeck coefficient.

Recently Elsner et al.[35] performed thermoelectric transport simulations in organic molecular crystals using the FOB-SH method with physically and experimentally reasonable values for rubrene crystals, considering partial delocalization effects located in the regime of transient localization. Albeit being quite accurate, the method is as already said before currently computationally limited to small systems or two-dimensional lattices, making it hard to investigate polymeric systems or systems with more complex meso-scale morphology.

Goal of this Work

This thesis tries to bridge more sophisticated multi-scale simulations containing complex and expensive quantum chemical or semi-empirical calculations on MD based morphologies, but localized hopping, and simulation methods with the possibility of partial charge delocalization on simple lattice morphologies. I will thereby use modelled or Molecular Dynamics based morphologies and derive a semi-empirical Tight Binding Model of these morphologies which then serve together with a modified MA Transfer rate as input for kMC simulations. With this approach, electric and thermoelectric properties of a variety of morphologies considering partial delocalization effects can be simulated on a larger scale with comparatively limited computational cost.

I start by introducing OSCs and their morphologies and a description of them using Tight Binding theory. From there, energetical and localization properties will be derived and transferred to modified transfer rate to finally perform kMC simulations and investigate electrical and thermoelectrical properties of different systems with the prescribed scheme.

The investigated systems will cover anisotropic films, amorphous P3HT and different aggregated morphologies and also simple doped systems.

Theoretical Background and Methods

Organic Semiconductors

(Following[36] if not others stated). The class of Organic materials is defined by materials that mostly consist of bonds between carbon (C) atoms and carbon-hydrogen (C-H) bonds. Being in the fourth main group of the periodical system, carbon can form up to four covalent bonds. Allowing bonds with different heteroatoms (atoms that are not C or H), a vast material space can be constructed, containing highly functionalized molecules with very specific properties and abilities like proteins in living beings.

One can divide organic materials in many different categories ranging from small molecules over fullerenes to different kinds of conjugated polymers. The organic materials of concern in this thesis are medium to high molecular mass organic semiconductors (OSC). A central property of many OSCs of interest is the bond conjugation between C atoms, which can be nicely explained by orbital hybridization. Molecular orbitals are usually approximately described by solutions of the molecule's Schrödinger equation, obtained by inserting a linear combination of atomic orbitals (LCAO) as ansatz, in the Born-Oppenheimer approximation, where the electronic part is decoupled from the nuclidic part due to the inert nuclides in comparison to the much lighter electrons. The linear combination (therefore called orbital hybrids) of an s-orbital, p_x-orbital and an p_y-orbital (sp^2 hybridization) gives three planar covalent σ-bonds (bonds along the bond direction) of the C atoms. The fourth C-orbitals are out-of-plane formed by p_z and therefore form π-bonds (bonds perpendicular to the axis of bond direction). The charges in conjugated polymers are delocalized over the overlapping π-orbital system of the molecule. LCAO provides for every bonding state an anti-bonding state, denoted by a star after the bonding type, e.g. σ^* or π^* due to one symmetric and one antisymmetric solution. The electron density is for bonding states highest between the atoms, such that the Coulomb potential by the cores is screened and therefore the energy of the state is reduced. Anti-bonding states have a minimum between the atoms, are close to the cores, and have therefore higher energy.

A simple example of a conjugated polymer is an alkene chain of length N. Solving the corresponding N-π-electron Hamiltonian provides N energy levels that are symmetrically distributed around some fixed energy. At moderate temperatures the lowest N/2 states get

fully occupied in the ground state. The highest occupied state is called the HOMO (Highest Occupied Molecular Orbital), the i-th state below the HOMO is called HOMO-i. The lowest unoccupied orbital, being the first anti-bonding state, is called LUMO (Lowest Unoccupied Molecular Orbital), and i-th state above LUMO is called LUMO-i. The energy difference between the HOMO and the LUMO is called energy gap.

Due to the intrinsic disorder emerging from disorder in the chemical and energetic vicinity of individual molecules the HOMOs and LUMOs of the molecules will differ from each other, leading to not well-defined HOMOs and LUMOs for the bulk material, but rather to probabilistic distributions around some mean values. This disorder leads to hopping type of transport rather than band conduction, which will be discussed later.

Molecular Forces

Bonding Types

(See literature like Fließbach[37], Hunklinger[38]) One can categorize chemical bonds in materials as metallic, ionic and covalent bonds. Metallic bonds, as the name suggests, are found in metals and occur in atomic lattices of elements that have weakly bound valence electrons that can delocalize over ideally the whole lattice leading to an energetically lower and stable configuration.

Ionic bounds, often found in salts, occur when one atomic species donates one or more electrons to a different atom species such that they are found in ionized form as cations and anions. Those oppositely charged ions are then strongly and closely held together by the Coulomb interaction and form distinct regular (bravais) lattices. Opposing to metallic bonds, the electrons or holes are strictly localized on the ions.

However, as already covered in the previous chapter, the relevant intramolecular bonding type in OSCs is the covalent bonding. Covalent bonds are generally weaker than ionic bonds. For the bonding state, the electrons are not bound to one atom but shared between them and screen the coulombic interaction. This leads to a longer bonding length compared to ionic bonds and therefore more flexible molecular structures allowing for deformation like bending or torsion to some extent, depending on the geometry and size of the molecule.

Polar and Van der Waals Forces

Whereas the covalent bonds define the molecular structure, they do not form intermolecular bonds. Intermolecular bonds are formed by hydrogen bridges and dipole-dipole (or multipolar) interactions of partial charges, induced dipole – dipole interactions and van der Waals bonds (induced dipole – induced dipole).

A Hydrogen bridge is a directional dipole-dipole interaction between two strongly polar groups that occurs if hydrogen undergoes a covalent bond with a much more electro negative atom like oxygen. Due to the high electro negativity of the bonding partner, the bond electron gets pulled close to it, leaving hydrogen with a significant partial positive charge while the other gains a negative partial charge creating a strong polar group within the molecule. The hydrogen positive partial charge then aligns with the partial negative charge of another molecule forming the so-called hydrogen bridge.

Similarly, a general difference in electro negativity between atoms results in a non-uniform charge distribution along the bond resulting in dipoles or multipoles of partial charges across the molecule. The potential $\Phi(\boldsymbol{r})$ of a general charge distribution $\rho(\boldsymbol{r})$ can be Taylor expanded into a *Multipole expansion* (in Gauss units)

$$\Phi(\boldsymbol{r}) = \int d\boldsymbol{r}' \frac{\rho(\boldsymbol{r})}{|\boldsymbol{r}-\boldsymbol{r}'|} = \frac{q}{r} - \sum_{i=1}^{3} p_i \frac{\partial}{\partial x_i}\frac{1}{r} + \mathcal{O}(2) = \frac{q}{r} + \frac{\boldsymbol{p}\cdot\boldsymbol{r}}{r^3} + \mathcal{O}(2) \qquad (1)$$

, where the definition of the *dipole moment* $p_i = \int d\boldsymbol{r}'\, x_i' \rho(\boldsymbol{r})$ and the total charge q was used. The first term is just the Coulomb potential of a single charge q, whereas the second term is the *dipole potential* Φ_{dipole}. The potential energy of a dipole $\boldsymbol{p}_1$ in the electric field $\boldsymbol{E}_2$ of a dipole $\boldsymbol{p}_2$ is then given by

$$U_{dip-dip} = -\boldsymbol{p}_1 \cdot \boldsymbol{E}_2 = \boldsymbol{p}_1 \cdot \nabla\Phi_{dipole} = \frac{\boldsymbol{p}_1 \cdot \boldsymbol{p}_2}{r^3} - \frac{3(\boldsymbol{p}_1 \cdot \boldsymbol{r})(\boldsymbol{p}_2 \cdot \boldsymbol{r})}{r^5} \qquad (2)$$

For the induced dipole – dipole and Van der Waals interaction we need the concept of polarizability, which is also needed later in this thesis. Consider an otherwise neutral charge distribution $\rho(\boldsymbol{r})$ (e.g. an atom or a molecule) and an external electric Field $\boldsymbol{E}$. The electric field can induce a dipole into $\rho(\boldsymbol{r})$ by exerting a force onto it and thereby partially separating charges within $\rho(\boldsymbol{r})$. The induced dipole moment is $\boldsymbol{p} = \boldsymbol{\alpha}\boldsymbol{E}$ with the *polarizability tensor* $\boldsymbol{\alpha}$. The potential energy of the induced dipole – dipole system is then

$$U_{ind-dip} = -\boldsymbol{p}_{ind} \cdot \boldsymbol{E}_{dipole} = -\boldsymbol{\alpha}\boldsymbol{E}_{dipole} \cdot \boldsymbol{E}_{dipole} \propto -\frac{\alpha \boldsymbol{p}^2}{r^6} \tag{3}$$

where for the last proportionality a scalar polarizability was assumed (i.e. $\boldsymbol{\alpha}$ is diagonal with equal entries). It is mentioned that, due to the minus sign, the induced dipole – dipole interaction is attractive. While the interaction energy (potential energy) of the dipole – dipole interaction drops off with third power of distance, the induced dipole – dipole interaction is much shorter ranged due to the sixth power drop off with distance.

Lastly, but most important for OSCs, especially polymeric, one has the Van der Waals interaction between molecules. It is basically the induced dipole – induced dipole interaction. Quantum mechanically, the electrons of an atom are not always statically distributed according to their wavefunction, but can fluctuate such that temporary dipoles can occur that then again can induce dipoles in another molecule and vice versa. The attractive part of the Van der Waals interaction is like the one of induced dipole – dipole interaction and scales with $\Phi \propto 1/r^6$. However, increasing overlap of orbitals due to low distance is counteracted by Paulis exclusion principle, leading to a repulsive counter force. This can be empirically modeled by adding and exponential term or another power-law term to the attractive potential, such one arrives at the *Lennard-Jones Potential*

$$\Phi(r) = \frac{A}{r^{12}} - \frac{B}{r^6} = 4\epsilon\left(\left(\frac{\sigma}{r}\right)^{12} - \left(\frac{\sigma}{r}\right)^{6}\right) \tag{4}$$

that has a minimum which depth is determined by ϵ and a zero-crossing determined by σ. The location of the minimum can be interpreted as some kind of Van der Waals bonding length. For single molecules the Van der Waals interaction is negligible, but it gets stronger for high contact area like in polymers, where it gets the main intermolecular force.

Dielectric Constant and Polarizability

How strong microscopic electrostatic fields influence the interactions between charges or molecules within a material can be described by the *dielectric constant* $\epsilon_r \geq 1$. It describes the ability of the material to screen charges and reduces Coulomb potentials by

$V_{Coulomb} = \frac{q}{r} \rightarrow \frac{q}{\epsilon_r r}$. For ideal metals ϵ_r is technically infinite since there are no electric fields within a metal because charges would respond to the electric force and redistribute freely until

there is no force and therefore field anymore. In organic semiconductors the situation is quite opposite. Charges are localized and immobile, leading to a very low dielectric constant, usually in the range of 3 to 4. However, experiments have shown that doped OSCs can have indeed a higher dielectric constant[39,40]. One can make a toy model of molecular doped OSC to understand this behavior as shown by Comin et al.[41]. The following section will summarize their theoretical approach.

The authors assume a fcc lattice with random gaussian distributed displacements to model the disordered nature of OSCs. At the lattice sites i induced dipoles $\boldsymbol{\mu}_i = \boldsymbol{\alpha}_i \boldsymbol{E}_i$ are considered according to the total microscopic field at site i $\boldsymbol{E}_i = \boldsymbol{E}_i^0 + \boldsymbol{E}_i^{\mu}$. Here, $\boldsymbol{E}_i^0$ are the external fields and fields from charged sites and $\boldsymbol{E}_i^{\mu}$ is the field contribution of other induced dipoles and $\boldsymbol{\alpha}_i$ are the polarizability tensors of the individual sites i. Now the induced dipole relations given for each individual site i are stacked and summarized into one supervector

$$\begin{pmatrix} \boldsymbol{\mu}_1 \\ \vdots \\ \boldsymbol{\mu}_N \end{pmatrix} = \begin{pmatrix} \boldsymbol{\alpha}_1 & & 0 \\ & \ddots & \\ 0 & & \boldsymbol{\alpha}_N \end{pmatrix} \begin{pmatrix} \boldsymbol{E}_1 \\ \vdots \\ \boldsymbol{E}_N \end{pmatrix} \quad \Leftrightarrow \quad \boldsymbol{\mu} = \widehat{\boldsymbol{\alpha}} \boldsymbol{E} \tag{5}$$

Now the distance vector $\overrightarrow{r_{ij}}$ of each pair *ij* of dipoles is calculated and for each pair the dipole-field tensor is calculated

$$\boldsymbol{D}_{ij} = \frac{3\overrightarrow{r_{ij}} \otimes \overrightarrow{r_{ij}} - r_{ij}^2 \mathbb{I}}{4\pi\epsilon_0 r_{ij}^5} \tag{6}$$

Here $\otimes$ is the dyadic product such that $\boldsymbol{E}_i^{\mu} = \boldsymbol{D}_{ij}\boldsymbol{\mu}_i$ is the induced dipole field of i at dipole j. Bringing everything together into one large vector notation, with $\boldsymbol{D}$ being a block matrix consisting of $\boldsymbol{D}_{ij}$, one can write $\boldsymbol{E}^{\mu} = \boldsymbol{D}\boldsymbol{\mu}$. Now one can solve the following expression for $\boldsymbol{\mu}$

$$\widehat{\boldsymbol{\alpha}}^{-1}\boldsymbol{\mu} = \boldsymbol{E} = \boldsymbol{E}^0 + \boldsymbol{E}^{\mu} = \boldsymbol{E}^0 + \boldsymbol{D}\boldsymbol{\mu} \Leftrightarrow (\widehat{\boldsymbol{\alpha}}^{-1} - \boldsymbol{D})\boldsymbol{\mu} = \boldsymbol{E}^0 \tag{7}$$

Knowing the induced dipoles from solving above's equation, one can now calculate the induced polarization $\boldsymbol{P} = \frac{1}{V}\sum_i \boldsymbol{\mu}_i = \epsilon_0 \boldsymbol{\chi} \boldsymbol{E} = \epsilon_0 \boldsymbol{\zeta} \boldsymbol{E}^{ext}$ with the susceptibility $\boldsymbol{\chi}$ and susceptibility to an external field, $\boldsymbol{\zeta}$, and solve for latter. For a uniformly polarized medium it holds for the total macroscopic field $\boldsymbol{E} = \boldsymbol{E}^{ext} - \frac{\Delta \cdot \boldsymbol{P}}{\epsilon_0}$, where $\Delta = \frac{\mathbb{I}}{3}$ is the depolarization tensor for spherical samples. Finally, one can calculate the susceptibility $\boldsymbol{\chi}$ and the dielectric tensor $\boldsymbol{\epsilon}_r$ via

$$\boldsymbol{\chi} = (\mathbb{I} - \Delta \cdot \boldsymbol{\zeta})^{-1}\boldsymbol{\zeta} \quad \text{and} \quad \boldsymbol{\epsilon}_r = \mathbb{I} + \boldsymbol{\chi} \tag{8}$$

For simplicity, one can assume a constant polarizability α_{host} for the OSC molecules and another also constant polarizability α_{CT} for the dopants and depending on the charge concentration c define an average c-dependent polarizability $\alpha_{avg} = (1-c)\alpha_{host} + c\alpha_{CT}$ and do the calculation. The continuous line in **Figure 1** corresponds to this case, whereas the histograms are results from inhomogeneous lattice simulations.

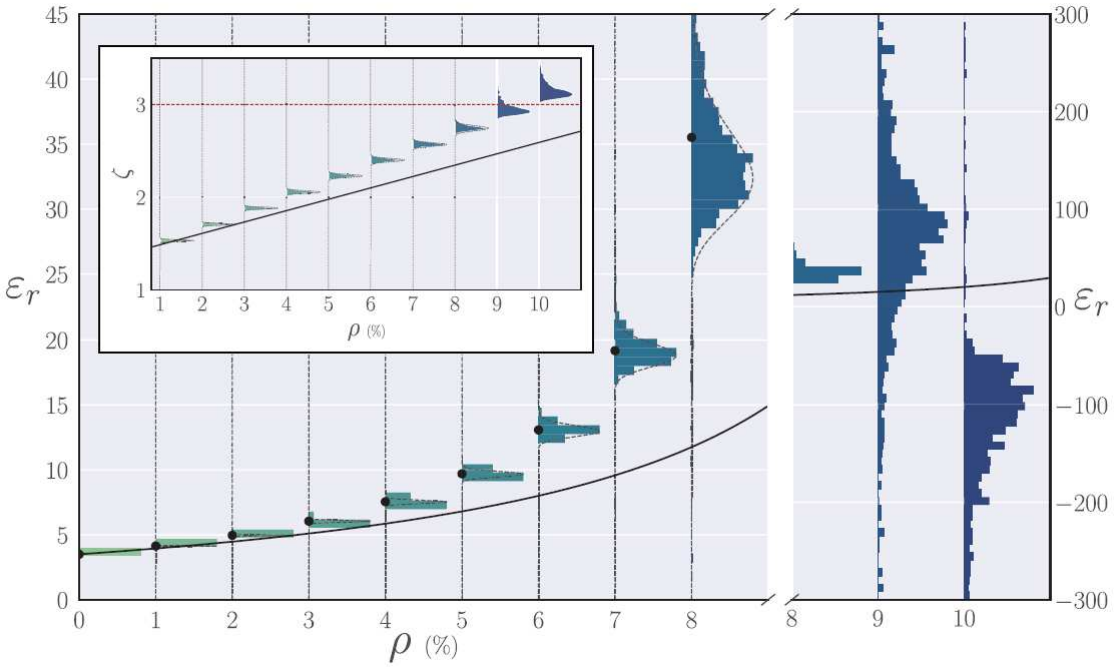

Figure 1 – Full line: Effective homogeneous medium. Dashed lines: Gaussian fits to inhomogeneous lattice simulations. Reproduced with permission from [41], © 2021 Wiley-VCH GmbH.

The plot shows clearly an increase of the dielectric constant with increasing doping. Therefore, the enhanced dielectric constant in doped OSCs can be attributed to high polarizability of dopant molecules that allow for enhanced screening. However, this model is clearly limited, since in contrast to their effective medium approach, for intermediate to higher charge concentrations, their inhomogeneous lattice simulations give rise to a dielectric catastrophe, which is not observed in OSCs. It is likely that the model enters for higher charge concentrations a regime that rather describes the dielectric catastrophe of ferroelectric materials near the Curie temperature as can be modeled with e.g. Ising models.

Morphology

Classification

As discussed in the last chapter, the main inter-molecular interaction of OSCs is the weak Van der Waals force and the main intra-molecular interaction is the covalent bond. Covalent bonds are weak enough that the thermal energy or microscopic mechanical forces can already cause torsion or bending of molecular bonds. Additionally, Van der Waals forces are so weak that they cannot constraint the degrees of freedom between molecules as can the Coulomb force in ionic crystals. Together with the possibly complex and large molecular structure this leads to the possibility of an abundance of chemical and geometrical defects implying an intrinsically disordered microscopic structure of the bulk material. The microscopic and mesoscopic structure of the bulk material is called *morphology*. Physical and chemical properties of OSCs are essentially influenced by the morphology[42–44]. **Figure 2** shows a rough classification of morphologies in organic materials into four categories.

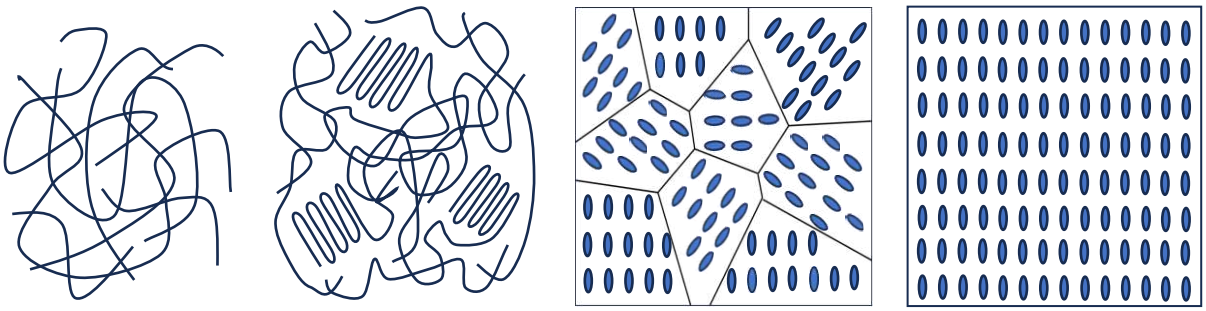

Figure 2 – Morphology categories

Completely disordered morphologies are called *amorphous*. In *semicrystalline* media, crystalline regions are embedded in an amorphous background. Materials consisting of differently oriented crystalline grains are called *polycrystalline*. If the material is a macroscopically ordered (single-) crystal, it is called *crystalline*. Polycrystalline and crystalline morphologies can usually only be obtained with small molecules, while polymeric organic materials usually form amorphous or semicrystalline morphologies[42]. However, there are more kinds of specific morphologies than those mentioned above. Depending on the choice and

combination of organic materials, solutions, substrates, deposition- and post-processing techniques, one can achieve specific microscopic structures. For example, the effective dimensionality of the organic material can be modified, like rubbing of PBTTT leads to quasi-one-dimensional morphology of many parallel chains[45].

Edge-on and Face-on Orientation

Another type of molecular orientation classification is the classification into edge-on and face-on orientation or morphology. Technically, edge-on or face-on morphologies are semi-crystalline morphologies, with the specification of how the aggregates are oriented with respect to the substrate as illustrated in **Figure 3**.

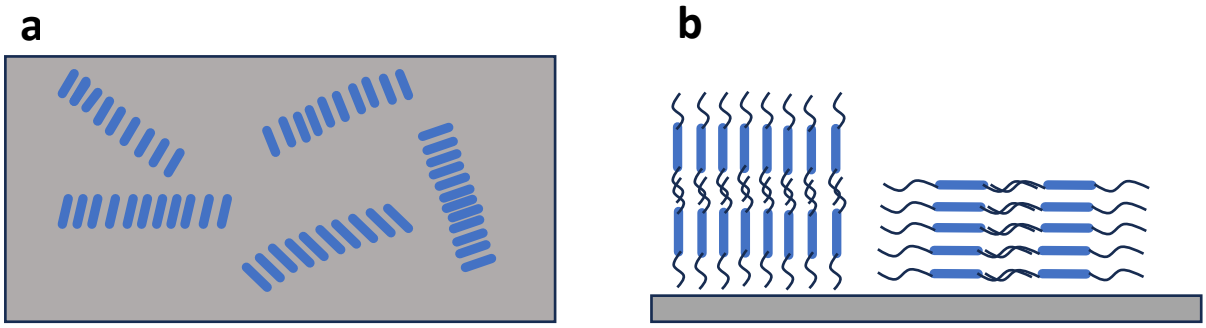

Figure 3 – **a** Top view of edge-on orientated lamellar stacks. **b** Side view of edge-on orientated (left) and face-on orientated stacks (right).

As this thesis contains modeling and simulation of the implications of edge-on and face-on orientation on the thermoelectric power factor of OSC as part of a collaboration, it is useful to have a deeper look into the theoretical background here.

Villalva et al.[46] utilized Hansen Solubility Parameters (HSPs) to control the crystallinity and orientation of different OSC films. HSPs were introduced by Hansen[47,48] in 1967 and are an attempt to quantify solubility of molecular species dependent on different molecular interactions. For a solvent – solute pair, the energy of dispersive (δD), polar (δP) and hydrogen bonding (δH) forces are determined, typically in units of $MPa^{1/2}$. One can now treat these three quantities as axes in a three-dimensional cartesian coordinate system and solvents can be depicted as points in this so-called Hansen space. In this set-up, it is usually found that good solvents for a molecule are approximately located within a sphere of some radius R_0 called the interaction radius. The value of R_0 is determined empirically by testing different solvents at a

given temperature and concentration. For a given solvent, one can now calculate the Hansen radius R_a via

$$R_a^2 = 4(\delta D_1 - \delta D_2)^2 + (\delta P_1 - \delta P_2)^2 + (\delta H_1 - \delta H_2)^2 \quad (9)$$

For $R_a < R_0$ the solvent is typically good, whereas for $R_a \geq R_0$ the solubility typically gets worse. The principle behind that is that molecular species with similar molecular interactions dissolve good. If $R_a < R_0$ (good solution), polymer chains are almost fully dissociated, which preferably produces face-on orientation. However, if R_a is in the vicinity of R_0, pre-aggregates are formed in solution that preferably produce edge-on orientation on the OSC film.

However, as Villalva et al. point out, R_a alone is not a sufficient as a figure of merit to determine the orientation of the film (edge-on face-on ratio (EFR)). They propose a refined parameter including the boiling point of the solvent (BP) by multiplication $R_a \cdot BP$. For this quantity, they find an exponential dependence of the EFR from $R_a \cdot BP$.

Besides solvents, dopants can influence and improve molecular packing. They find that dopant – polymer interaction can reduce the solubility of the polymer-dopant complex and facilitate conjugated polymer nucleation and therefore increase crystalline fraction and edge-on portion of the film.

Molecular Dynamics

In order to predict and calculate morphologies, unfortunately ab initio calculations like DFT are computationally too expensive since thousands of atoms need to be included for a significant and physically meaningful box size. However, due to emergence, it is mostly not needed to do so. The dynamics of molecules on larger scales does mostly not require quantum mechanically exact calculations. Instead, one can perform Newtonian dynamics with optimized parametrized potentials, so-called force fields. Given molecular structures in equilibrium, one can model different potential terms for different forces between molecules. The force field of a specific molecular setup is not unique and needs to be carefully chosen and optimized. In a corporation contributing to this thesis, P.S. Floris (see also [49]) performed Molecular Dynamics (MD) for different P3HT oligomers. For this, the following standard OPLS-AA[50] force field with standard parameters was used

$$U = \sum_{bonds} k_b(\boldsymbol{r} - \boldsymbol{r}_0)^2 + \sum_{angles} k_\theta(\theta - \theta_0)^2 + \sum_{dihedrals} \sum_{n=1}^{4} \frac{V_n}{2}(1 + \cos(n\Phi - \Phi_n)) + \sum_{i<j} \left[\frac{q_i q_j}{4\pi\epsilon_0 r_{ij}} + 4\epsilon_{ij} \left(\left(\frac{\sigma_{ij}}{r_{ij}} \right)^{12} - \left(\frac{\sigma_{ij}}{r_{ij}} \right)^{6} \right) \right] \quad (10)$$

The first term is the potential for displacing two bonded atoms from its equilibrium position $\boldsymbol{r}_0$ in the harmonic approximation with force constant k_b. The second term is the potential term for bending two bonds from equilibrium angle θ_0, again in the harmonic approximation with force constant k_θ. The third term is the potential due to torsion of the dihedral angle ϕ associated to a rotation around the central bond of a four-atom sequence (i-j-k-l). It is expressed by the Fourier coefficients V_n (with the dihedral periodicity n) interpreted as force constants and with the phase-shifts Φ_n with typical values of 0 or π. The last term contains the Coulomb energy between two partial charges q_i and q_j located at atom i and j and the Lennard-Jones potential of the Van der Waals force. The Lennard-Jones parameters for two different atoms i and j are calculated using the Lorentz-Berthelot combining rule via $\epsilon_{ij} = \sqrt{\epsilon_{ii}\epsilon_{jj}}$ and $\sigma_{ij} = \sqrt{\sigma_{ii}\sigma_{jj}}$. For the Van der Waals force, a Lennard-Jones (LJ) cutoff distance of 1 nm was chosen and for the long range electrostatic a particle-particle particle-mesh (PPPM) solver was applied with a spacing of 10^{-4} in Fourier space for the FFT-calculation. The force constants and partial charges are parametrized from DFT calculations of different molecular geometries, vibrational energies and torsional profiles.

Having a suitable force field, one can solve the Newtonian dynamics equations

$$\dot{\boldsymbol{p}}_i = -\nabla_i U \quad (11)$$

and assigns random initial conditions for the positions of the molecules and their momenta in a box of volume V with periodic boundary conditions. The system is then evolved until equilibrium is reached. The described procedure gives only morphologies, but for the purpose of this thesis we are also interested in the thermal conductivity of the system. This is done by a form of non-equilibrium MD, with fully atomistic approach-to-equilibrium MD (AEMD), based on the lumped capacitance approximation, where thermal fluctuations within a given (sub-) volume are treated negligible. The procedure is as follows. The simulation box is divided into two parts of equal volume. Now the first half is heated up to $T_1 = 400\ K$ and the second

part to $T_2 = 200\ K$ via velocity rescaling in 10^5 steps with time step $t_s = 0.5\ fs$. This is done by taking the current configuration of each volume and calculating its kinetic energy $K = \frac{1}{2}\sum_i m_i \boldsymbol{v}_i^2$ and scaling the velocities in each step with $\alpha = \sqrt{T_{target}/T_{current}}$ such that $K = 3Nk_BT_{target}/2$. Then the system evolves within its force field for time t_s and the procedure is repeated with the 10^5 steps until a step like temperature profile is reached. Then the system is evolved in the NVE ensemble (particle number N, volume V and energy E are constant) until thermal equilibrium is reached. The thermal conductivity can then be calculated by comparing the time evolution of the average temperature difference of the two volumes to the heat equation solution[51]:

$$\Delta T(t) = \langle T_1 \rangle - \langle T_2 \rangle = \sum_{n=1}^{\infty} C_n \exp(-\alpha_n^2 \bar{\kappa}_i t) \tag{12}$$

with the thermal diffusivity $\bar{\kappa}_i$, $\alpha_n = \frac{2\pi n}{L_i}, C_n = 8(T_1 - T_2)\frac{\left[\cos\left(\frac{\alpha_n L_i}{2}\right)-1\right]^2}{\alpha_n^2 L_i^2}$ where L_i is the box length in direction i. From there, the lattice thermal conductivity can be calculated with $\kappa_i = \bar{\kappa}_i c_v/V$ where the heat capacity $c_v = 3Nk_B$ from Dulong-Petit law and N is the number of atoms.

However, the above NVE ensemble corresponds to a microcanonical ensemble. Experimental setups however are rather canonical ensembles coupled to a thermal bath in a specific atmospheric pressure, so N, P and temperature T are constant. In order to achieve the so-called NPT ensemble, one needs to modify the Hamiltonian of the system. This is done with the Nose Hoover thermostat and barostat[52]. The dynamics equations are thereby modified by friction terms

$$\dot{\boldsymbol{q}}_i = \frac{\boldsymbol{p}_i}{m_i},\ \dot{\boldsymbol{p}}_i = \boldsymbol{F}_i(\boldsymbol{q}) - (\dot{\epsilon} + \xi)\boldsymbol{p}_i\ ,\dot{\xi}Q = \sum_i \frac{\boldsymbol{p}_i^2}{m_i} - gk_BT\ ,\dot{\epsilon} = \frac{\dot{V}}{3V},\quad \ddot{\epsilon} = \frac{(P - P_{ext})V}{\tau^2 k_B T} \tag{13}$$

that emerge when modifying the Hamiltonian as follows

$$H = \sum_i \frac{\boldsymbol{p}_i^2}{2m_i} + U\left(\frac{\boldsymbol{r}}{V^{\frac{1}{3}}}\right) + \frac{Q}{2}\xi^2 + \frac{3}{2}\dot{\epsilon}^2\tau^2 k_B T + P_{ext}V \tag{14}$$

Here, $g = 3N$ is the degrees of freedom, P_{ext} is the external pressure, and Q is some kind of mass of the thermal bath. The term $Q\xi^2/2$ is the kinetic term of the thermal bath, where Q controls how fast heat with the thermal bath is exchanged. This term acts as thermostat to maintain constant temperature. The fourth term is the kinetic term of the barostat. The relaxation time τ determines how fast pressure differences are adjusted. The last term describes the mechanical work done by the pressure. The idea behind the barostat is that the volume of the system is varied to adapt for the pressure, therefore the particle positions are scaled with $1/V^{1/3}$ to mimic the change in volume. The parameter $\dot{\epsilon}$ thereby is a measure of the speed or rate of volume change. With this procedure, the system is brought to be in the isothermal and isobaric ensemble. Note that without the barostat, the system is in a canonical ensemble with NVT fixed.

With this NPT ensemble, the system is finally equilibrated at $T = 300\ K$ and 1 atm with time step 0.5 fs to achieve the final morphology that we want to obtain. The results for the simulated P3HT will be shown in the Results section of this thesis.

Simplified Annealing Model

To study the effect of aggregation in OSCs, I did not specifically rely on the previously described MD simulations. To simplify the aggregated morphology generation, now the specific molecular morphologies and molecules are abstracted. For this, a simple regular lattice of size $N = N_x \times N_y \times N_z$ with two site species, the host and the guest. Single molecules are treated as sites of the lattice. To aggregate the guest sites, an annealing procedure is performed as in Ref [53]. First, for a random distribution of host and guest sites, the free energy of the system is calculated via the sum over all sites and their 6 direct neighbors

$$E = \frac{1}{2}\sum_{i=1}^{N}\sum_{j=1}^{6} E_{M(i),M(j)} \tag{15}$$

where M(i) is the material of site i and $E_{A,B}$ are the free energies associated with a molecular contact between material A and B. For contact of same sites, $E_{A,A}$ can be calculated from the e.g. experimentally extracted (evaporation enthalpy by thermogravimetry) cohesive energy per mole $E_{coh} = 3N_A E_{A,A}$ with the Avogadro constant N_A. For the model it is assumed that the cohesive energies are very similar in OSCs such that it is set $E_A = E_B$. Additionally, it is assumed that $2E_{A,B} = E_{A,A} = E_{B,B}$. For a given annealing temperature, the procedure is now to

repeatedly swap neighboring sites to minimize the free energy, thus minimizing the contact area between host and guest sites. The probability, at which the swapping tries to overcome free energy barriers $\Delta E_A = E_{old} - E_{new}$ is modeled as Boltzmann type rate $R(T) \propto \exp\left(-\frac{\Delta E_A}{k_B T}\right)$. The decision which swap to make in each step is then done in a Monte Carlo manner (see later chapter) based on R(T), meaning that swaps with higher reduction of free energy have higher probability than lower. Higher annealing temperatures provides higher thermal energies to overcome high barriers, making aggregation slower and worse. The annealing procedure is continued until a maximum number of swaps is reached or a required aggregate size is reached. The aggregate radius r_C is approximated via the volume V occupied by the guest sites and their interface area A through the assumption that the aggregates are spherical

$$\frac{V_{sphere}}{A_{sphere}} = \frac{\frac{4}{3}\pi r_c^3}{4\pi r_c^2} \quad \Leftrightarrow \quad r_c = \frac{3V}{A} \tag{16}$$

This method can give large aggregates, but lacks more detailed structural information like site connectivity and relative orientation.

3-Phase-Model

An attempt to improve this is a group intern implementation of a lattice-based morphology generation simulating polymer growth in a 3-phase-model.

The 3-Phase-Model divides the gradual drying polymers into dissolved, drying and solid phases. The weak interaction of the dissolved phase allows to neglect the dissolved phase and only the interactions of the solid and drying phases need to be considered. The morphology generating process starts by initialization of a simple lattice. The growing part starts by random nucleation of several monomers. The monomers now simultaneously grow until a maximum length is reached or they run into dead ends. For growing, new monomers are attached to the polymer ends in a direction and orientation depending on the nearest neighbor interactions.

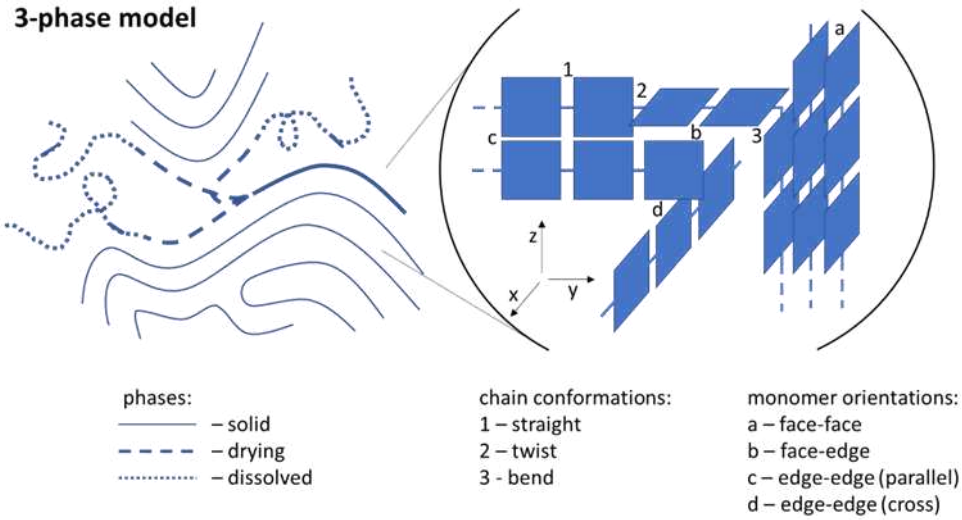

Figure 4 - Visualization of the 3-phase model and the possible chain conformations and monomer-monomer orientations. (Image by Martijn Kemerink)

For that, three intra-chain interaction energies and four inter-chain interaction energies are set. The intra-chain interactions consist of the energy cost for attaching the monomer straight, twisted, or bended up or down. Inter-chain interactions consist of the energy costs of four possible relative orientations of the monomer with its neighbor in a simple lattice, that is face-face, face-edge, parallel edge-edge or cross edge-edge (see **Figure 4**). Additionally, other possible interactions are generalized into alignment fields, which reward or penalize monomer orientations and directions in x, y and z-directions respectively. For each of the four possible orientations of the drying monomer, the inter-chain interaction energies with all nearest neighbors and the intra-chain energy and the direction and orientation rewards or penalties are added into the total interaction energy $E_i^{o,d}$ of monomer i. The orientation and direction of the drying monomer is then randomly chosen from all possible configurations relative to their relative probability that is modeled as being proportional to the Boltzmann factor

$$p_i^{o,d} \propto \exp\left(-\frac{E_i^{o,d}}{k_B T}\right) \tag{17}$$

For a more realistic growth model, not only one monomer in the drying phase, but a 4-multiple of monomers is considered, where four is empirical, which avoids running into dead ends. However, not only the n nucleation sites from the initialization grow, but new nucleation sites can be generated with either random probability or with probability proportional to the maximum length of the chain. For a new nucleation site an empty site is randomly chosen and

then diffused until at least one nearest neighbor is occupied, which should mimic the tendency of nucleation near previously solidified material. Alternatively, nucleation can take place at empty sites that have the most free volume around them to mimic polymers avoiding each other due to steric or electrostatic effects.

The maximum chain length can either be set constant for all chains or randomly for all chains according to the Flory-Schulz[54] distribution to model polydispersity. According to Flory-Schulz, the number average length distribution is given by

$$N(x) = (1-p)p^{x-1} \tag{18}$$

where x is the number of monomer units in a chain and p the growing probability set to constant. Then the distribution can be understood as growing x-1 times and then not growing anymore (factor 1-p). The associated weight-average molecular weight distribution is then

$$W(x) = \frac{xN(x)}{\sum_k kN(k)} = x(1-p)^2 p^{x-1} \tag{19}$$

The number average molecular weight M_n, the weight average molecular weight M_w with the monomer molecular weight m and the polydispersity PDI are defined as

$$M_n = \frac{m}{1-p} \qquad M_w = \frac{m(1+p)}{1-p} \qquad PDI = \frac{M_w}{M_n} = 1+p \tag{20}$$

After the morphology generation is done, one can analyze the morphology with different measures.

The typical feature size can be calculated similarly to the annealing model. Moreover, the typical size of a single polymer can be calculated as

$$r_{typ} = \frac{\sum_i |\boldsymbol{r}_i - \boldsymbol{r}_{COM}|}{x} \tag{21}$$

with the center of mass position of the polymer $\boldsymbol{r}_{COM}$ and the monomer position of monomer i in the chain $\boldsymbol{r}_i$. Depending on the parameter settings, the polymers can grow quasi one-, two- or three-dimensional. The effective dimensionality can be obtained from a double-log plot of x vs. r_{typ} since $x \propto r_{typ}^d$ for dimension d.

Having obtained a morphology by either of the methods described above, one can now move on to define a Hamiltonian for the OSC with its respective morphology. For that, the Tight-Binding approximation of the OSC system is used and introduced over the next chapter.

Tight Binding Theory

Introduction and HOMO/LUMO Bandwidth

The theoretical section up to Wannier functions is based and adapted from my Master thesis[55]. For metals, the conduction electrons are weakly bound to the atomic nuclei so that they can delocalize over a long-range up to the whole material. Opposing that, the situation in organic molecular materials or ionic crystals is different. There, the electrons usually stay close to the nuclei. In this section, it will be first shown how in this setting of tightly bound electrons the overlap between neighboring molecules gives rise to a transition from individual and localized states to a band formation. After that, the mathematical framework for the Tight Binding formalism will be introduced.

To determine the influence of overlap between molecules on the energetics (following Hunklinger[38]), a periodic lattice with its periodic potential will be used for simplicity. Isolated molecules, as stated in the introduction, form discrete energy levels (HOMO-i and LUMO+i). For those, the stationary Schrödinger equation reads

$$H_A\psi_i = E_i\psi_i \tag{22}$$

With the single-molecule Hamilton operator H_A and its eigen energies (being HOMO-i and LUMO+i) E_i and the respective eigenfunctions ψ_i. The single-electron approximation will be imposed, which means that the motion of a single electron in the field of all other atoms H_S will be studied. Therefore, the perturbing potential is

$$H_S(\boldsymbol{r} - \boldsymbol{R}_m) = \sum_{n \neq m} V_A(\boldsymbol{r} - \boldsymbol{R}_n) \tag{23}$$

with $\boldsymbol{r}$ being the electron position, $\boldsymbol{R}_m$ the position of the lattice molecule the electron resides on in the beginning and $\boldsymbol{R}_n$ the position of the molecule n in the rest of the lattice (being the perturbation). V_A is the potential of a free molecule. The single electron Hamiltonian reads

$$H = H_A + H_S = -\frac{\hbar^2}{2m}\Delta + V_A(\boldsymbol{r} - \boldsymbol{R}_m) + H_S(\boldsymbol{r} - \boldsymbol{R}_m) \tag{24}$$

The eigen-energy $E_{k,i}$ for the solution wavefunction $\Psi_{k,i}$ is calculated as usual:

$$E_{k,i} = \frac{\int \Psi_{k,i}^* H \Psi_{k,i} \mathrm{d}V}{\int \Psi_{k,i}^* \Psi_{k,i} \mathrm{d}V} \tag{25}$$

, but since the exact solution is not known, the wave function $\Psi_{k,i}$ will be approximated by a superposition of the single-molecule eigen functions such that the wave function respects the symmetry of the lattice and fulfills the properties of a Bloch function. This gives the wave function ansatz

$$\Psi_{k,i} \approx \phi_{k,i} = \frac{1}{\sqrt{N}} \sum_m \psi_i(\boldsymbol{r} - \boldsymbol{R}_m) \exp(i\boldsymbol{k}\boldsymbol{R}_m) \tag{26}$$

with N being the total number of molecules in the lattice. This gets now inserted into Equ. (25). Since the overlap between different molecules is assumed to be small compared to other terms, they can be neglected, so the normalization factor will be about unity and the numerator splits into three parts:

$$E_{k,i} \approx E_i - \alpha_i - \sum_n \exp(i\boldsymbol{k}\boldsymbol{R}_n)\, \beta_{i,n} \tag{27}$$

where the identity $\sum_m \exp(i\boldsymbol{k}\boldsymbol{R}_m) = \sqrt{N}\, \delta_{k0}$ was used and the factor N for the sum containing $\beta_{i,n}$ was canceled by recognizing that the double sum is N times the sum of Equation (27). The first part is the eigenenergy part of the individual molecules E_i, the second is the energy shift due to the perturbing potential

$$\alpha_i = -\int \psi_i^*(\boldsymbol{r} - \boldsymbol{R}_m) H_S(\boldsymbol{r} - \boldsymbol{R}_m) \psi_i(\boldsymbol{r} - \boldsymbol{R}_m) \mathrm{d}V \tag{28}$$

And the third is the transfer integral resulting from interaction with the perturbing field and the molecular overlap

$$\beta_{i,n} == -\int \psi_i^*(\boldsymbol{r} - \boldsymbol{R}_n) H_S(\boldsymbol{r} - \boldsymbol{R}_m) \psi_i(\boldsymbol{r} - \boldsymbol{R}_m) \mathrm{d}V \tag{29}$$

where we set $\boldsymbol{R}_m = 0$ without loss of generality (wlog). Only caring about nearest neighbors in for example a cubic lattice, $E_{k,i}$ is for a lattice constant a evaluated as

$$E_{k,i} \approx E_i - \alpha_i - 2\beta_i\big[\cos(k_x a) + \cos\big(k_y a\big) + \cos(k_z a)\big] \tag{30}$$

The interaction caused by the perturbing field of the overlapping molecules results in a formation of a narrow band (in this case of width $12\beta_i$) out of the earlier discrete molecular

energy levels, i.e. HOMO and LUMO. The bandwidth gets larger with decreasing molecular separation, and also at some point interactions between HOMO-i and HOMO-j further increase the bandwidth, but for realistic separations and transfer integrals, this is usually not the case. Additionally, bandlike transport is only obtained, if the disorder σ_{DOS} (see next sections) is less than the bandwidth, which is for organics usually not the case[36]. Nevertheless, for semi-crystalline morphologies, that is crystallized regions between amorphous and disordered regions, locally a band can form, and if the transfer integral between crystallized regions is large enough, band like behavior could maybe even be observed macroscopically. But usually hopping between localized states as in the Mott theory is the limiting and therefore dominating charge transport process although more delocalized states can substantially improve the conductivity as will be studied in this thesis.

Second Quantization

(Following Altland and Simons[56]). The first fundament of the tight binding theory is the formalism of second quantization, which is a way of rewriting the Hamiltonian into a different form, using abstract, but physically intuitive operators named *creation and annihilation operators.* In the occupation number representation of a quantum mechanical state $|n_1, n_2, \dots\rangle$, also called a *Fock state*, which shows the number of particles in each state i, the *creation operator* acts as

$$a_i^\dagger |n_1, \dots, n_i, \dots\rangle \coloneqq (n_i + 1)^{\frac{1}{2}} \zeta^{s_i} |n_1, \dots, n_i + 1, \dots\rangle \tag{31}$$

With $s_i = \sum_{j=1}^{i-1} n_j$, $\zeta = 1$ for bosons and $\zeta = -1$ for fermions. For fermions, the occupation numbers have to be taken mod 2. This means, the operator $a_i^\dagger$ raises the occupation number of state i. It is therefore called *creation operator.* It follows that the Fock basis states can be obtained by repeated application of creation operators on the vacuum state $|0\rangle$

$$|n_1, n_2, \dots\rangle = \prod_i \frac{1}{\sqrt{n_i!}} \left(a_i^\dagger\right)^{n_i} |0\rangle \tag{32}$$

Due to the unitarity of Hamiltonians, one also has to determine the action of the Hermitian adjoint operator of the creation operator, $\left(a_i^\dagger\right)^\dagger = a_i$. One finds the action of a_i on a Fock state to be

$$a_i |n_1, \dots, n_i, \dots\rangle = n_i^{\frac{1}{2}} \zeta^{s_i} |n_1, \dots, n_i - 1, \dots\rangle \tag{33}$$

This means that the operator a_i reduces the number of particles in state i, and is therefore called *annihilation operator.* If the state i is a vacuum state, the annihilation operator just destroys the state itself, i.e. $a|0\rangle = 0$.

Representation of operators

One important operator is the occupation number operator, which is defined as:

$$\hat{n}_\lambda = a_\lambda^\dagger a_\lambda \tag{34}$$

The application of this operator on a Fock state gives

$$\hat{n}_{\lambda_j}\left|n_{\lambda_1}, n_{\lambda_2}, \dots\right\rangle = n_{\lambda_j}\left|n_{\lambda_1}, n_{\lambda_2}, \dots\right\rangle \tag{35}$$

with n_{λ_j} being the occupation number of the state λ_j, justifying the name of the operator. Since any state in Fock space can be generated by the application of creation and annihilation operators, any operator must have a representation in terms of creation and annihilation operators. In a diagonal basis, the representation of a single particle operator $\hat{\mathcal{O}}_1$ in the creation/annihilation operator formalism is

$$\hat{\mathcal{O}}_1 = \sum_i o_{\lambda_i} \hat{n}_{\lambda_i} \tag{36}$$

Which is just the sum of the occupations of every state weighted by its eigenvalue. In a general basis, one finds

$$\hat{\mathcal{O}}_1 = \sum_{\mu\nu} \langle \mu | \hat{\mathcal{O}}_1 | \nu \rangle a_\mu^\dagger a_\nu \tag{37}$$

which intuitively removes a particle in state ν and creates one in state μ with its respective transition amplitude. This implies a matrix representation of the operator in the $\{\mu\}$ basis with matrix elements $H_{\mu\nu} = \langle \mu | \hat{\mathcal{O}}_1 | \nu \rangle$. This result can be generalized to many-body operators. A two-particle operator describes the interaction between two particles and can be represented as

$$\hat{\mathcal{O}}_2 = \sum_{\lambda\lambda'\mu\mu'} \langle \mu, \mu' | \hat{\mathcal{O}}_2 | \lambda, \lambda' \rangle a_\mu^\dagger a_{\mu'}^\dagger, a_\lambda a_{\lambda'} \tag{38}$$

An example of a two body-operator would be the electron-electron interaction due to Coulomb interaction.

Tight-Binding Approximation on Periodic Lattices

(Following[57]) We will start the discussion of the Tight-binding model on a periodic lattice and generalize afterwards. At the beginning of this chapter, where tightly bound electrons in a periodic lattice were studied to see the emergence of bands, already a simplification was used, which will now be studied in more detail. As in Equation (26), the starting point is Bloch's theorem. If the exact Bloch wavefunction, which is the exact solution to the problem, is not known, the periodic function in it can be constructed by superposition of some convenient or appropriate localized functions $\omega_\tau(\boldsymbol{r})$, where τ is some quantum number:

$$\phi_{k,\tau} = \frac{1}{\sqrt{V}} \sum_{\boldsymbol{R}} \omega_\tau(\boldsymbol{r} - \boldsymbol{R}) \exp(i\boldsymbol{k}\boldsymbol{R}) \tag{39}$$

which is a generalization of Equation (26) and therefore fulfills the Bloch wave conditions. As already said and used before, ω_τ can be some atomic orbital function or a molecular orbit function.

Now the Hamiltonian matrix elements are calculated in this Bloch wave basis. Bloch waves imply that only electron interactions with the same crystal momentum (momenta that only differ by some reciprocal lattice vector) are possible such that only the Hamiltonian matrix elements between different states τ will be considered.

$$\begin{aligned} H_{\tau'\tau}(\boldsymbol{k}) &= \langle \phi_{k,\tau'} | H | \phi_{k,\tau} \rangle \\ &= \sum_{\boldsymbol{R},\boldsymbol{R}'} \frac{1}{V} \exp\big(i\boldsymbol{k}(\boldsymbol{R} - \boldsymbol{R}')\big) \langle \omega_{\tau'}(\boldsymbol{r} - \boldsymbol{R}') | H | \omega_\tau(\boldsymbol{r} - \boldsymbol{R}') \rangle \\ &= \sum_{\Delta\boldsymbol{R}} \exp(-i\boldsymbol{k}\Delta\boldsymbol{R}) \langle \omega_{\tau'}(\boldsymbol{r} - \Delta\boldsymbol{R}) | H | \omega_\tau(\boldsymbol{r}) \rangle \end{aligned} \tag{40}$$

where in the last step **r** was shifted such that $\Delta\boldsymbol{R} = \boldsymbol{R}' - \boldsymbol{R}$ and then sum over **R** was performed giving $\sum_{\boldsymbol{R}} \frac{1}{V} = 1$. Defining the hopping amplitude

$$t_{\tau,\tau'}^{\Delta R} = \langle \omega_{\tau'}(\boldsymbol{r} - \Delta\boldsymbol{R}) | H | \omega_{\tau(\boldsymbol{r})} \rangle \tag{41}$$

The second quantized form of the Hamiltonian reads

$$H = \sum_{\Delta \mathbf{R}} \sum_{\substack{k \\ \tau,\tau'}} t_{\tau,\tau'}^{\Delta R} \exp(-i\boldsymbol{k}\Delta\boldsymbol{R}) a_{\boldsymbol{k},\tau'}^{\dagger} a_{\boldsymbol{k},\tau} = \sum_{\substack{\boldsymbol{k} \\ \tau,\tau'}} \epsilon_{\boldsymbol{k},\tau\tau'} a_{\boldsymbol{k},\tau'}^{\dagger} a_{\boldsymbol{k},\tau} \tag{42}$$

with $\epsilon_{\boldsymbol{k},\tau\tau'} = \sum_{\Delta \boldsymbol{R}} t_{\tau,\tau'}^{\Delta R} \exp(-i\boldsymbol{k}\Delta\boldsymbol{R})$. A Fourier transformation to real space of this expression yields

$$H = \sum_{\substack{\boldsymbol{R},\Delta\boldsymbol{R} \\ \tau,\tau'}} t_{\tau,\tau'}^{\Delta R} a_{\boldsymbol{R}+\Delta\boldsymbol{R},\tau'}^{\dagger} a_{\boldsymbol{R},\tau} \tag{43}$$

Mostly not all τ are considered. Usually, only the outermost orbitals of molecules participate in charge transport such that all other orbitals can be neglected and the Hamiltonian is simplified.

Wannier functions

(Following[57]) The problem about taking just some localized function ω_τ as atomic orbitals is that those states are not orthogonal and can be an overcomplete basis set, which can sometimes lead to problems in calculations. Now, instead of imposing some localized functions to obtain a Bloch wave, for a given Bloch state $\phi_{k,\tau}$ the localized functions ω_τ are searched. The first thing to notice about this is that the localized functions are not unique. In fact, any unitary transformation for a given set of localized functions is again a suitable localized function that recovers the Bloch wave exactly. Additionally, any eigenstate, as the Bloch wave is, is defined up to some phase. For generality, the Bloch wave is therefore multiplied by a phase $\exp\big(i\theta(\boldsymbol{k})\big)$. Now the localized function that exactly recovers the given Bloch wave, named the Wannier function, is obtained by a Fourier transformation:

$$\omega_\tau(\boldsymbol{r}-\boldsymbol{R}) = \sqrt{\frac{1}{V}} \sum_{\boldsymbol{k}} \exp\big(i\theta(\boldsymbol{k})\big) \exp(-i\boldsymbol{k}\boldsymbol{R})\, \phi_{k,\tau}(\boldsymbol{r}) \tag{44}$$

The freedom of the phase that was introduced can now be used to tune the properties of the Wannier functions. One can for example choose the function $\theta(\boldsymbol{k})$ such that the expectation value of $\boldsymbol{r}^2$, $\langle \omega_\tau | \boldsymbol{r}^2 | \omega_\tau \rangle$ is minimized, meaning that a maximally localized Wannier function is searched.

By construction, Wannier functions also remove the problem of non-orthonormality that was encountered before:

$$\begin{aligned}\langle \omega_{\boldsymbol{R},\tau} | \omega_{\boldsymbol{R}',\tau'} \rangle &= \frac{1}{V} \sum_{k,k'} \exp\big(i(\boldsymbol{k}'\boldsymbol{R}' - \boldsymbol{k}\boldsymbol{R})\big) \langle \phi_{k',\tau'} | \phi_{k,\tau} \rangle \\ &= \frac{1}{V} \sum_{k} \exp\big(i\boldsymbol{k}(\boldsymbol{R}' - \boldsymbol{R})\big)\, \delta_{\tau,\tau'} = \delta_{\boldsymbol{R},\boldsymbol{R}'} \delta_{\tau,\tau'}\end{aligned} \tag{45}$$

Generalization to Non-Orthogonal Bases and Arbitrary Lattices

The above considerations of the Tight Binding model are already quite powerful, however for the purpose of this thesis the concept has to be generalized. Following mainly e.g. Ref [58], let us consider for a general case the stationary Schrödinger equation with its full Hamiltonian H

$$H|\Psi\rangle = E|\Psi\rangle \tag{46}$$

The full Hilbert space of H is generally infinite dimensional, which can be unpractical for applications. There are even more complications. First, the full basis of the Hilbert space is often not even known due to the complexity of general systems. Also, the previous considerations are only applicable for periodic systems. However, general systems, especially organic materials are not periodic at all, so the Bloch wave ansatz is not applicable. And lastly, what was already problematic before, the basis of even a subspace can be non-orthogonal.

To approach this scenario, first assume a fictional non-orthogonal full basis of the Hilbert space $\{|\phi_\alpha\rangle\}$. We can define a reciprocal basis $\{|\phi^\alpha\rangle\}$ through the relation $\langle \phi^\alpha | \phi_\beta \rangle = \delta_{\alpha\beta}$. With the full basis, the unity operator can be defined as

$$I = \sum_{\alpha} |\phi_\alpha\rangle\langle\phi^\alpha| \tag{47}$$

The basis elements define the overlap matrix S

$$S_{\alpha\beta} = \langle \phi_\alpha | \phi_\beta \rangle \quad S^{\alpha\beta} = \langle \phi^\alpha | \phi^\beta \rangle = (S^{-1})_{\alpha\beta} \tag{48}$$

In terms of the overlap matrix, the original and the reciprocal basis can be related as

$$|\phi^\alpha\rangle = \sum_{\beta} S^{\beta\alpha} |\phi_\beta\rangle \qquad |\phi_\alpha\rangle = \sum_{\beta} S_{\beta\alpha} |\phi^\beta\rangle \tag{49}$$

One can now formally split the Hilbert space into two complementary subspaces $\mathcal{P}$ and $\mathcal{Q} = I - \mathcal{P}$. The overlap matrix can then be written in a block matrix form

$$S = \begin{pmatrix} S_{PP} & S_{PQ} \\ S_{QP} & S_{QQ} \end{pmatrix} \tag{50}$$

where $(S_{PP})_{pp'} = \langle \phi_p | \phi_{p'} \rangle$ with $|\phi_p\rangle, |\phi_{p'}\rangle \in \mathcal{P}$, $(S_{PQ})_{pq} = \langle \phi_p | \phi_q \rangle$ with $|\phi_p\rangle \in \mathcal{P}, |\phi_q\rangle \in \mathcal{Q}$ and so on. With the projection operator P defined as

$$P = \sum_{p \in \mathcal{P}} |\phi^p\rangle\langle\phi_p| \tag{51}$$

one can then project the state $|\Psi\rangle$ onto the subspace $\mathcal{P}$ and calculate the Schrödinger equation in the projected space $\mathcal{P}$

$$HP|\Psi\rangle = EP|\Psi\rangle \tag{52}$$

After some calculation one can represent the projected Schrödinger equation with an effective Hamiltonian that depends on the eigenvalue E

$$\begin{aligned} H^{eff}(E)\boldsymbol{c}_P &= E\boldsymbol{c}_P \\ H^{eff}(E) &= S_{PP}^{-1}\Big(H_{PP} + \big(ES_{PQ} - H_{PQ}\big)\big(ES_{QQ} - H_{QQ}\big)^{-1}\big(ES_{QP} - H_{QP}\big)\Big) \end{aligned} \tag{53}$$

where $(H_{PP})_{pp'} = \langle \phi_p | H | \phi_{p'} \rangle$ with $|\phi_p\rangle, |\phi_{p'}\rangle \in \mathcal{P}$ and analogously H_{PQ} and H_{QP}. The projected eigen vector components are defined via $(\boldsymbol{c}_P)_p = \langle \phi^p | \Psi \rangle$. The restricted Schrödinger equation above can alternatively be written as

$$H_L^{eff}(E)\boldsymbol{c}_P = ES_{PP}\boldsymbol{c}_P \tag{54}$$

referring to $H_L^{eff}(E) = H_{PP} + \big(ES_{PQ} - H_{PQ}\big)\big(ES_{QQ} - H_{QQ}\big)^{-1}(ES_{QP} - H_{QP})$ as the Löwdin Hamiltonian. Since the $\mathbf{c}_P$ are not orthogonal, one can now perform a Löwdin transformation

$$\Big(H_L^{eff}(E)\Big)' = S_{PP}^{-\frac{1}{2}} H_L^{eff}(E) S_{PP}^{-\frac{1}{2}} \qquad \boldsymbol{c}'_P = S_{PP}^{1/2}\boldsymbol{c}_P \tag{55}$$

to obtain the orthogonalized eigenvalue problem

$$\Big(H_L^{eff}(E)\Big)' \boldsymbol{c}'_P = E\boldsymbol{c}'_P \tag{56}$$

The Löwdin transformation gives the closest orthogonal representation to the localized non-orthogonal basis $\{|\phi_p\rangle\}$. Of course, the implicit dependency of the Löwdin Hamiltonian on the energy is computationally restrictive. However, if one chooses E to be around the region of

interest, like the center of DOS at E_0, one gets a good approximation of the eigenvalue spectrum around E_0 by

$$\left(H_L^{eff}(E_0)\right)' \boldsymbol{c}'_P = E\boldsymbol{c}'_P \tag{57}$$

So far, the problem was basically only rewritten and we still have the problem of the lacking knowledge of the basis states of $\mathcal{Q}$. The idea is now to truncate the Hilbert space towards only the subspace $\mathcal{P}$, meaning that all $\mathcal{Q}$ dependent terms are ignored and just keep $H_L^{eff}(E_0) \rightarrow H_{PP}$. This is the tight binding approximation. But since we possibly ignore important features hidden in $\mathcal{Q}$, the accuracy of the tight binding approximation is crucially dependent on the proper choice of the subspace $\mathcal{P}$. Usually, the choice of $\mathcal{P}$ are the basis states that are believed to be most relevant for the physics of interest, in OSCs this could be the HOMOs or LUMOs.

Before going into the actual calculation of the tight binding parameters, first the general OSC model Hamiltonian is introduced.

General Model Hamiltonian of Organic Semiconductors

In this section (mainly following[36], also reproduced from my Master thesis[55]), organic semiconductors will be studied from a quite general model Hamiltonian which captures the most relevant properties and it is the starting point for many theoretical and numerical studies.

The proposed Hamiltonian[36,59,60] is divided into several terms:

$$H = H_e^0 + H_{ph}^0 + H_e^{tr} + H_{e-ph}^{loc} + H_{e-ph}^{non} + H_e^{stat} \tag{58}$$

The first term describes the electron energy E_n^0 of N electrons in a perfectly ordered lattice without any interactions

$$H_e^0 = \sum_n^N E_n^0 a_n^\dagger a_n \tag{59}$$

The second term describes free phonons (bosonic quasiparticles emerging from quantization of lattice distortions)

$$H_{ph}^0 = \sum_{\boldsymbol{q},j} \hbar\omega_{\boldsymbol{q},j}\left(b_{\boldsymbol{q},j}^\dagger b_{\boldsymbol{q},j} + \frac{1}{2}\right) \tag{60}$$

where $\hbar\omega_{\boldsymbol{q},j}$ is the energy of the phonon mode on branch j with wavevector q. The $b^{\dagger}_{\boldsymbol{q},j}, b_{\boldsymbol{q},j}$ are the phonon creation and annihilation operators.

So far, no interactions and no transport is introduced. Electronic transfer from molecule m to molecule n by the transfer integral $J_{mn} = \langle\psi_n(\boldsymbol{r}-\boldsymbol{R}_n)|H_e^{tr}|\psi_m(\boldsymbol{r}-\boldsymbol{R}_m)\rangle$ is given by

$$H_e^{tr} = \sum_{m\neq n}^{N} J_{mn} a_n^{\dagger} a_m \tag{61}$$

The next two terms describe the local and non-local electron-phonon interactions in first order. Local means that the interaction does not lead to scattering onto a different molecule (intramolecular interaction), whereas non-local is, therefore, an electron-phonon scattering by intermolecular interactions involving the scattering of electrons onto a different molecule. The local term is

$$H_{e-ph}^{loc} = \frac{1}{\sqrt{N}} \sum_{\boldsymbol{q},j} \sum_{m}^{N} \hbar\omega_{\boldsymbol{q},j} \left(g_m(\boldsymbol{q},j) b_{\boldsymbol{q},j} + g_m^*(\boldsymbol{q},j) b^{\dagger}_{-\boldsymbol{q},j} \right) a_m^{\dagger} a_m \tag{62}$$

And the non-local term is

$$H_{e-ph}^{non} = \frac{1}{\sqrt{N}} \sum_{\boldsymbol{q},j} \sum_{\substack{m,n \\ m\neq n}}^{N} \hbar\omega_{\boldsymbol{q},j} \left(g_{nm}(\boldsymbol{q},j) b_{\boldsymbol{q},j} + g_{nm}^*(\boldsymbol{q},j) b^{\dagger}_{-\boldsymbol{q},j} \right) a_n^{\dagger} a_m \tag{63}$$

The g_m and g_{mn} are the local and non-local electron-phonon couplings respectively. Equation (62) is known as *diagonal dynamic disorder*, whereas Equation (63) is the *off-diagonal dynamic disorder*. Dynamical disorder is also called *thermal disorder* since the dynamic lattice distortions are due to thermal movement of the molecules. The effect of the electron-phonon interaction is that there are no pure electronic eigenstates. Electrons are always accompanied by phonons, which are lattice distortions. From this coupling, quasi particles emerge, which are called *polarons*, that is, a charge surrounded by a phonon cloud. The effect gets larger the stronger the coupling becomes. Typically, for organic semiconductors, the coupling is quite high, which in addition to the low dielectric constant of about $\epsilon_r \approx 3$ [61–63] for low doping, which is a measure of the ability of the medium to screen charges ($\epsilon_r > 10$ in inorganic semiconductors), leads to a polarization of the molecule where the charge resides[36]. The charges energy is then reduced by the polarization energy it created, which for low transfer

integral compared to the coupling is given[59] by $E_{pol}^{loc} = -\frac{1}{N}\sum_{\boldsymbol{q},\boldsymbol{j}} \hbar\omega_{\boldsymbol{q},j}|g_{nm}(\boldsymbol{q},j)|^2$, and traps itself, leading to a localized polaron, the *small polaron.* If the interaction is long-range (untypical for organics), the resulting polaron is more delocalized, forming a *large polaron.* If the transfer integrals J_{mn} are large compared to the electron-phonon couplings, the charge transport in the medium gets band-like, whereas when its small, hopping between localized states is the main charge transport mechanism.

So far, the lattice is perfectly periodic, which of course is not the usual case in organic semiconductors. In realistic scenarios, the molecules or polymer chains are quite disordered. Therefore, one introduces another term into the Hamiltonian, the so-called *static disorder*, which describes the variation of on-site energy, δE_n, due to the variations in the chemical vicinity of the respective molecule and variations in lattice potential due to the mainly static distortions in the 'lattice'. Since the transfer integral is mainly determined by the frontier orbital distances and their orientation, the random distortions in the molecular 'lattice' also introduce variations in the transfer integrals, δJ_{mn}. The latter is the *off-diagonal disorder*, whereas the former is called *diagonal disorder.* The term reads

$$H_e^{stat} = \sum_{n}^{N} \delta E_n a_n^\dagger a_n + \sum_{\substack{m,n \\ m\neq n}}^{N} \delta J_{mn} a_n^\dagger a_m \tag{64}$$

In disordered polymer-based materials, the static disorder is much more important than the dynamical disorder due to their high molecular mass (therefore slow thermal motion). Dynamic disorder becomes important though, if the conjugated polymers are highly ordered, and also, again due to their small molecular mass, it is important in small molecules[13].

Most studies however don't utilize the whole general Hamiltonian. Especially for large molecular mass OSCs like conjugated polymers, one can neglect the dynamic disorder since thermal motions become very slow in comparison to electronic time scales and use only the electronic Hamiltonian

$$H = H_e^0 + H_e^{stat} + H_e^{tr} \tag{65}$$

for charge transport simulations and calculations, as also done in this thesis. The next session discusses the parametrization of this tight binding model.

Tight Binding Parametrization and Transfer Integrals

To parametrize the tight binding model, one needs to find a suitable basis and calculate the transfer integrals of the whole system. A physically intuitive basis for tight binding models of OSCs are the localized frontier orbitals of the molecules that are mainly responsible for charge transport, i.e. HOMO or LUMO orbitals. In principle, one could perform exact DFT calculations of a whole system with its Kohn-Sham-Fock-Operator or Kohn-Sham Hamiltonian H, calculate the HOMO or LUMO orbitals of localized fragments of the system forming the localized basis of the system and calculate the transfer integrals $J_{AB} = \langle \phi^A | H | \phi^B \rangle$ between localized fragments A and B. However, the calculation of large systems using DFT is computationally prohibitive. One could make a first approximation by just considering the Hamiltonian of the dimer system A and B and calculating the frontier orbitals of A and B to calculate the transfer integral $J_{AB} = \langle \phi^A \big| H^{dim} \big| \phi^B \rangle$. This so-called dimer approximation is widely used for multi-scale simulations. It is however still computationally very expensive, since for large systems a very large number of molecular dimer configurations that the investigated system splits into, has to be calculated via DFT, so this approach is still limited to small systems. If one also wants to include thermal or dynamic disorder, it gets even more complicated. Some approaches utilizing DFT for transfer integral calculations were given in the introduction. One can further reduce the computational effort of transfer integral calculations with the ZINDO[16] approximation, which is deduced by approximations of the unrestricted Hartree-Fock equations. The Hartree-Fock equations are deduced by variation of the full Hamiltonian of the multi-electron system and translate the complex Schrödinger equation to a system of effective one-electron equations. Hereby, the Hamiltonian is replaced by the Fock-operator F^α and one obtains a system of equations for one-electron wavefunctions or molecular orbitals $\phi_i^\alpha = \sum_\mu c_{i\mu}^\alpha \chi_\mu$ in the localized atomic orbital basis $\{\chi_\mu\}$ which are the columns of the matrix C^α for spin α respectively

$$F^\alpha C^\alpha = C^\alpha \epsilon^\alpha$$
$$F^\alpha = h + \sum_j \left(J_j - K_j^\alpha \right) \tag{66}$$

such that the Fock operator consists of a single particle Hamilton operator h containing the kinetic energy and electron-core potential, the Coulomb interactions J_j and the exchange terms K_j^α. ZINDO makes approximations to the Fock-operator F to reduce the high

computational effort required for the full Fock operator. It neglects certain overlap integrals and two-electron integrals or replaces them by empirically deduced constants or parameters. For the calculation of the transfer integral between the frontier orbitals (e.g. HOMOs) of molecules A and B one needs to calculate $J_{AB} = \langle \phi^A_{HOMO} | F | \phi^B_{HOMO} \rangle = \sum_{\mu\nu} a^*_\mu b_\nu \langle \mu | F | \nu \rangle$ for $\mu \in A, \nu \in B$ and therefore the Fock matrix elements $F_{\mu\nu} = \langle \mu | F | \nu \rangle$ in the basis $\{\chi_\mu\}$. In the ZINDO approximation, these elements are given as

$$F_{\mu\nu} = S_{\mu\nu} \frac{\beta_A + \beta_B}{2} + P_{\mu\nu} \frac{\gamma_{AB}}{2} \tag{67}$$

where $S_{\mu\nu} = \langle \mu | \nu \rangle$ are the atomic overlaps, β_A the ionization potential of molecule A and $P_{\mu\nu} = \sum_a C_{\mu a} C_{\nu a} n_a$ are the elements of the density matrix (occupation number n_a). The $\gamma_{AB} \propto \frac{1}{R_{AB} + \delta}$ is the two-electron Coulomb integral in the Mataga-Nishimoto formalism with the empirical parameter δ and molecular distance R_{AB}. As Kirkpatrick et al.[64] argue, for symmetric molecules A and B, like if A and B are the same molecule, the density matrix elements $P_{\mu\nu}$ can approximately be neglected since $|\mu\rangle, |\nu\rangle$ are localized on different molecules. It follows that $F_{\mu\nu} \propto S_{\mu\nu}$ and therefore the transfer integral $J_{AB} \propto S_{AB}$ is approximately proportional to the molecular overlap between A and B. This approximation is called Molecular Orbital Overlap (MOO) and can dramatically reduce the computational effort of transfer matrix calculations.

One can even further simplify this approach by the Analytic Overlap Method[65] (AOM) by projecting the molecular orbitals onto a minimal Slater type basis set and analytically calculate the overlaps. They find over a wide range of distances a proportionality between the molecular overlap and the transfer integral calculated by high level ab initio reference calculations.

Tight Binding Model of this Thesis

These findings motivate the following tight binding model parametrization that is used throughout this thesis

$$H = \sum_n \epsilon_n a_n^\dagger a_n - \sum_{\langle n,m \rangle} f_{nm} \cdot \hbar\nu_0 \langle \phi_n | \phi_m \rangle a_n^\dagger a_m + \sum_n \langle \phi_n | V | \phi_n \rangle a_n^\dagger a_n + \sum_{\langle n,m \rangle} \langle \phi_n | V | \phi_m \rangle a_n^\dagger a_m \tag{68}$$

Here, ϵ_n is the diagonal disorder or on-site energy. Sometimes, ϵ_n is directly approximated from the force field if MD is used for morphology generation. However, due to the macroscopic randomness of the diagonal disorder, here it is assumed that they are gaussian distributed, i.e. $\epsilon_n \sim \mathcal{N}(\mu, \sigma)$ with mean $\mu = 0$ and disorder σ. The transfer integral $J_{nm} = (-) f_{nm} \cdot \hbar\nu_0 \langle \phi_n | \phi_m \rangle$ is proportional to the molecular overlap with scaling factor $\hbar\nu_0$ and f_{nm} is another scaling factor for special relations between molecular pairs n and m like intra-chain connection. The sum is over neighbors $\langle n, m \rangle$ with distance $\leq R_{cut}$.

Both on-site energies and transfer integrals are corrected in the presence of dopant ions that add the Coulomb interaction terms $\langle \phi_n | V | \phi_n \rangle$ and $\langle \phi_n | V | \phi_m \rangle$, which get treated explicitly here. Since periodic boundary conditions are applied, for the calculation of the Coulomb potential $N_{shell} = 5$ periodic shells of the simulation box are considered. At a point **r** within the simulation box, all Coulomb potentials of each counter-ion within the with N_{shell} periodic shells extended simulation box are added. To maintain charge neutrality, the potential of an oppositely charged homogeneous and spherical charge distribution is subtracted, treating the charge-charge interaction as single-particle interaction with an effective mean background. Denoting V_{shells} as the extended simulation box and Q the total counter-ion charge within V_{shell}, the radius of the homogeneously charged sphere is

$$\frac{4\pi}{3} R_{eq}^3 = V_{shell} \quad \Leftrightarrow \quad R_{eq} = \left(\frac{3 V_{shell}}{4\pi} \right)^{\frac{1}{3}} \tag{69}$$

The charge density of the sphere is $\rho_0 = -Q / V_{shell}$. The potential at a point **r** within the sphere is calculated via

$$V_{bg}(\boldsymbol{r}) = \frac{1}{4\pi\epsilon_0\epsilon_r} \int \frac{\rho_0}{|\mathbf{r} - \mathbf{r}'|} \, \mathrm{d}\boldsymbol{r}' = \frac{\rho_0}{6\epsilon_0\epsilon_r} \left(3R_{eq}^2 - r^2 \right) \tag{70}$$

The effective Coulomb potential, the charge *e* is interacting with, is now calculated as

$$V(\boldsymbol{r}) = \sum_{\boldsymbol{r}_{Ion} \in V_{shell}} \frac{e q_{Ion}}{4\pi\epsilon_0\epsilon_r} \frac{1}{\min(|\boldsymbol{r}_{Ion} - \boldsymbol{r}|, r_{min})} + eV_{bg}(\boldsymbol{r}) \tag{71}$$

Here, a cutoff distance $r_{min} = 2a_{typ}$ of the Coulomb potential of the counter-ions was introduced to mimic the finite potential depth of a charged dopant, with a_{typ} being the lattice constant for lattice-based morphologies.

As non-orthogonal basis, HOMO or LUMO orbitals ϕ_n of monomer units are used. For simplicity, in this thesis these are approximated as exponentially decaying ellipsoids

$$\phi_n(\boldsymbol{r}) = \langle \boldsymbol{r} | \phi_n \rangle = \frac{1}{\sqrt{\pi l_x l_y l_z}} \exp\left(-\sqrt{\left(\frac{x}{l_x}\right)^2 + \left(\frac{y}{l_y}\right)^2 + \left(\frac{z}{l_z}\right)^2} \right) \tag{72}$$

with the orbital decay lengths $l_{x,y,z}$ in the x- ,y- and z-directions. However, above orbital is centered at zero and oriented along the cartesian axes. Therefore, the monomer center coordinates and the orbital orientations need to be adjusted.

From the MD morphology output, for every monomer-core, i.e. neglecting side chains, the geometrical center of mass of all constituent atoms is taken as the monomer center coordinates $\boldsymbol{r}_i = \sum_{n \in core} \boldsymbol{r}_n \,/\, \sum_{n \in core} 1$. Additionally, a plane containing the monomer center $\boldsymbol{r}_i$ can be fitted to the atoms constituting the monomer-core. The normal vectors $\hat{\boldsymbol{n}}_i$ of these planes are one orientation vector the monomer units. By projecting the coordinates $\boldsymbol{r}_S$ of a specific atom of a monomer unit onto the monomers plane, like the S atom of thiophene, the normalized vector pointing from the monomer center to the projected point is the second orientation vector $\hat{\boldsymbol{s}}_i$ of a monomer unit, $\hat{\boldsymbol{s}}_i \cdot |\mathbf{s}_\mathrm{i}| = (\mathbf{r}_\mathrm{S} - \boldsymbol{r}_i) - [(\boldsymbol{r}_S - \boldsymbol{r}_i) \cdot \hat{\boldsymbol{n}}_i] \cdot \hat{\boldsymbol{n}}_i$.

The orientation is completed by a third orientation vector defined by the cross product $\hat{\boldsymbol{n}}_i \times \hat{\boldsymbol{s}}_i$. These three unit vectors define a rotation matrix

$$R_i = [\hat{\boldsymbol{s}}_i, \hat{\boldsymbol{n}}_i \times \hat{\boldsymbol{s}}_i, \hat{\boldsymbol{n}}_i] \tag{73}$$

The reoriented and translated orbital is then calculated via the transformation $\phi_i(R_i \cdot \boldsymbol{r} + \boldsymbol{r}_i)$.

For intra-chain coupling between neighboring monomers n and m, the scaling factor f_{nm} is applied if the angle between the monomers is less than a critical angle $\theta_0 < 40°$. Above this empirical critical angle here it is assumed that the conjugation of the polymer breaks (defect).

For a morphology generated by the 3-phase model, the same procedure is applied. However, no center of mass needs to be calculated, since the morphology is lattice based, with each lattice site corresponding to a monomer unit such that the lattice site coordinates are taken as the monomer center coordinates. In the 3-phase model morphologies, reduced diagonal disorder in aggregated regions in contrast to amorphous regions can be modeled. The interaction energy landscape of the monomers define regions of lower and higher energies. Aggregated regions will have lower energy, therefore a monomer is taken to be located within an aggregate if its interaction energy is below some threshold (e.g. $E_{int} < 0.3$ on a normalized energy scale). To mimic the lower diagonal disorder, the on-site energy of monomers within aggregates can be drawn from a gaussian distribution with different disorder $\sigma_{agg} < \sigma_{am}$. Since within real aggregates the molecular packing is better, the electronic coupling is enhanced there. However, since the model is lattice based and the lattice constant is constant, there are two possible workarounds to mimic enhanced electronic coupling. Either for neighboring sites that are both within an aggregate, a factor f_{nm} can be applied, or one enhances the l_z orbital parameter to model better coupling through $\pi - \pi$ stacking. This will on average enhance the coupling within aggregates, but also induces higher average coupling in the amorphous phase, albeit less than in the aggregated phase. For the lattice-based model, it is also possible to add positional disorder in the amorphous phase by adding small distortions in random directions to each site within the amorphous phase.

Lastly, for the annealed morphology model the situation is different. It gives only coordinates of guest sites and host sites. The guest sites are considered sites within aggregates, whereas host sites are part of the amorphous phase, but there is no orientation given. To work around that, orientations are attributed artificially. Guest sites are all oriented in the same direction. Host sites however get attributed a random direction. With site orientations attributed in this way, the rest is the same as with the 3-phase model, with the only difference that there is no information about a site belonging to a polymer chain.

Density of States

After setting up the tight binding Hamiltonian *H*, the Hamiltonian is diagonalized. Since the TB model is built on a non-orthogonal basis, instead of the classical eigenvalue problem, the generalized eigenvalue problem needs to be solved

$$HC = ESC \tag{74}$$

with the overlap matrix *S*. The matrix *C* contains the eigenvectors in the non-orthogonal basis in the columns. This is equivalent of solving the orthogonalized eigenvalue problem via the Löwdin transformation $H = S^{-1/2}HS^{-1/2}$ and $C' = S^{1/2}C$, as discussed previously. The result is the eigenvalues *E* of the wavefunctions of the TB Hamiltonian and their respective wavefunctions, either in the orthogonalized basis or the non-orthogonal basis. The eigenvalue spectrum is called the Density of states (DOS). It will be studied in the results for different scenarios.

One can also look at the DOS from an analytical perspective, which will be done in the following.

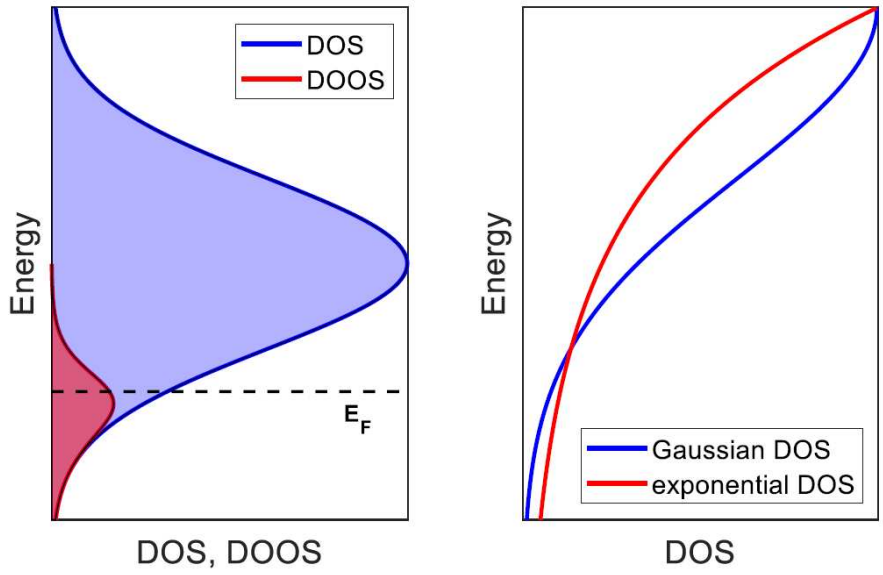

Figure 5 - Left: DOS and DOOS of gaussian disorder. Right: Comparison between exponential and gaussian DOS.

The simplest and mostly used effective model for the energy distribution in OSCs assumes gaussian distributed energies and is therefore referred to as the *Gaussian Disorder Model* (GDM). The intrinsic disorder is therefore described by[36]

$$g_{GDM}(E) = \frac{N}{\sqrt{2\pi\sigma_{GDM}^2}} \exp\left(-\frac{(E-E_0)^2}{2\sigma_{GDM}^2}\right) \tag{75}$$

and is illustrated in blue in **Figure 5.** Hereby, E_0 is the mean, which is usually the mean HOMO or LUMO energy of the OSC and σ_{GDM} is the energy variance called the disorder energy. The disorder takes values around $\sigma_{GDM} \approx 75\ meV$ [59,66], a value that also can be as much as double of this value in the case of very disordered OSCs. For experimentally relevant charge densities however, only the energetic tail states are relevant. The physical occupation of the states is described by *density of occupied states* (DOOS), $DOOS(E) = g(E)f(E, E_F, T)$, with the Fermi-Dirac distribution as function of the Fermi energy E_F and temperature T

$$f(E, E_F, T) = \frac{1}{1 + \exp\left(\frac{E-E_F}{k_B T}\right)} \tag{76}$$

and is also shown in **Figure 5**. The Fermi energy and the thermal energy $k_B T$ set two characteristic energy scales in the system. Another characteristic energy of a system is given by the energy expectation value for the energy w.r.t. the DOOS

$$\langle E \rangle = \frac{\int_{-\infty}^{\infty} E g(E) f(E) \mathrm{d}E}{\int_{-\infty}^{\infty} g(E) f(E) \mathrm{d}E} = -\frac{\sigma_{GDM}^2}{k_B T} \tag{77}$$

where the last equation is for $E_0 = 0$ and for low charge concentrations.

For low to intermediate charge concentrations, especially in doped systems, the relevant tail of the DOS can be modeled to be exponential[36]

$$g(E) = \frac{N}{k_B T} \exp\left(-\frac{E}{k_B T_0}\right) \tag{78}$$

with the *characteristic trap temperature* T_0, for $E \geq 0$ and p-type doping. For n-type doping, the sign of E is flipped. In this model, the energy expectation value is determined to be $\langle E \rangle = k_B T_0/(1 + T_0/T)$. The exponential DOS is however not a good model for undoped systems, since it yields a dispersive (time-dependent) mobility for dilute systems, or systems with very low charge density, which is experimentally not observed[67].

To see how an exponential tail can emerge in doped systems from an intrinsic gaussian distribution, Arkhipov[68] developed a model that modifies the GDM tail due to the introduction of Coulomb-traps from doping counter ions, which got later refined to include differences in HOMO/LUMO levels of the semiconductor and the dopant[69]. The model assumes low dopant concentrations such that one can assume that only one dopant ion influences the considered charge near the ion, but can be used for a wider range of dopant concentrations. The following summary of the derivation was already formulated in my Master thesis[55] and therefore adopted here.

Arkhipov describes the broadening of the DOS due to doping. The probability density of having a dopant ion in distance r to the considered intrinsic energy site is given by a Poisson distribution $w(r) = 4\pi r^2 N_d \exp(-4\pi N_d r^3/3)$ with dopant density N_d. Now the distribution of localized sites at $E_c = -e^2/4\pi\epsilon_0\epsilon_r r$ is

$$g_c(E_c) = w\big(r(E_c)\big)\left|\frac{dr}{dE_c}\right| \tag{79}$$

The modified DOS is then given by integrating the product of the intrinsic DOS and g_c with the energy condition $E = E_i + E_c$

$$\begin{aligned} g(E) &= \int_{-\infty}^{0} g_c(E_c)\mathrm{d}E_c \int_{-\infty}^{\infty} g_i(E_i)\delta(E - E_i - E_c)\mathrm{d}E_i \\ &= A\int_{-\infty}^{0} \frac{\mathrm{d}E_c}{E_c^4}\exp\left(\frac{A}{3E_c^3}\right) g_i(E - E_c) \end{aligned} \tag{80}$$

with $A = 4\pi e^6 N_d/(4\pi\epsilon_0\epsilon_r)^3$. The refined model makes two assumptions: 1) Although a counter ion induces a long-range potential, giving a local spatial dependence of energy levels, the whole vicinity of the counter ion is effectively treated as one deep trap state. 2) The new energy level of the trap state is given by the sum of the intrinsic energy level and the potential formed by the Coulomb potential of the nearest counter ion and an externally applied field, $E = E_i + \Delta$, $\Delta = (\sqrt{e^3 F/\pi\epsilon_0\epsilon_r} - e^2/4\pi\epsilon_0\epsilon_r a)$, where a is the distance of the nearest counter ion to the intrinsic energy site. The expression in the square root comes from inserting the radius that maximizes the sum of potential drop due to the external electric field and the Coulomb potential of the counter ion. Now, to accommodate for the energy difference $\Delta E = E_d - E_i$ of HOMO/LUMO of dopant and intrinsic semiconductor, in a radius of $a_{NN} = N_i^{-1/3}$ around the dopant ion, corresponding to a Coulomb energy $E_1 = E_c(a_{NN})$, the

intrinsic semiconductor is replaced by the dopant energy level E_d and the ion potential. Otherwise, the uncorrected broadened DOS Equation (80) is used. For vanishing electrical field, this gives rise to the expression[69,70]

$$g(E) = \left(1 - \frac{4\pi N_d}{3N_i}\right)\frac{g_1(E)}{\int_{-\infty}^{0} g_1(E)\mathrm{d}E} + \frac{4\pi N_d}{N_i}\frac{g_2(E)}{\int_{-\infty}^{0} g_2(E)\mathrm{d}E} \tag{81}$$

With the intrinsic charge density N_i and

$$g_1(E) = A\int_{E_1}^{0}\frac{\mathrm{d}E_c}{E_c^4}\exp\left(\frac{A}{3E_c^3}\right)g_i(E - E_c) \tag{82}$$

and

$$g_2(E) = A\int_{-\infty}^{E_1}\frac{\mathrm{d}E_c}{E_c^4}\exp\left(\frac{A}{3E_c^3}\right)g_i(E - \Delta E - E_c) \tag{83}$$

The result is shown in **Figure 6** for the GDM. Essentially, for higher doping concentration, the Coulomb potential of the dopant ions induces an exponential tail at the intrinsic Gaussian curve. As from this interpretation is expected and investigated in[70] a higher dielectric constant ϵ_r, meaning larger screening, makes the exponential tail vanish.

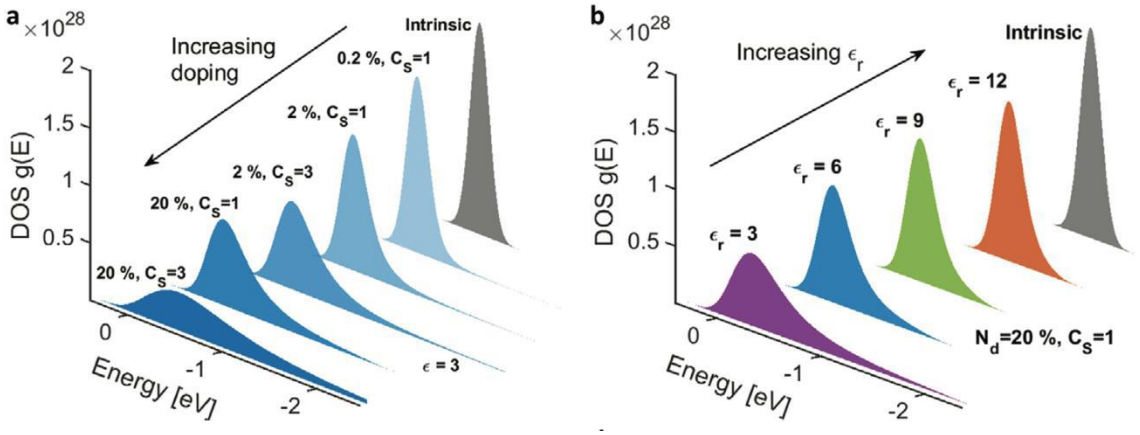

Figure 6 – a Formation of an exponential tail upon doping an initially gaussian DOS. **b** Vanishing of an exponential tail upon increasing the dielectric constant ϵ_r due to screening. Adapted from[70]. Licensed under CC BY 4.0 (https://creativecommons.org/licenses/by/4.0/).

In the results section, the DOS of doped DOS will be elaborated further and it will be shown that the TB model will also show another possible phenomenon in the DOS that occurs at higher doping concentration.

Localization

Localization Measures

Having obtained the energy of the states from the TB model describing the OSC system of interest, yet another extremely important property of OSCs needs to be investigated, namely wavefunction or Anderson localization. From the diagonalization of the TB Hamiltonian we obtain the wavefunctions in the orthogonalized basis C' and the non-orthogonal basis C. The localization of a wavefunction can be measured with the concept of the *Inverse Participation Ratio* (IPR). It is defined as[71]

$$IPR(E_i) = \frac{1}{\sum_n^N \left|c'_{in}\right|^4} \tag{84}$$

where E_i is the eigen energy of the i-th eigenstate with components c'_{in} in the orthogonalized basis. To understand the expression, one can look at two extreme cases. In the first case the wavefunction is localized on one site such that $c'_{in} = \delta_{ni}$. Here the IPR takes on the value 1. The other extreme case is a completely delocalized wavefunction over all N sites such that $c'_{in} = 1/\sqrt{N}$. Here, the IPR takes on the value N. This shows that the IPR is a measure of over how many sites the wavefunction is effectively delocalized. From that, a localization length α can be extracted via

$$\alpha(E_i) = \sqrt[3]{IPR(E_i)} \cdot a_{typ} \tag{85}$$

with $a_{typ} = \left(\frac{V}{N}\right)^{1/3}$ being the typical (average) inter-site distance of N sites in the volume V.

In this thesis a modification is introduced. The minimal value the IPR takes on is one, but physically the minimal value is the frontier orbital localization denoted as λ. Therefore, it is corrected via

$$\alpha(E_i) = \left(\sqrt[3]{IPR(E_i)} - 1\right) \cdot a_{typ} + \lambda \tag{86}$$

One problem with this definition of a localization length is that it is best defined for a regular lattice geometry. For unregular lattices, there can be deviations through this definition, since all sites are attributed the same volume, which is depicted in **Figure 7**.

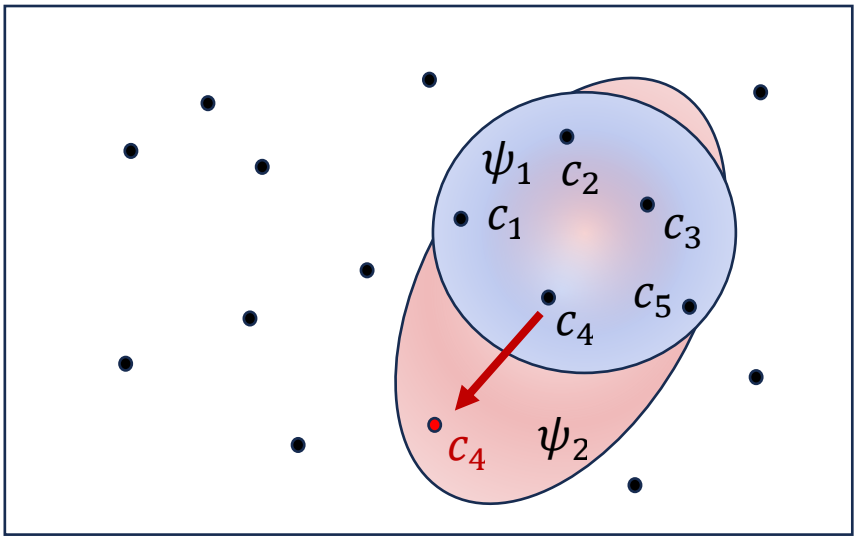

Figure 7 - Wavefunction localization in a random lattice of two wavefunctions ψ_1(blue) and ψ_2(red). The second lattice differs from the first (black) by shifting one site. The c_i are the components of the wavefunctions.

Assuming two wavefunction ψ_1 and ψ_2 in two random lattices, from which one differs from the other by shifting one site away. If the two wavefunctions are solely localized on the sites 1-5, i.e. components $c_i \neq 0$ and both have the same components $c_i(\psi_1) = c_i(\psi_2)$, one can have the situation that with the classical definition both wavefunctions would give the same IPR, albeit wavefunction ψ_2 covers a larger volume than ψ_1. A workaround can be the division of the lattice into distinct volumes that are attributed to each site. This can be done by the *Voronoi tessellation* (**Figure 8**).

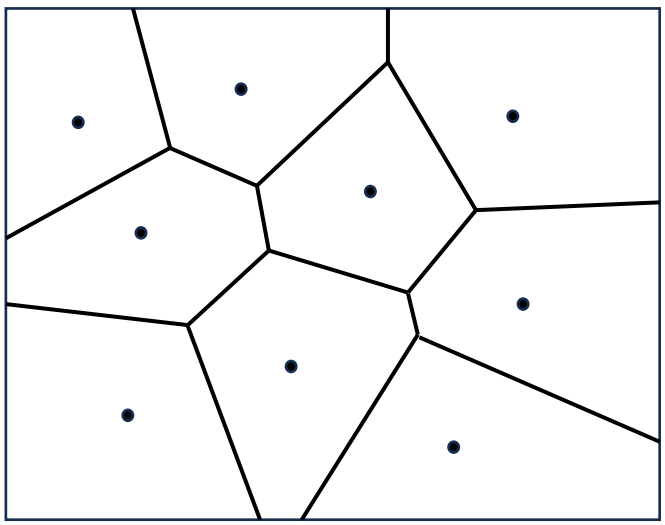

Figure 8 – Voronoi Tessellation of a random lattice in 2D.

The Voronoi tessellation is basically the same as the construction of a Wigner-Seitz cell. For every pair of neighboring sites, a hyperplane that is orthogonal to the connection line between two neighboring sites and crosses its mid-point is drawn. In that way, each site is contained in a polytope that is defined by the crossing hyperplanes. These polytopes are the Voronoi cells. Denoting V_i as the volume of the Voronoi cell of site i, one can construct a generalized IPR that weights each site with its Voronoi cell volume

$$IPR_{voronoi} = \left(\sum_i \frac{|c_i|^4}{V_i} \right)^{-1} \tag{87}$$

For regular lattices, all V_i become the same and the standard expression of the IPR is recovered. However, in the analyses of this thesis the definition Eq. (86) is used for consistency with a previous paper. In the SI, the two models are compared to each other.

For some applications, it can also be useful to study the anisotropy of wavefunctions. Therefore, here a possibility to do that is introduced. The aim is, to fit an ellipsoid to the wavefunction as an approximation of its spatial distribution in the lattice. A method to accomplish this is by using *Principal Component Analysis* (PCA). The procedure is as follows.

For a wavefunction ψ with components c_i on site i at position $\boldsymbol{r}_i$, the center of mass is calculated

$$\boldsymbol{\mu} = \frac{\sum_i^N \boldsymbol{r}_i |c_i|}{\sum_i^N |c_i|} \tag{88}$$

Now each point $\boldsymbol{r}_i$ is shifted by the center of mass, $\boldsymbol{r}_i' = \boldsymbol{r}_i - \boldsymbol{\mu}$. Then each point is weighted by its wavefunction component and all sites are put into one matrix

$$X = \begin{pmatrix} \boldsymbol{r}_1'^{\,t} \cdot |c_1| \\ \boldsymbol{r}_2'^{\,t} \cdot |c_2| \\ \vdots \\ \boldsymbol{r}_N'^{\,t} \cdot |c_N| \end{pmatrix} \tag{89}$$

Then the covariance matrix (3x3) is defined as $Cov = \frac{1}{N}(X^t X)$. Finally, the covariance matrix is diagonalized and the eigenvalues λ_i and the eigenvectors $\boldsymbol{v}_i$ are extracted. Geometrically, the square roots of the eigenvalues, $a = \sqrt{\lambda_1}$, $b = \sqrt{\lambda_2}$ and $c = \sqrt{\lambda_3}$, are the lengths of the fitted ellipsoid main axes and the eigenvectors are the corresponding axes directions, i.e. the

ellipsoid orientation. Finally, one needs to rescale the axes lengths such that the ellipsoid volume equals the IPR

$$\frac{4\pi}{3}abc \cdot s^3 = IPR \quad \Rightarrow \quad s = \left(3 \cdot \frac{IPR}{4\pi abc}\right)^{\frac{1}{3}} \qquad (90)$$
$$a \to a \cdot s, \quad b \to b \cdot s, \quad c \to c \cdot s$$

The following section deals with the physical reason of the wavefunction localization as was investigated in the literature.

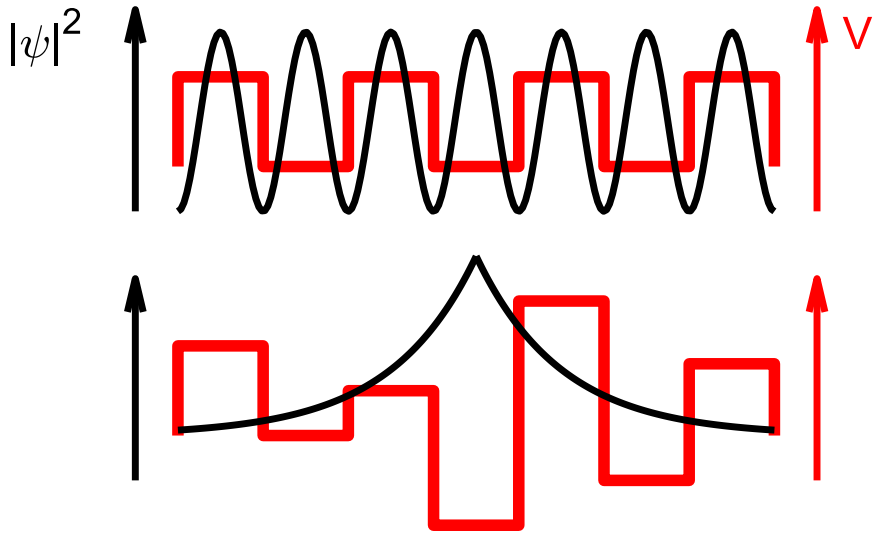

Figure 9 – Up: Blochwave in periodic potential. Down: Anderson localization in disordered potential.

Anderson Localization

(As already summarized in my Master thesis[55]) In 1958, P.W. Anderson published the work *Absence of Diffusion in Certain Random Lattices*[72], where he studied the wave function of a particle in a disordered lattice and found that, for a certain degree of disorder, wave functions become localized.

Anderson ultimately found out that the electronic wavefunction will decay exponentially with distance from its center of mass (initial site) $\psi(r) \propto \exp\left(-\frac{r}{\alpha}\right)$, where the decay-parameter α is the localization length if the disorder is larger than some threshold: $\frac{V}{W} < \left(\frac{V}{W}\right)_{crit}$, where V is the potential and W the disorder (see **Figure 9**). Besides that, the critical disorder is dependent on the eigenstate energy. This localization can be understood in terms of the

wavefunction being reflected at the lattice at a certain magnitude of the disorder so much that the probability amplitude of the wave function stays localized.

The transition from localization to delocalization can be studied by using Scaling Theory. As stated in[73], the conductance is studied at different length scales. They state that the conductance at a changed scale is a function of the previous scale and the scale itself. Assuming a box with side length L, the conductance is studied at scales bL. Mathematically speaking, the conductance g at scale bL has the form

$$g(bL) = f\big(b, g(L)\big) \tag{91}$$

Now a scaling parameter $\beta(g) = \mathrm{d}\ln(g)\,/\mathrm{d}\ln(L)$ is introduced to study the scaling behavior of the conductance. For large $g \to \infty$ Ohm's law is attained, from which the resistivity scales as

$$R = \rho\frac{L}{A} = \rho\frac{L}{L^{d-1}} = \rho L^{2-d} \tag{92}$$

where ρ is the specific resistivity and d is the dimension of the considered box. The conductance is therefore $G = \frac{1}{R} = \sigma L^{d-2}$ and from there $\beta = d - 2$.

For low conductance $g \to 0$, that is for sufficient disorder, from Anderson Localization it is known that the conductance will decay exponentially with distance, $g \propto \exp(-L/\alpha)$, and therefore $\beta = \ln(g) = -L/\alpha < 0$. From these rather simple considerations, one sees that $\beta \leq 0$ if $d \leq 2$, which means for dimensions smaller or equal to two, at macroscopic length scales $L \to \infty$, the macroscopic conductance will vanish even for very small disorder. For three dimensions, there is a turning point at g_c where $\beta(g_c) = 0$ and positive above so that above this critical behavior there is a transition to a well-conducting medium. This phenomenon is called *Anderson metal-insulator transition.*

As discussed in[13], localization in different morphologies can emerge in different ways. In polymers, the energy needed to rotate monomers around a bond is comparable with the thermal energy at room temperature such that rotations are a usual source of static disorder, breaking the symmetry of the otherwise straight polymer chain. The rotations disturb the periodic structure and potential of the polymer, causing potential variations in the vicinity of monomers. Rotations do not only change the angle between monomers within a polymer chain, they also change the angle to orbitals of neighboring polymer chains, which are

responsible for charge transfer. For example, the transfer integral in π-π stacking of polymers, that is the overlap of p_z orbitals, is dependent on the angle and the separation between each other.

One proposed model for conjugated polymers is the so-called *conjugation break model* [13]. It states that charges are delocalized over planar parts of the conjugated molecular backbone, where the transfer integrals are large enough. If now due to thermal energy a rotation of a monomer around a bond exceeds a critical angle such that the transfer integral becomes much weaker, it causes the charge to localize. This model would imply that closer to the band edge, which is defined by an infinitely large polymer chain, the charges are more delocalized since the chain is longer. However, simulations of Mladenovic and Vukmirovic[13] suggest the opposite behavior that charges are more localized near the band edge and more delocalized further away. It was found that the variation of on-site energies plays a dominant role for localization. The on-site energy was found to be reduced with alkyl side chains since due to the separation of monomers/polymers the variations in potential are less pronounced. Thereby, since the wavefunction is mainly localized on the molecular backbone, disorder in the alkyl side chains does play a minor role in the on-site energy disorder and localization. It was also suggested that polymers with strong built-in dipole moments within their monomers enhance the on-site disorder since, due to their larger dipole strength, variations are felt much more by neighboring monomers/polymers.

Polaronic effects could possibly also localize the wavefunctions, although this is controversial and may be material-dependent. On the one hand, the polarization energy that emerges due to the polarization of the molecules containing the charge traps the charge by lowering the energy, forming small polarons, but on the other hand, e.g. DFT calculations on straight polythiophene chains find negligible polaron binding energies of only a few meV [74,75].

Besides that, the polymer molecular weight influences the morphology, giving rise to semicrystalline-like structures containing crystalline regions, where the charge should be completely delocalized over, and connecting amorphous regions that rather localize the charge[13].

In small molecule polycrystals, grain boundaries are a localizing boundary of the electronic wavefunction. The grain boundaries provide trap states, where the charges localize. Again,

simulations[13] also found that the charges can also delocalize beyond the grain boundaries, but mostly just into one side of the grain boundary.

Summarizing, in both all considered cases, localization is a rather complicated and versatile phenomenon, and therefore a factor whose role should be considered in more detail in charge transport models.

Hopping Rates

With the state energies and the calculated localization lengths extracted from the TB model, all ingredients are given to construct the transfer rates or hopping rates for the later kinetic Monte Carlo simulations. In the following section, the two most used hopping rates, namely the Marcus rate and the Miller-Abrahams rate, will be discussed.

Miller Abrahams Rate

(Adopted and modified from the text about rates from my Master thesis[55]) The disordered nature of amorphous materials gives rise to strong scattering effects of the charge carriers such that for not too high thermal energies, the charge carriers reside in localized states. A similar situation was described by A. Miller and E. Abrahams in 1960 in their paper *Impurity Conduction at Low Concentrations*[4]. They studied the conductivity of n-type semiconductors at low n_D and low temperature. At low n_D, the concentration of impurities is too low for them to form in some kind of band, called impurity band, because the overlap between the states is too small. Additionally, the thermal energy at sufficiently low temperatures is not high enough to sufficiently delocalize the charge carriers to form a band. The conduction that still takes place is described by (phonon-assisted) *hopping* between localized states, which in their work were the impurities, i.e. donors and acceptors. Utilizing Fermi's golden rule, they arrived at an expression for the transition rate between two states at energies E_j and E_i separated by R_{ij} like

$$p_{ij} = \nu_0 \exp\left(-\frac{2R_{ij}}{\alpha}\right) \begin{cases} \exp\left(-\dfrac{\max\left(0, E_j - E_i - e\Delta \boldsymbol{x}_{ij}\boldsymbol{F}\right)}{k_B T}\right) & E_j > E_i \\ 1 & E_j < E_i \end{cases} \tag{93}$$

where ν_0 is the so-called *attempt-to-hop-frequency* and α is the localization length of the states. For amorphous materials the factor ν_0 is in the order of 10 THz and a typical phonon mode frequency. Therefore, it can be physically interpreted that on average after every time $\tau = 1/\nu_0$ a possible hopping event assisted by a phonon can take place. The first term $\exp\left(-\frac{2R}{\alpha}\right)$ can be interpreted as a tunneling probability, by which a charge can tunnel between the states E_j and E_i. The second factor is for $E_j > E_i + e\Delta\boldsymbol{x}_{ij}\boldsymbol{F}$ just the Boltzmann factor describing thermal excitation from the lower state to the higher state. The term $e\Delta\boldsymbol{x}_{ij}\boldsymbol{F}$ is the energy that a charge gains or loses hopping over a distance $\Delta\boldsymbol{x}_{ij}$ between the states i and j in the direction or against the field $\boldsymbol{F}$, similar to a voltage drop.

Marcus Rate

The Miller Abrahams expression is in that sense not quite correct for many organic materials since it neglects chemical details about the hopping process. Indeed, hopping in organics often involves non-negligible molecular reorganization, which lowers the energy by the *reorganization energy* λ_{reorg}. An elaborative approach via Fermi's Golden rule gives the Marcus hopping rate[5,36] as

$$k_{ET} = \frac{J^2}{\hbar}\left(\frac{\pi}{\lambda_{reorg}k_BT}\right)^{1/2}\exp\left(-\frac{\left(\lambda_{reorg}+\Delta G^0\right)^2}{4\lambda_{reorg}k_BT}\right) \tag{94}$$

The transfer integral J is often taken to be the transfer integral of a dimer system $\langle\phi_n|H_{dim}|\phi_m\rangle$ as discussed in the tight binding section. It can alternatively be modeled as in the case of the tunneling term in the Miller Abrahams rate. ΔG_0 is the change in the free energy between the metastable bound state between ionized donor and acceptor and the dissociated states. The Marcus hopping rate can in some cases predict qualitatively different results than the Miller Abrahams expressions, but often the consideration of the Miller-Abrahams hopping rate is sufficient, as a more complicated ansatz through the Marcus rate will often ultimately give similar results.

Generalized Transfer Rate

The models that were considered so far have one thing in common: They all assume a small and constant localization length parameter α, describing hopping between strongly localized states. In the recent past years, researchers indicated experimental discrepancies which could not be explained by the present models. One of these problems are unphysically high attempt-to-hop frequencies, e.g. of $\nu_0 \approx 6.3 \times 10^{20} s^{-1}$ for a localization length of 2 Å, using the Miller-Abrahams expression for the hopping rate [13] for pristine P3HT. In fact, such high frequencies are much higher than expected from even the highest phonon mode, as which ν_0 is sometimes interpreted as. Detailed computational analyses of conjugated polymers as P3HT, as studied in Ref.[13], used the theoretically full hopping rate W_{ij} at the scale of the carriers wavefunction to study the electronic transport, given by

$$W_{ij} = \pi \sum_q \frac{\left|M_{ij,q}\right|^2}{\omega_q} \left[\left(N_q + 1\right)\delta\left(E_i - E_j - \hbar\omega_q\right) + N_q \delta\left(E_i - E_j + \hbar\omega_q\right)\right] \tag{95}$$

with the phonon-mode q, the corresponding phonon-mode frequency ω_α and electron-phonon coupling $M_{ij,q}$ between two atoms i and j. N_q are the number of phonons (given by the Bose-Einstein distribution) and $\delta(E)$ is the Dirac delta functional. This expression is essentially Fermi's Golden Rule. Thereby, the Miller-Abrahams rate is recovered, if the electron-phonon coupling is said to be proportional to the wavefunction overlap and that the overlap decays exponentially with distance, which is in fact only a good approximation for spherically symmetric wavefunctions, and additionally if the energy dependence of the phonon DOS is completely neglected. The most crucial factor in this simplification turned out to be the details of the overlap, and secondary the effect of the phonon DOS.

Further, these detailed computational analyses of conjugated polymers such as P3HT have shown [13,14,27] that the assumption of strongly localized states has to be rethought. It is found that charge carriers can delocalize over multiple molecules or polymer chains, which is in strong contrast to the assumed strong localization. In fact, the first stated problem of unphysically high ν_0 vanished upon considering both localized and more delocalized states in the electronic transport[27]. Therefore, a physically correct and more realistic model of charge transport should include the effect of partially delocalized states.

In this thesis, the consideration of partially delocalized states is done by modifying the Miller-Abrahams rate as

$$p_{ij} = \nu_0 \exp\left(-R_{ij}\left(\frac{1}{\alpha_i}+\frac{1}{\alpha_j}\right)\right)\exp\left(-\frac{\max\left(0, E_j - E_i - e\Delta\boldsymbol{x}_{ij}\boldsymbol{F}\right)}{k_B T}\right) \tag{96}$$

Hereby, the localization lengths of state i and j are α_i and α_j respectively, calculated from the TB model as discussed before. The energies E_i and E_j are the corresponding eigen-energies of the states i and j calculated from the TB model. This expression converges to the classical Miller-Abrahams expression for $\alpha_i \to \alpha_j$ and allows for different wavefunction localizations of the states i and j. With this expression it is possible to model the local energetical and localization correlations of the considered morphology in a more realistic way.

The hopping rate is an essential ingredient for the kinetic Monte Carlo simulations that will be studied in detail in the following section.

Kinetic Monte Carlo Simulations

Detailed analytic calculations of charge transport in OSCs is beyond effective theories not possible, since the inherently disordered morphology of OSCs can be very diverse and there are no symmetries to reduce the complexity of the problem as for example in crystalline media. However, the fundamental charge transport mechanism in OSCs is hopping between localized states. This can be utilized to build a stochastic charge transport model for OSCs (see e.g. Ref.[76]).

The probability density to find a system in a state s at time t is given by $p(s,t)$. Let now $\{s_n\}_{n\geq 1}$ and $\{t_n\}_{n\geq 1}$ be sequences of system states s_n at corresponding times t_n with the initial configuration (s_1, t_1). The joint probability density of $\{s_n\}_{n\geq 1}$ at times $\{t_n\}_{n\geq 1}$ can be expanded using the chain rule of probability into a product of conditional probabilities

$$\begin{aligned} &p(s_n, t_n; s_{n-1}, t_{n-1}; \dots; s_1, t_1) \\ &= p(s_n, t_n | s_{n-1}, t_{n-1}; \dots; s_1, t_1) p(s_{n-1}, t_{n-1}; \dots; s_1, t_1) \\ &= p(s_n, t_n | s_{n-1}, t_{n-1}; \dots; s_1, t_1) p(s_{n-1}, t_{n-1} | s_{n-2}, t_{n-2}; \dots; s_1, t_1) \dots p(s_1, t_1) \\ &= p(s_n, t_n | s_{n-1}, t_{n-1}) p(s_{n-1}, t_{n-1} | s_{n-2}, t_{n-2}) \dots p(s_1, t_1) \end{aligned} \tag{97}$$

where in the last equation the *Markov property* $p(s_n, t_n | s_{n-1}, t_{n-1}; \dots; s_1, t_1) = p(s_n, t_n | s_{n-1}, t_{n-1})$ was used. This assumption is valid since we are dealing with uncorrelated hopping events in the charge transport, meaning that the state of a system is only determined

by its previous state. Differently speaking, the location of a charge after a hop is only determined by where it was sitting before, so it is “memoryless”. These kinds of processes are called *Markov chains*. The probability to find the system in any state $(s_i, t+\tau)$ after being in a state (s_j, t) after some time $\tau > 0$ is clearly unity

$$1 = \sum_i p\big(s_i, t+\tau \big| s_j, t\big) \tag{98}$$

The same holds for $\tau = 0$, however at an instant time the probability density to find a state (s_j, t) in a different state (s_i, t) must be zero, $p\big(s_i, t \big| s_j, t\big) = \delta_{ij}$, so it holds

$$1 = \sum_i p\big(s_i, t \big| s_j, t\big) = p\big(s_j, t \big| s_j, t\big) + \sum_{i \neq j} p\big(s_i, t \big| s_j, t\big) = p\big(s_j, t \big| s_j, t\big) \tag{99}$$

Subtracting Equ. (98) and Equ. (99) and dividing by τ, one arrives at

$$\begin{aligned} 0 &= \frac{p\big(s_j, t+\tau \big| s_j, t\big) - p\big(s_j, t \big| s_j, t\big)}{\tau} + \sum_{i \neq j} \frac{p\big(s_i, t+\tau \big| s_j, t\big) - p\big(s_i, t \big| s_j, t\big)}{\tau} \\ &= \frac{p\big(s_j, t+\tau \big| s_j, t\big) - 1}{\tau} + \sum_{i \neq j} \frac{p\big(s_i, t+\tau \big| s_j, t\big)}{\tau} \end{aligned} \tag{100}$$

With the definition of the transition rate

$$k_{ji} = \lim_{\tau \to 0} \frac{p\big(s_i, t+\tau \big| s_j, t\big) - p\big(s_i, t \big| s_j, t\big)}{\tau} \tag{101}$$

The last line of Equ. (100) can be written as

$$0 = k_{jj} + \sum_{i \neq j} k_{ji} \quad \Leftrightarrow \quad k_{jj} = -\sum_{i \neq j} k_{ji} \tag{102}$$

This result will be used in the next step.

Starting from time t, the probability density to find the system in a state s_j at time $t+\tau$ is given by the *Chapman-Kolmogorov equation*

$$p\big(s_j, t+\tau\big) = \sum_i p\big(s_j, t+\tau \big| s_i, t\big) p(s_i, t) \tag{103}$$

which describes the sum over configurations (s_i, t) to find the system in state $(s_j, t+\tau)$ given that it was in state (s_i, t) before. Now, $p(s_j, t+\tau)$ will be Taylor-expanded to first order around $\tau = 0$

$$
\begin{aligned}
& p(s_j,t) + \tau \cdot \frac{\mathrm{d}}{\mathrm{d}t} p(s_j,t) = \sum_i p(s_j, t+\tau | s_i, t) p(s_i, t) \\
& \Leftrightarrow \\
& \frac{\mathrm{d}}{\mathrm{d}t} p(s_j,t) = \sum_{i \neq j} \frac{p(s_j, t+\tau | s_i, t) p(s_i,t)}{\tau} + \frac{p(s_j, t+\tau | s_j, t) p(s_j,t)}{\tau} - \frac{p(s_j,t)}{\tau} \\
& \Leftrightarrow \\
& \frac{\mathrm{d}}{\mathrm{d}t} p(s_j,t) = \frac{p(s_j, t+\tau | s_j, t) - 1}{\tau} p(s_j,t) + \sum_{i \neq j} \frac{p(s_j, t+\tau | s_i, t)}{\tau} p(s_i,t) \\
& \Leftrightarrow \\
& \frac{\mathrm{d}}{\mathrm{d}t} p(s_j,t) = k_{jj} \cdot p(s_j,t) + \sum_{i \neq j} k_{ij} \cdot p(s_i,t) \\
& \Leftrightarrow \\
& \frac{\mathrm{d}}{\mathrm{d}t} p(s_j,t) = \sum_{i \neq j} \left(k_{ij} \cdot p(s_i,t) - k_{ji} \cdot p(s_j,t) \right)
\end{aligned}
\tag{104}
$$

where in the second last line the definition of the transition rate was used and in the last line the result of Equ. (102). The equation in the last line is the so-called *Master equation*. This system of differential equations describes the change of probability distribution of state s_j in time due to the difference of the hopping-flow out of state s_j into states s_i with rate k_{ji} and the hopping-flow from all possible states s_i into state s_j with rate k_{ij}.

The transition rate can be anything physically senseful, like the Marcus rate, Miller-Abrahams rate Equ. (93) or, as it is used here, the modified Miller-Abrahams rate Equ. (96).

In its analytical form, in the general case the Master equation is still very hard to solve. Here the idea of kinetic Monte Carlo (kMC) simulations comes in. kMC is the approach to solve the Master equation stochastically by stochastically simulating hopping paths and averaging over them. To see how that works, assume the system in an initial state s_j at time t, meaning that $p(s_i, t) = 0 \; \forall i \neq j$. For small Δt then the Master equation simplifies to

$$
\frac{\mathrm{d}}{\mathrm{d}t} p(s_j, t+\Delta t) = -\sum_{i \neq j} k_{ji} \cdot p(s_j, t) \tag{105}
$$

The probability that the system is still in the state s_j after time Δt is then given by integrating this equation

$$P_{stayed}(s_j, \Delta t) = \exp\left(-\int_t^{t+\Delta t} k_{tot}(s_j, \tau) d\tau\right) = \exp(-k_{tot}(s_j) \cdot \Delta t) \tag{106}$$

where the total rate is $k_{tot}(s_j, \tau) = \sum_{i \neq j} k_{ji}$ and it was assumed that the total rate is not time dependent, which is the case for the possible rates that are used within this thesis. This means that the hopping is a Poissonian process and the jumping times Δt are Poisson-distributed.

The kMC simulation process then works as follows. First, a simulation lattice is defined, which we get in our case from the TB model and MD simulations or other morphology generating schemes. If all charges would be solely localized on one monomer of the system, a good choice of lattice sites would be the monomer positions $\boldsymbol{r}_i$. However, from the TB model we get wavefunctions as states, that are mostly not solely localized on a single monomer and there is no mapping towards a unique monomer for each wavefunction. To solve this issue, a close lying solution would be to define the center of mass of each wavefunction as lattice site. Therefore, from the eigenfunctions of the TB Hamiltonian, a new lattice is defined as

$$\boldsymbol{r}_i' = \frac{\sum_n |c_{i,n}| \boldsymbol{r}_n}{\sum_n |c_{i,n}|} \tag{107}$$

To simulate bulk, periodic boundary conditions are applied. Now for each site j the transition rate with its N_n neighboring sites is calculated via the modified Miller-Abrahams rate with the new lattice coordinates, the localization lengths, and eigen-energies from the TB model as input. Then a fraction of c of all N sites are randomly occupied by charges, whereas no double occupation is allowed to account for the large on-site Coulomb repulsion.

First, a hopping charge needs to be selected. Site j has the total rate to jump towards any of its neighbors $k_{tot}(s_j)$. Therefore, the probability that an occupied site j jumps is given by $p_j = k_{tot}(s_j) / \sum_{occupied\ j} k_{tot}(s_j)$, so the total rate of site j normalized by the sum of total rates of all occupied sites. Now a site j is chosen randomly according to their relative probabilities.

Next, a hopping event needs to be chosen. Similarly to the particle selection scheme, the probability that the charge at site j jumps to a neighboring (unoccupied) site i is given by $p_{ji} =$

$k_{ji}/k_{tot}(s_j)$. Again, the site i to which the charge jumps is determined randomly according to each sites' probability.

Lastly, the time Δt for the charge to hop, or equivalently how long the charge stayed at its location before jumping, needs to be calculated. Since the hopping times are Poisson distributed, we solve Equ. (106) for Δt

$$\Delta t = -\frac{\ln\left(P_{stayed}(s_j, \Delta t)\right)}{k_{tot}(s_j)} \equiv -\frac{\ln(Z)}{k_{tot}(s_j)} \tag{108}$$

To determine a hopping time from this, we chose a random number $Z \in (0,1]$ for this event and calculate Δt according to the equation above. With this procedure it is ensured that Δt follows the Poisson distribution of Equ. (106). This kMC step is repeated until a stopping criterium is fulfilled, in this case, when the calculated current density becomes stationary.

To calculate transport properties from the kMC simulation, the particle movements around the lattice, their hopping times and the energies of the visited sites are stored.

For our purposes, not the whole charge trajectories need to be stored, it is sufficient to store the effective charge movement. This means that starting from an effective movement of $\Delta \boldsymbol{x}_{eff} = 0$, for each jumping event of any charge going from a site i to site j with hopping distance vector $\Delta \mathbf{x}_{ij}$, the effective movement is updated $\Delta \boldsymbol{x}_{eff} \rightarrow \Delta \boldsymbol{x}_{eff} + \Delta \boldsymbol{x}_{ij}$. At the same time, the simulation time is updated $t \rightarrow t + \Delta t$. Storing every hopping event would be space demanding, since millions of hops are simulated. Therefore, one divides the simulation time interval $[t_{min}, t_{max}]$ of a minimum simulation time t_{min} to a maximum simulation time t_{max} into N_t time bins with logarithmic scaling. Now the effective movement $\Delta \boldsymbol{x}_{eff}$ and simulation time t is only stored once the end of a time bin is reached.

The energy of the hops is stored in a similar way. Starting from $E_{\boldsymbol{x}} = 0$, the average energy of each hop weighted by its hopping distance is added up in each cartesian direction x_i

$$dE_{x_i} = \sum_{hops} \frac{E_n + E_m}{2} \cdot (\Delta \boldsymbol{x}_{nm})_i \tag{109}$$

At the end of each time bin, the accumulated energies of the hops are normalized by the effective movement and stored

$$E_{x_i} = \frac{\sum_{hops} \frac{E_n + E_m}{2} \cdot (\Delta \boldsymbol{x}_{nm})_i}{\sum_{hops} (\Delta \boldsymbol{x}_{nm})_i} \tag{110}$$

Additionally, the DOOS is tracked as a histogram by adding a count to the corresponding energy bin of the current DOOS (denoted as $DOOS_i$) at each hopping event with final energy state E_j and removing a count in the corresponding energy bin of the initial site energy E_i. The $DOOS_i$ histogram for each hop is then weighted with the hopping time Δt and added up. At the end of each time bin, it is then normalized by the sum over all Δt since the beginning of the time bin.

$$DOOS(t_{bin}, E) = \frac{\sum_{hops=i} DOOS_i(E) \cdot \Delta t_i}{\sum_{hops=i} \Delta t_i} \tag{111}$$

From the section about DOS, it is known that the DOOS and the DOS are connected via the Fermi distribution $f(E, E_F, T)$ as $DOOS(E) = DOS(E) f(E, E_F, T)$. With this relation the Fermi energy (and the effective temperature T_{eff}, see later section) can be calculated by minimizing the following expression with the sum over least squares over the energy E

$$\log_{10}\left(\frac{DOS(E)}{1 + \exp\left(\frac{E - E_F}{k_B T_{eff}}\right)}\right) - \log_{10}\big(DOOS(E)\big) \tag{112}$$

Having obtained the tracked simulation time, effective movement, hopping energy, the Fermi energy and DOOS one can then calculate all charge transport properties of interest.

Conductivity

The first thing we are interested in is the *conductivity*. It is defined as $\sigma = en\mu$ with the elementary charge e, the charge density n and the *mobility* μ. The mobility is defined over the relation $v = \mu F$ with the drift velocity of the charges v and the electric field F or alternatively over the current density j via $\mu = j/enF$.

From the effective movement one defines in each direction x_i

$$\bar{J}_{x_i}(t) = \frac{e}{V}\Big(\Delta \boldsymbol{x}_{eff}(t)\Big)_i \tag{113}$$

with the simulation box volume V. For a time interval in which the current density converged, it is fitted a first order polynomial to $\bar{j}_{x_i}(t)$. The gradient of the first order polynomial is then the current density

$$j_{x_i} = \frac{e}{V} v_i \tag{114}$$

From there then the mobility and the conductivity is calculated in each direction

$$\mu_{x_i} = \frac{j_{x_i}}{enF_{x_i}} \quad \Rightarrow \quad \sigma_{x_i} = en\mu_{x_i} \tag{115}$$

Many analytical theories have been developed to model the mobility or conductivity of OSC, which differ in the level of detail, the charge carrier concentration, the DOS and others, but it is not in the scope of this thesis to discuss them here in detail. For completeness however, one example is given here anyways, namely the Mott-Martens model.

The Mott-Martens model[77,78] uses the concept of transport energy and also percolation theory. The conductivity is found by optimization of the hopping rate, and a percolation criterion is used to determine a critical hopping length at the transport energy that emerges from the optimization as the relevant energy for transport.

From Miller Abrahams, one assumes the conductivity to take the form

$$\sigma = \sigma_0 \exp\left(-\frac{2R^*}{\alpha} - \frac{E^* - E_F}{k_B T}\right) \tag{116}$$

The conduction is assumed to take place mostly by activation from the Fermi level to some yet to determine the energy E^* with some usual distance R^*. This distance now gets extracted from a percolation criterion

$$B_c = \int \mathrm{d}\boldsymbol{r} \int_{E_F}^{E^*} \mathrm{d}\epsilon \; g(\epsilon) = \frac{4\pi}{3} R^{*3} \int_{E_F}^{E^*} \mathrm{d}\epsilon \; g(\epsilon) \tag{117}$$

Now the conductivity is solely determined by E^* which is calculated by

$$\left.\frac{\mathrm{d}\sigma}{\mathrm{d}E^*}\right|_{E_{tr}} = 0 \tag{118}$$

From which follows

$$\sigma = \sigma_0 \exp\left(-\frac{2R^*(E_{tr})}{\alpha} + \frac{E_{tr} - E_F}{k_B T}\right) \tag{119}$$

The above expression is not a closed analytical form, it is implicitly formulated by the condition of Equ. (117), since depending on the DOS it cannot be written out analytically. Of special interest is also the temperature dependence of the conductivity (or mobility). For low to intermediate charge concentrations many models[77] predict the following form (for GDM)

$$\ln\left(\frac{\mu}{\mu_0}\right) \propto -\frac{1}{T^2} \tag{120}$$

One example is the often used relation $\mu \propto \exp\left(-c\left(\frac{\sigma_{DOS}}{k_B T}\right)^2\right)$ with a numerical prefactor $c \approx 0.69$ [79]. For high charge densities, the temperature dependence changes to the Arrhenius law

$$\ln\left(\frac{\mu}{\mu_0}\right) \propto -\frac{1}{T} \tag{121}$$

This result is to be considered with care since the models above might not be appropriate at high charge densities anymore. Comparing this to Mott's law, where $\ln\left(\frac{\mu}{\mu_0}\right) \propto -1/T^{1/4}$ this is a striking difference. This discrepancy is resulting from the different DOS underlying the models. Indeed, Mott's law is derived for a uniform DOS, whereas more appropriate models like the ones mentioned above consider the GDM, where the DOS is non-negligibly increasing towards higher energies from the Fermi energy, increasing the mobility due to an increase in available states by thermal activation into higher energies. If one applies a uniform DOS on the models above, indeed Mott's law is recovered.

Thermoelectrics

The next property of interest is the Seebeck coefficient. Before discussing how to extract that from the kMC simulation, the basic theory of thermoelectrics is introduced.

(Modified and extended version of text in my Master thesis[55] up to effective temperature section) If two different conducting materials are brought into contact forming an electric circuit, as in **Figure 10**, and there is a temperature difference between the contacts, a potential difference (voltage) between the contacts forms. This effect of the occurrence of a voltage upon providing a temperature difference between the contacts is called Seebeck effect.

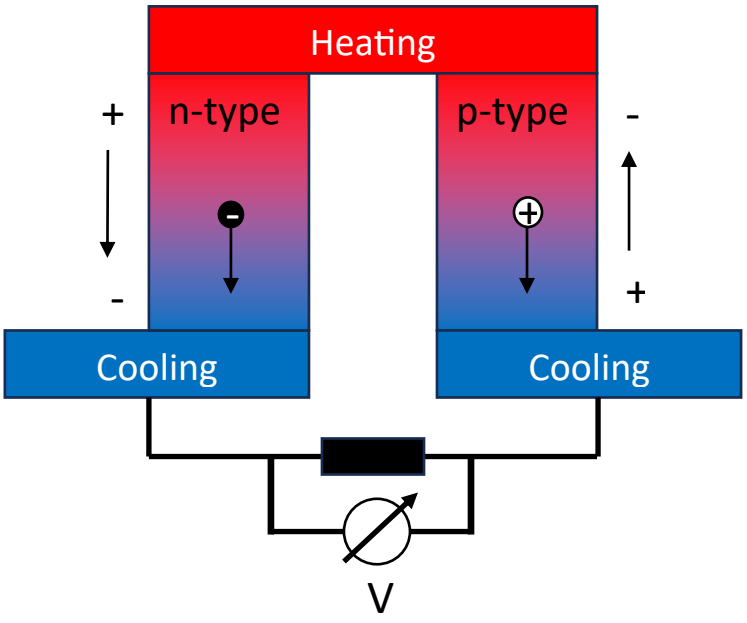

Figure 10 – Seebeck effect circuit.

The reverse effect, where a temperature difference forms upon applying a voltage, is called Peltier effect. The voltage drop in the Seebeck effect is proportional to the temperature difference, and the proportionality factor is a difference between material constants called Seebeck coefficients S. They are therefore defined as

$$S = \frac{V}{\Delta T} \tag{122}$$

with the voltage drop V. The Seebeck coefficient can also be derived by the solutions of the Boltzmann transport equation. There, the electrical current density $\boldsymbol{j}$ and the thermal current density $\boldsymbol{j}^q$ are phenomenologically connected by the equations

$$\boldsymbol{j} = L_{11}\epsilon + L_{12}(-\nabla T) \tag{123}$$

$$\boldsymbol{j}^q = L_{21}\epsilon + L_{22}(-\nabla T) \tag{124}$$

where $\epsilon = \boldsymbol{F} + \nabla\mu_F/e$ is the sum of the electric field $\boldsymbol{F}$ and the gradient of the chemical potential μ_F. These equations generalize the equations for electrical current, thermal current and diffusion laws, etc. where the individual currents are defined to be proportional to some scalar field gradient. Onsager found a useful reciprocal relation between the off-diagonal Boltzmann transport coefficients, $L_{21} = TL_{12}$. In the relaxation time approximation, the coefficients L_{ij} can be calculated from the Boltzmann transport equation as follows[80]

$$L_{11} = \mathcal{L}^{(0)} \tag{125}$$

$$L_{21} = TL_{12} = -\frac{1}{e}\mathcal{L}^{(1)} \tag{126}$$

$$L_{22} = \frac{1}{e^2 T}\mathcal{L}^{(2)} \tag{127}$$

where

$$\mathcal{L}^{(\alpha)} = \int \mathrm{d}E \left(-\frac{\partial f}{\partial E}\right)(E - E_F)^{\alpha}\sigma(E) \tag{128}$$

with the so-called conductivity distribution function

$$\sigma(E) = e^2\tau(E)\int \mathrm{d}\boldsymbol{k}\delta\big(E - E(\boldsymbol{k})\big)\boldsymbol{v}(\boldsymbol{k})^2 \tag{129}$$

Here, $\tau(E)$ is the relaxation time for a charge with energy E and f is the Fermi Dirac distribution as usual. The conductivity distribution function is not straightforwardly determined, it depends on the model details and on the used model. The conductivity and the Seebeck coefficient S (or reciprocally, the Peltier coefficient Π) are connected to the Boltzmann transport coefficients by

$$\sigma = L_{11} = \int_{-\infty}^{\infty} \mathrm{d}E\sigma(E)\left(-\frac{\partial f}{\partial E}\right) = \int_{-\infty}^{\infty} \mathrm{d}E\sigma'(E) \tag{130}$$

$$\begin{aligned} S = \frac{L_{12}}{L_{11}} = \frac{\Pi}{T} &= -\frac{1}{eT}\int_{-\infty}^{\infty} \mathrm{d}E(E - E_F)\frac{\sigma'(E)}{\sigma} \\ &= -\frac{1}{eT}\int_{-\infty}^{\infty} \mathrm{d}E(E - E_F)\frac{j(E)}{j} \end{aligned} \tag{131}$$

where in the last line was used $j(E) = \sigma(E)F$. The Seebeck coefficient is basically a sum over the transported energy per temperature weighted with the portion to which the energy contributes to charge transport.

By defining the *transport energy*

$$E_{tr} = \frac{\int_{-\infty}^{\infty} Ej(E)\mathrm{d}E}{j} \tag{132}$$

the Seebeck coefficient can be expressed as

$$S = -\frac{E_{tr} - E_F}{eT} \tag{133}$$

Equation (133) gives rise to the calculation of the Seebeck coefficient in the kMC simulation. In steady state, both the nominator and denominator are constant so we can integrate both to yield the equivalent expression of the transport energy

$$E_{tr} = \frac{\int_0^t \mathrm{d}\tau \int_{-\infty}^{\infty} Ej(E)\mathrm{d}E}{\int_0^t \mathrm{d}\tau \int_{-\infty}^{\infty} j(E)\mathrm{d}E} \tag{134}$$

The nominator is in discretized form equivalent to $\frac{e}{V} dE_{\boldsymbol{x}}$ from Equ. (109) and the denominator is equivalent to $\bar{J}_{\boldsymbol{x}}(t)$ from Equ. (113) and hence the transport energy equals the average hopping energy Equ. (110). Therefore, from kMC we can calculate the Seebeck coefficient in each cartesian direction x_i as

$$S_{x_i} = -\frac{1}{eT}\left(\frac{\frac{e}{V} dE_{x_i}}{\bar{J}_{x_i}} - E_F\right) = -\frac{1}{eT}\left(E_{x_i} - E_F\right) \tag{135}$$

If the Seebeck coefficients are plotted against the respective conductivities for different charge concentrations, sometimes a universal curve of the form

$$S = \frac{k_B}{e}\left(\frac{\sigma}{\sigma_0}\right)^{-1/4} \tag{136}$$

is observed, as first noticed by Glaudell et al.[81], i.e. the Seebeck coefficient decreases for increasing conductivity.

For thermoelectric applications often a figure of merit zT is defined to benchmark the performance of thermoelectric materials:

$$zT = \frac{\sigma S^2}{\kappa_{el} + \kappa_{lat}} T = \frac{PF}{\kappa_{el} + \kappa_{lat}} T \tag{137}$$

where κ_{el} is the electronic contribution of the thermal conductivity and κ_{lat} is the respective lattice contribution. PF is called the power factor. The maximum efficiency of a thermoelectric material is a function of the figure of merit and given by

$$\eta_{TE} = \frac{T_h - T_c}{T_h}\left(\frac{\sqrt{1+zT} - 1}{\sqrt{1+zT} + \frac{T_c}{T_h}}\right) \tag{138}$$

where T_c and T_h are the temperatures of the cold and hot sides respectively.

As last two points, the field dependence of the conductivity in OSCs and the concept of effective temperature will be discussed.

Field Dependence in Organic Semiconductors

(Following [82]) The Poole-Frenkel law was originally derived for inorganic semiconductors at high fields. For a charge in a localized Coulomb trap, the potential barrier is simply $e^2/4\pi\epsilon_r r$ with distance r from the trap center. If an electric field is applied, the potential on one side reduces by

$$\Delta U = eFr_0 + \frac{e^2}{4\pi\epsilon_r r_0} \tag{139}$$

where r_0 is the distance of the local maximum from the trap center. By setting the differentiation after r_0 to zero, one arrives at $r_0 = \sqrt{e/4\pi\epsilon_r F}$, resulting in

$$\Delta U = \sqrt{\frac{e^3 F}{\pi\epsilon_r}} \tag{140}$$

The probability of escaping the trap is then simply the Boltzmann factor $\exp(-\Delta U) = \exp\left(-\gamma\sqrt{F}\right)$ for some constant γ which then yields a field dependence of the conductivity

$$\sigma \propto \exp\left(-\gamma\sqrt{F}\right) \tag{141}$$

The Poole-Frenkel behavior is for organic semiconductors only found in a limited range at high fields, where the range was argued to be widened by consideration of a spatially correlated potential for charge carriers[83]. In fact, Pasveer's model can predict in a limited range for high fields a Poole-Frenkel behavior, since for rising fields the mobility saturates. In a larger field range, the field dependence of the logarithmic mobility on the field is rather as predicted quadratic or linear[84]. Pasveer developed a model describing the field dependence from low to intermediate field, optimized for low charge densities n by a mere empirical fit to numerical data

$$\mu(T, n, F) \approx \mu(T, n) f(T, F) \tag{142}$$

$$f(T, F) = \exp\left(0.44\left(\left(\frac{\sigma_{DOS}}{k_B T}\right)^{\frac{3}{2}} - 2.2\right)\left[\sqrt{1 + 0.8\left(\frac{Fea}{\sigma_{DOS}}\right)^2} - 1\right]\right) \tag{143}$$

The numerical data is found from cubic grid simulations with lattice constant a. For low fields, the logarithmic mobility is found to scale quadratically with the field, i.e. $\ln(\mu/\mu_0) \propto F^2$, up to some transition field strength $F \approx \sigma/ea$ after which it scales linearly, i.e. $\ln(\mu/\mu_0) \propto F$. Nenashev et al.[85] argued that Equation (143) cannot hold, since it misses a decisive factor, and showed by own simulations that the decisive length scale for the field dependence is not the lattice spacing a, but rather the localization length α, especially in the more realistic case of a random lattice and corrected upon that. More on that will be discussed in the section about effective temperature.

Effective Temperature

In 1992 S. Marianer and B.I. Shklovskii[86] investigated the effect of the electric field on the carrier energy distribution function in an amorphous semiconductor with localized states of localization length α via master equation approach. They found that at various temperatures and fields the carrier distribution function (which is the Fermi-Dirac distribution at zero field) is a Fermi-Dirac distribution with some effective temperature that is not the temperature itself at non-zero fields. They realized that strong electric fields, the electric field has a similar role to temperature. From a phenomenological point of view, this is very plausible, as illustrated in **Figure 11**.

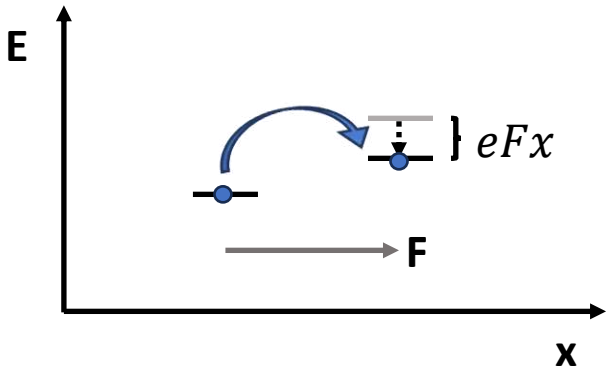

Figure 11 – Reduction of the energy barrier of a hop due to the electric field.

Considering two energy levels separated by a distance x and energy difference ΔE with an electric field F applied in direction of x. If a charge sitting on the energy site E_1 would hop to E_2, it would feel a voltage drop over the distance x, which effectively lowers the final hopping site by the energy eFx. This is equivalent to a charge being thermally activated from E_1 to a

site of some effective energy $E_2 - eFx$ such that it is plausible that the electric field plays a similar role as temperature. The charges gain energy from the electric field upon hopping, which causes the charge carriers to be effectively hotter than the lattice.

For example, at zero temperature, the Miller-Abrahams rate is given by $\nu = \nu_0 \exp(-2x/\alpha)$ which can be rewritten to be $\nu = \exp\left(-\frac{\epsilon}{k_B T_{eff}(F)}\right)$ with $\epsilon = eFx$ and $T_{eff} = eF\alpha/2k_B$. For non-zero temperatures, the situation is not so clear. If one would make the ansatz to combine field and temperature into an effective temperature as a simple sum, i.e. $T_{eff} = T + \gamma\, eF\alpha/k_B$, this would fail[67]: Supposing the dc conductivity σ_{dc} would only depend on $T_{eff}(T, F)$ given by the simple sum, the derivative of σ_{dc} with respect to the field should vanish in the Ohmic regime. However, calculating

$$\frac{\mathrm{d}\sigma_{dc}}{\mathrm{d}F} = \frac{\mathrm{d}\sigma_{dc}}{\mathrm{d}T_{eff}} \frac{\mathrm{d}T_{eff}}{\mathrm{d}F} = \frac{\mathrm{d}\sigma_{dc}}{\mathrm{d}T_{eff}} \frac{\gamma e\alpha}{k_B} \nrightarrow 0 \ (F \to 0) \tag{144}$$

such that a simple sum cannot be the right answer. Rather than a direct sum, one takes the phenomenological term

$$T_{eff} = \left(T^{\beta} + \left(\gamma \frac{eF\alpha}{k_B}\right)^{\beta}\right)^{1/\beta} \tag{145}$$

which gives $\beta = 1.54 \pm 0.2$ and $\gamma = 0.64 \pm 0.2$ depending on the transport parameters. Also often, this expression is just taken with $\beta = 2$. Unfortunately, there is no further analytical theory behind this expression that would derive this exact expression for the effective temperature. What has been proven though, for example in Ref.[85], is that the length parameter α in the effective temperature expression is indeed not the average lattice spacing, which is a function of the site density. Nenashev et al.[85] showed that by deriving a master equation including finite temperature and field, the solution of the equation, the carrier energy distribution function, cannot be a function of the site density and therefore the lattice spacing, concluding that the only relevant length to include in the effective temperature is indeed the localization length.

Another way to think of the effective temperature with a more physical motivated formula is by heating of the charge carrier distribution with applied field[87]. The heat flux towards the charge distribution due to Joule heating is given by

$$\dot{Q}_H = \sigma \cdot F^2 = qn\mu F^2 \tag{146}$$

with the conductivity σ and the mobility μ. On the other hand, the charge distribution cools down via heat exchange to the lattice. The heat flux to the lattice can be approximated by the time derivative of the Boltzmann energy

$$\dot{Q}_C = nk_B\dot{T}_{eff} \approx \frac{nk_B\left(T_{eff} - T_{latt}\right)}{\tau} \tag{147}$$

with the charge density n and relaxation time τ. Equating the two heat fluxes to obtain heat balance equation

$$\dot{Q}_H = q\mu F^2 = \frac{k_B\left(T_{eff} - T_{latt}\right)}{\tau} = \dot{Q}_C \tag{148}$$

From equating the diffusion coefficients from the Einstein-Smoluchowski relation with the average quadratic charge displacement ξ^2 and the classical Einstein relation for the heated charges one obtains

$$D = \frac{\xi^2}{6\tau} = \frac{k_B T_{eff}\mu}{k_B} \tag{149}$$

$$\Leftrightarrow$$

$$\frac{1}{\tau} = \frac{6k_B T_{eff}\mu}{\xi^2 q} \tag{150}$$

Inserting this into the heat balance and solving the quadratic equation for T_{eff}, one arrives at

$$T_{eff} = \frac{T_{latt} + \sqrt{T_{latt}^2 + \left(\gamma\frac{q\xi F}{k_B}\right)^2}}{2} \tag{151}$$

This expression is similar to the former one, but just slightly modified and will be further considered as effective temperature model 2, whereas the classical expression as model 1. In this case however, ξ is not directly the localization length as argued for the former expression. The details and validity range of the effective temperature remains an open question.

Nevertheless, the field dependence of the mobility has for a wide range of parameters like carrier concentration, temperature and field strength been verified[88] to be the low field

mobility with the temperature being exchanged for the effective temperature, which is remarkable.

Results

Power Factor Optimization for Anisotropic Localization Properties

This section summarizes the theoretical findings that were performed by me for the collaboration with Diego Rosas Villalva et al. in Ref.[46].

The experimental collaborators used Hansen Solubility Parameters (see introduction) to control the orientation of aggregates on thin films. Here for, they studied 2DPP-2CNTVT thin films doped with three different n-type dopants, namely TBAF, TAM and N-DMBI, each with different doping levels and different solvents. For those systems, they performed structural analyses to extract the crystallinity and orientation of the films using GIWAXS and AFM and performed in-plane measurements of the Seebeck coefficient and conductivity of the thin films. With the help of HSP and the Solubility sphere they could choose a proper solvent for the doped n-type 2DPP-2CNTVT:N-DMBI system to obtain a system with a high edge-on to face-on ratio (EFR). For this system they found an exceptionally high power factor and break the limitation of the conductivity dependence of the Seebeck coefficient $S \sim \sigma^{-1/4}$ that is usually universally observed for OSCs.

To understand the observed deviation of the N-DMBI doped polymer from the usually expected $S \sim \sigma^{-1/4}$ law we have to look at the implications of the data about crystallinity and polymer orientation on the electronic wave functions. Higher crystallinity should imply a higher delocalization of the charge carriers, especially along the $\pi - \pi$ stacking direction of the crystalline grains. That alone would simply increase the effective localization length in every direction if the crystalline regions were randomly orientated. This changes if one introduces a preferred orientation of the crystalline regions. For example, if one manages to increase the edge-on oriented portion of crystalline regions, the in-plane delocalization gets enhanced whereas the out-of-plane delocalization gets reduced. This is schematically shown in **Figure 12**.

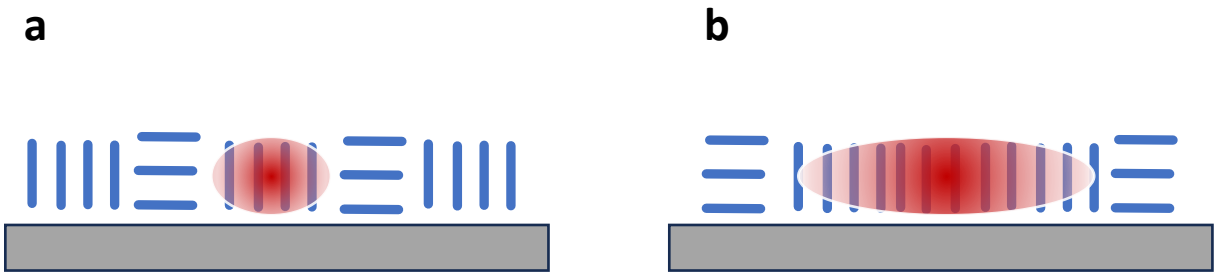

Figure 12 – a For $EFR \approx 1$ the wavefunction is spherical. **b** For $EFR \gg 1$ the wavefunction gets anisotropic.

Delocalization mostly takes place along the polymer backbone and in $\pi - \pi$-stacking direction, since lamellar stacking is not advantageous for delocalization due to the separating and usually not conductive side chains. Similar to the edge-on case, for face-on orientation the localization length would be enhanced in the out-of-plane direction and reduced in the in-plane directions. Effectively this implies that the introduction of a preferred orientation of crystalline regions introduces an anisotropy in the localization of electronic states, which means a non-spherical effective volume, in which the spatial electronic wavefunction is confined, which is represented as flattened spheres or ellipsoids in **Figure 12**. It is worth to note that in the edge-on orientated case the effective localization length gets enhanced in the whole plane of the substrate due to the in-plane randomly orientated crystalline grains, which is different from the situation after e.g. rubbing or tensile drawing, where one has a one specific direction of orientation.

We now use this conclusion about the anisotropy of the localization length to investigate the implications of an anisotropic localization length with regular kinetic Monte Carlo (kMC) simulations.

For that, we implement a regular lattice of box size 20^3 with periodic boundary conditions, inter-site-distance $a_{NN} = 1.8\,nm$ and gaussian energetic disorder with a disorder width of $\sigma_{DOS} = 75\,meV$. The charge transport is modelled as nearest neighbor Hopping (nnH) with Abraham-Miller hopping rates from site *i* to site *j*

$$p_{ij} = \nu_0 \times \begin{cases} \exp\left(-2\sqrt{\left(\frac{\Delta x}{\alpha_x}\right)^2 + \left(\frac{\Delta y}{\alpha_y}\right)^2 + \left(\frac{\Delta z}{\alpha_z}\right)^2}\right) \exp\left(-\frac{E_j - E_i}{k_B T}\right) & if\ E_j > E_i \\ \exp\left(-2\sqrt{\left(\frac{\Delta x}{\alpha_x}\right)^2 + \left(\frac{\Delta y}{\alpha_y}\right)^2 + \left(\frac{\Delta z}{\alpha_z}\right)^2}\right) & if\ E_j < E_i \end{cases} \quad (152)$$

The first exponential factor resembles the tunneling term where Δx_i is the hopping distance in x_i direction (x, y, z) and α_{x_i} is the corresponding localization length. The second exponential term for upwards-hops with site energies $E_j > E_i$ is just the Boltzmann factor for temperature *T*. Lastly, ν_0 is attempt-to-hop-frequency and chosen to be $\nu_0 = 10^{11}\ 1/s$ for every simulation.

For the simulation, five cases are considered. First, the case with an isotropic localization length vector of $\alpha_{iso} = (\alpha_x\ \alpha_y\ \alpha_z) = 0.5 \times (1\ 1\ 1)\ nm$ was simulated to compare the results to. Then, the edge-on and face-on cases were simulated by setting the respective localization length triplets to $\alpha_{eo} = 0.5 \times (2\ 2\ 1)\ nm$ and $\alpha_{fo} = 0.5 \times (1\ 1\ 2)\ nm$, where in-plane is set to be the x-y-plane of the system. Since these localization length triplets would lead to an increased effective localization length, another two simulations were performed where the length of the respective localization length vectors are normalized to the length of the isotropic case to decouple the effect of the anisotropy from effects that are due to increase of the total effective localization length. In this case, the localization length triplets were set to $\alpha_{eo,norm} = \alpha_{eo} \times \frac{|\alpha_{iso}|}{|\alpha_{eo}|} = \frac{1}{2\sqrt{3}}(2\ 2\ 1)\ nm$ in the edge-on case and $\alpha_{fo,norm} = \alpha_{fo} \times \frac{|\alpha_{iso}|}{|\alpha_{fo}|} = \frac{1}{2\sqrt{2}}(1\ 1\ 2)\ nm$ in the face-on case. Physically, the normalization means that in comparison to the isotropic case, the localization length still gets enhanced in the directions of anisotropy main axes but reduced in the other dimensions, e.g. in the edge-on case the localization length is enhanced in-plane and reduced out-of-plane.

For each case of localization lengths, the calculation was performed with a charge carrier concentration of $c_f = 1\%$ and $c_f = 10\%$. The results are summarized in **Figure 13**.

To further support the claim of the connection of anisotropic localization length and edge-on morphology, we incorporated a polymer morphology generating subprogram into our kMC model.

For the actual kMC with the generated morphology, it is assumed that the intra-chain transport along the backbone of a defect (twist, bend) free polymer is enhanced. This is accounted for

by a factor f_{ich} that reduces the inverse localization length α^{-1} as $\alpha^{-1'} = \alpha^{-1}/f_{ich}$. Inter-chain transport along the face-face (pi-stacking) direction is assumed to be enhanced with respect to the other directions. Here, a normalized change f_{α} in the (vectorial) inverse localization length for each monomer is used, which conserves the volume of the corresponding ellipsoid. That is, $\alpha^{-1'} = \alpha^{-1}/f_{\alpha}$ in the $\pm$-face direction and $\alpha^{-1'} = \alpha^{-1}/\sqrt{f_{\alpha}}$ in the other (edge) directions.

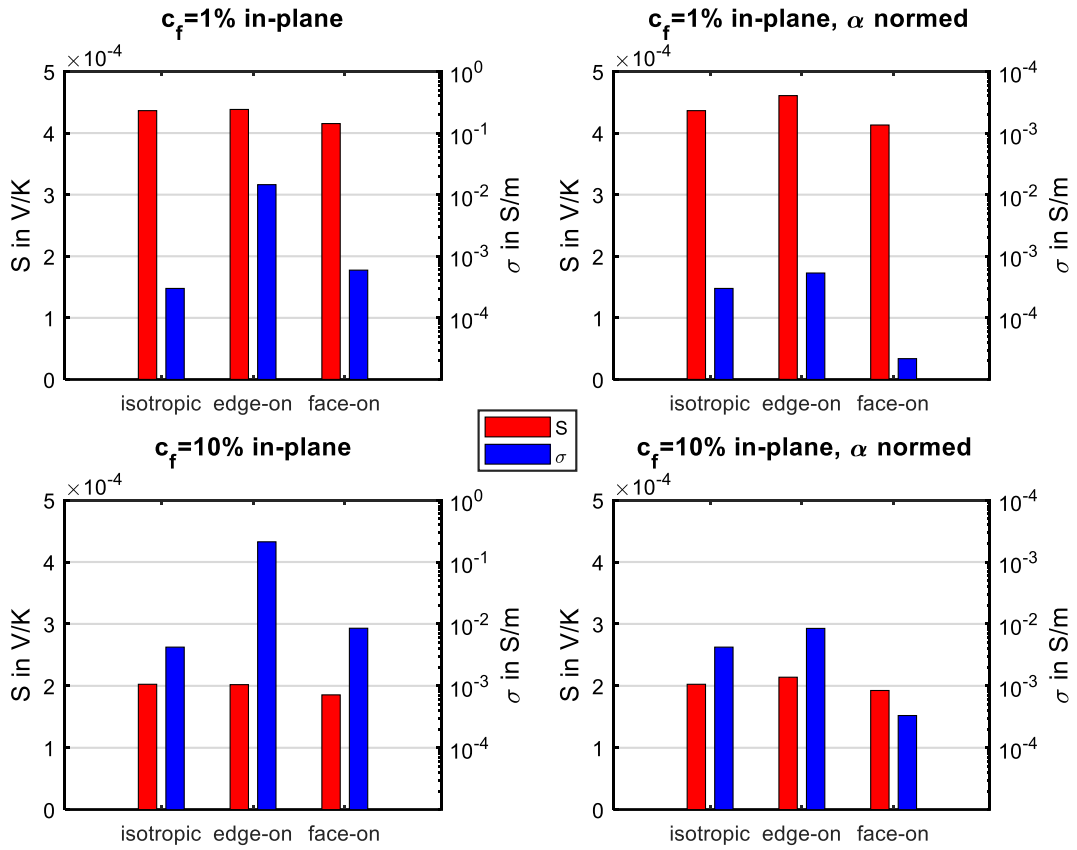

Figure 13 Comparison of the in-plane Seebeck coefficients and conductivities for free charge carrier concentrations of $c_f = 1\%$ and 10% for each isotropic, edge-on, face-on and their normed cases. Isotropic refers to a localization length vector of $\alpha_{iso} = 0.5 \times (1\ 1\ 1)\ nm$, edge-on refers to $\alpha_{eo} = 0.5 \times (2\ 2\ 1)\ nm$ and face-on to $\alpha_{fo} = 0.5 \times (1\ 1\ 2)\ nm$. Normed α refers to $\alpha_{eo,norm} = |\alpha_{iso}| \times \alpha_{eo}/|\alpha_{eo}|$ in the edge-on case and $\alpha_{fo,norm} = |\alpha_{iso}| \times \alpha_{fo}/|\alpha_{fo}|$ in the face-on case such that the effective localization length stays the same as in the isotropic case.

The upper two diagrams in **Figure 13** show the results for $c_f = 1\%$. The left one shows the un-normalized case. One can see that specifically in the edge-on case one has a significant increase in conductivity and a Seebeck coefficient that is barely affected. In the face-on case one also sees a slight increase in conductivity and a small drop in S. This is somewhat different to the right diagram, where the localization length is normalized. Here, for the edge-on case the conductivity is still increased, albeit not that much as in the un-normalized case, but also

the Seebeck coefficient is a little bit increased. In the face-on case the trend is different; here, the conductivity decreases significantly and the Seebeck coefficient is still a bit decreased in comparison to the isotropic case. The results of the $c_f = 10\%$ in the lower half of Figure 13 are qualitatively the same as for the $c_f = 1\%$ case.

The simulations therefore show that an anisotropy in the localization length, specifically the edge-on orientation, can induce a higher conductivity without the usually expected trade-off in the Seebeck coefficient. This results in an overall increase of the Power factor $PF = S^2\sigma$, as summarized in **Figure 14**.

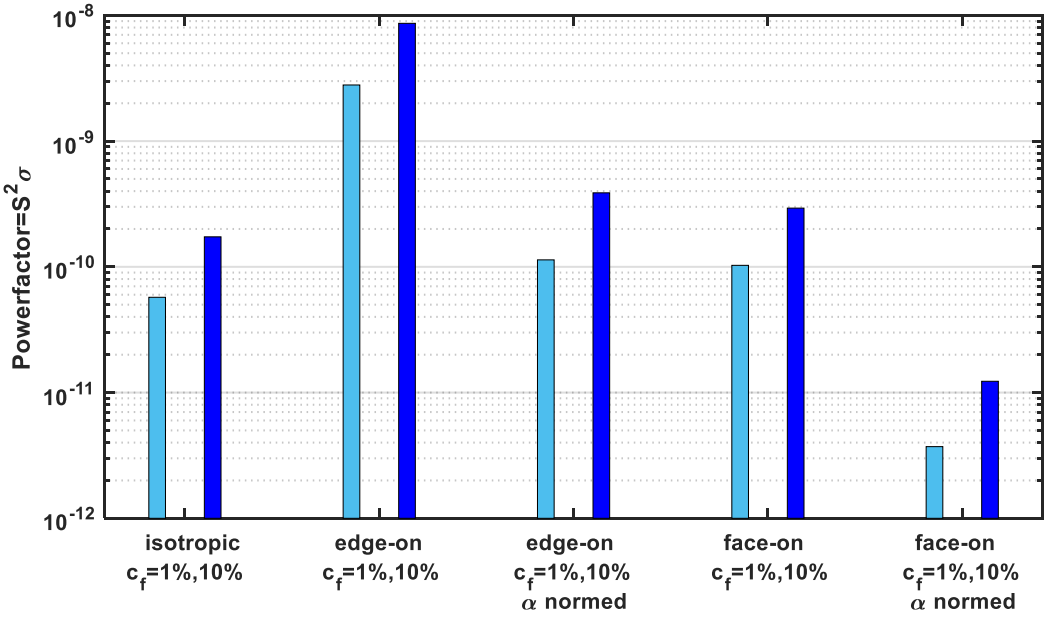

Figure 14 Comparison of the simulated Power factors for free charge carrier concentration of $c_f = 1\%$ (cyan bars) and 10% (blue bars) for each isotropic, edge-on, face-on and their normed cases. Isotropic refers to a localization length vector of $\alpha_{iso} = 0.5 \times (1\ 1\ 1)\ nm$, edge-on refers to $\alpha_{eo} = 0.5 \times (2\ 2\ 1)\ nm$ and face-on to $\alpha_{fo} = 0.5 \times (1\ 1\ 2)\ nm$. Normed α refers to $\alpha_{eo,norm} = |\alpha_{iso}| \times \alpha_{eo}/|\alpha_{eo}|$ in the edge-on case and $\alpha_{fo,norm} = |\alpha_{iso}| \times \alpha_{fo}/|\alpha_{fo}|$ in the face-on case such that the effective localization length stays the same as in the isotropic case.

Figure 14 also shows that the anisotropy with higher in-plane (edge-on) localization length with a larger effective localization length, i.e. not normalized localization length, is more effective than just the anisotropy. The practically important question is, whether normalized

or unnormalized localization lengths are more realistic from a physical point of view. On the one hand, the reorientation of randomly orientated crystalline grains into the edge-on orientation should in first order be closer to the normalized case. This is, because for the out-of-plane contributions of an inherently 3D percolation path, the possibility of high hopping rates due to $\pi - \pi$ orbital overlap along that direction gets reduced, which introduces a bottleneck that counteracts the positive effects of the improved average $\pi - \pi$ stacking along the in-plane direction. This resembles rather a redistribution or deformation of the localization volume. On the other hand, if a preferential orientation is accompanied by an overall increase in crystallinity, the total average delocalization can be expected to increase, which would correspond to a larger localization volume. The previous reasoning is additionally supported by the comparison of the results of the lattice kMC simulation with anisotropic localization length with the kMC simulation with a generated edge-on morphology.

Figure 15 shows an example morphology for the edge-on case for a just a few polymer chains for visual representation. The unitless inter-chain energies are given by (-4,3,-2,2) in the order face-face orientation, face-edge, edge-edge cross and parallel. The intra-chain energies are (0 2 2) for straight, twisted and bended direction. The color red means a monomer face orientation into x-direction, green is in y-direction and blue is in z-direction. To impose a certain preferred alignment orientation and direction, dummy homogeneous alignment fields into z direction were switched on during polymer growth. Positive energies always mean a penalty, whereas negative energies are energetically favorable. As can be seen, the given settings lead to a preferred edge-on orientation in-plane (x-y plane).

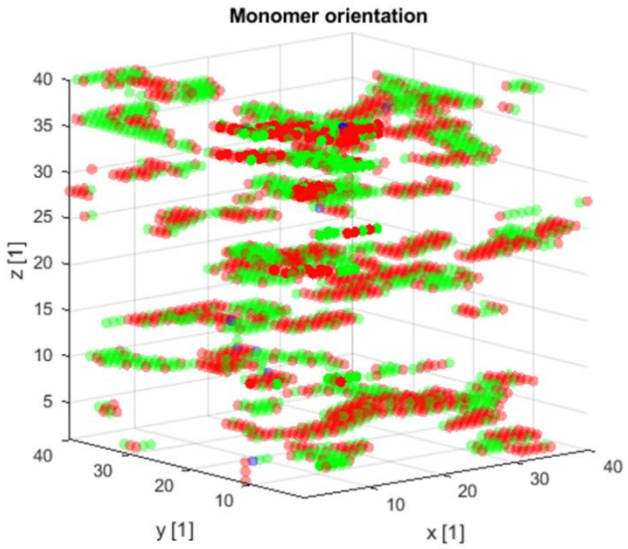

Figure 15 Visualization of a grown polymer morphology leading to edge- on orientated aggregates of polymer chains. Red means monomer-face orientation into x-direction, green into y-direction and blue into z-direction.

With the parameters given above, but much denser polymer morphology, kMC simulations with first no enhanced delocalization within a defect free chain segment (f_{ich}) and no delocalization enhancement for $\pi-\pi$ stacking (f_{α}) were performed, followed by simulations with $f_{ich}=1.5$ and/or $f_{ich}=1.25$. The results are summarized in the following **Table 1**.

Table 1 – In-plane Seebeck coefficient and conductivity for generated edge-on morphology for different combinations of delocalization enhancement factors of defect free chain segment f_{ich} and of $\pi-\pi$ stacking f_{α}.

	$f_{ich}, f_{\alpha}=1$	$f_{\alpha}=1.25$ $f_{ich}=1$	$f_{\alpha}=1$ $f_{ich}=1.5$	$f_{\alpha}=1.25$ $f_{ich}=1.5$
S $[\mu V/K]$	697 ± 4	704 ± 5	715 ± 3	734 ± 3
σ $[mS/m]$	14.7 ± 0.1	19.0 ± 0.1	22.7 ± 0.1	29.3 ± 0.3

Noting that physically indeed delocalization is enhanced for $\pi - \pi$ stacking and within a defect free chain segment ($f_\alpha, f_{ich} > 1$), these results confirm the previous results of the connection of an anisotropic localization length and edge-on morphology, leading both to an enhanced power factor in the in-plane direction.

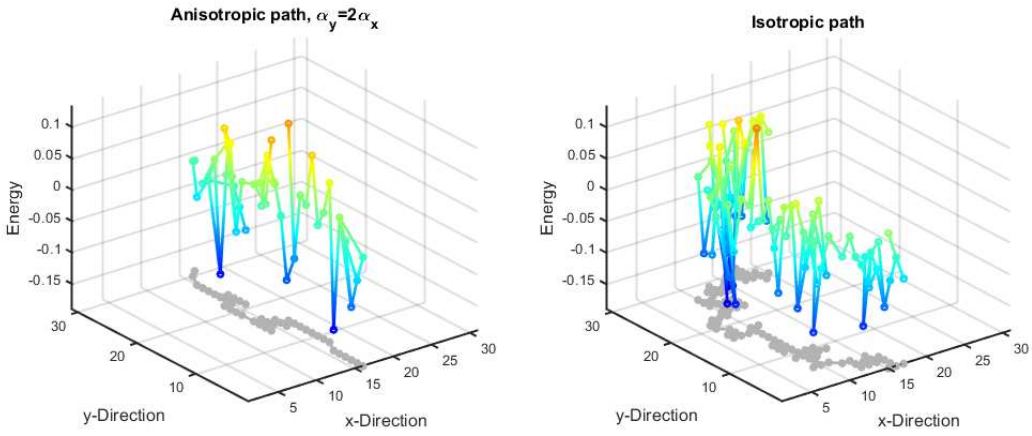

Figure 16 Difference between hopping paths of same system with for anisotropic (left) and isotropic localization (right), simulated by a 2D kMC model. Field is applied in y-direction. To highlight the energy of each site they are additionally color-coded with red colors indicating high energies and blue colors indicating lower energies. While in the isotropic case a larger path-network is explored, in the anisotropic case the path is more direct at the expense of occasionally higher energy barriers but therefore reduced tunneling action in y-direction, enhancing the transported energy on average.

To explain the simultaneous increase in σ and S, and concomitantly of the power factor in the edge-on orientation, it is instructive to visualize the hopping path of a charge in the anisotropic case in comparison to the isotropic case, which is done in **Figure 16**. Here, a 2D kMC simulation was performed to visualize the hopping path also in energy space. The localization length is set to be enhanced in the y-direction, where also the field is applied. It is directly visible that the hopping path in the anisotropic case is more linear and direct, whereas in the isotropic case the charge is exploring a more random path. This is, because for the same energy difference $E_j - E_i$ between two hopping sites *i* and *j*, the probability to hop into the direction of the larger localization length given by the tunneling term in the Miller-Abraham rate p_{ij} is higher. This also means that the charge can overcome a larger energy difference in the

direction of larger delocalization than in the direction of smaller delocalization for the same overall hopping rate, which translates into a higher transport energy for pathway that contain more hops in the easy direction. As such, the more direct path translates not only into a higher velocity in the direction of larger delocalization and therefore into a higher conductivity, but into a less optimized path from a pure energy perspective. This means that the trade-off for the geometrically more direct path are occasionally higher jumps in energy, which translate into a higher transport energy, which then in turn leads to a slightly increased Seebeck coefficient.

Field Dependence Simulations

For the Field Dependence of the conductivity of organic semiconductors several theoretical approaches have been proposed in the past decades (see Theoretical Background). The approaches reach from simple considerations leading to Poole-Frenkel behavior over rather empirical parametrizations like Pasveer's model up to the Effective Temperature approach, assuming the electrical field acts equivalent to a heating of the charge carrier distribution. Assuming the validity of the Effective Temperature approach, it would in principle be possible to extract a characteristic length-scale of the hopping conductivity in OSC interpreted as the localization length. Experimentally, this can be done by measuring the temperature dependence of the ohmic conductivity and the field dependence of the conductivity up to high fields to extract a localization length from an effective temperature $T_{eff}(F)$ obtained via the mapping $\sigma_{Ohm}\left(T_{eff}(F)\right) = \sigma(F,T)$, as proposed in literature[85,87]. The same experimental approach has been followed in our group. For three example systems, namely rrP3HT:F4TCNQ with 0.2 mg/ml and 0.8 mg/ml and SuperYellow:F4TCNQ with 5mg/ml sequential doping, the experimentally obtained field dependencies and effective temperatures are shown in **Figure 17** (M. Shokrani, unpublished data).

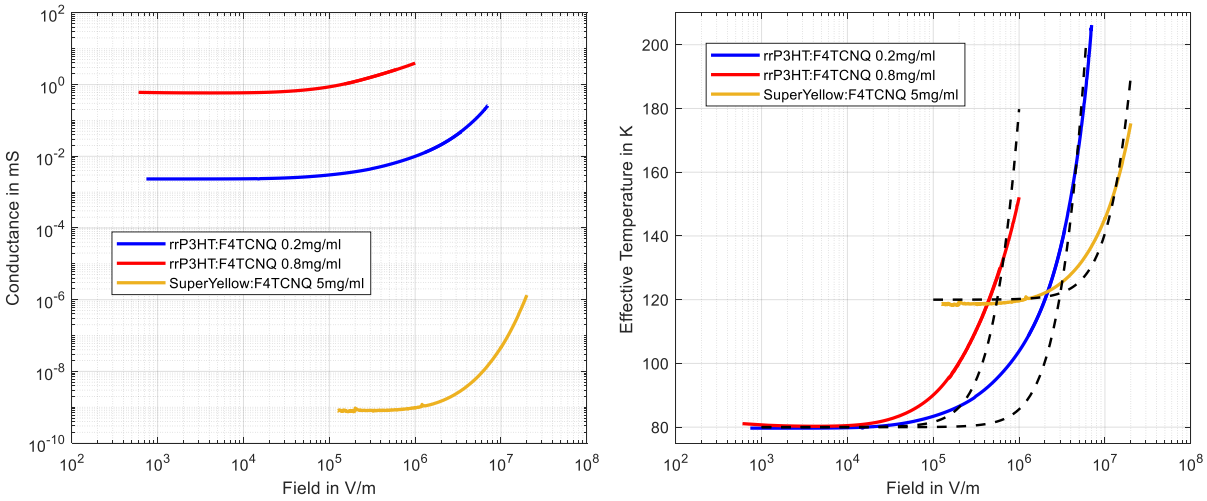

Figure 17 – Left: Experimentally obtained conductance as function of applied electrical field for two doping concentrations of the system P3HT:F4TCNQ and SuperYellow:F4TCNQ. Right: Experimentally obtained Effective Temperatures. The dotted lines are fits with the effective temperature model 1. (M. Shokrani, unpublished data)

While Super-Yellow only shows a significant field dependence at higher fields, the conductance of the P3HT systems show a significant field dependence already at relatively low fields. Analyzing the effective temperatures obtained experimentally via the approach described above, one finds that the characteristic length scales (interpreted as localization length) of the systems are in the order of $4\ nm$ for low doped P3HT and $22\ nm$ for higher doped P3HT or even two to three times larger values considering only the low field part. Besides the poor fit to the effective temperature model for the P3HT systems, these values are however much larger (about one to two order of magnitudes) than one would expect from disordered hopping systems, raising the question of the meaning of the obtained length scale. A possible working hypothesis could be that the length scale could represent the size of aggregates in the systems, as the doped P3HT is considered to be, leading to wavefunctions that could possibly be delocalized over those aggregates and hopping between aggregates takes place.

In this chapter the field dependence of the mobility or conductivity of different simple to aggregated morphologies is studied and compared to each other. First, the generation and parameters of each morphology are described, followed by the results from the tight binding model. Then the field dependence results are shown and discussed in the context of each morphological specifications, including other possible physical parameters that could influence the field dependence. The field dependencies are then analyzed with the effective

temperature approach to test the validity of the commonly used effective temperature models of the field dependence of OSC.

Field Dependence of the Simplified Model Morphologies

The first two morphologies studied are regular simple cubic (sc) lattices with box size of $20 \times 20 \times 20$ and lattice constant $a_{NN} = 0.5\,nm$. The orbital parameters for the ellipsoidal orbital approximation Equ. (72) are $(l_x, l_y, l_z) = (0.1, 0.1, 0.1)\,nm$, meaning a spherical s-type orbital. The transfer integral scaling factor was taken to be $\nu_0 = 10^{14}\frac{1}{s}$. Here, no ions are considered, so $V = 0$. The diagonal disorder for the first morphology was $\sigma_{dis} = 100\,meV$ and for the second $\sigma_{dis} = 80\,meV$. **Figure 18** shows the projection of a slice or tile of the center of mass lattice. The circles are the centers of masses of each localized eigenstate and their radius is proportional to their localization length. The colors indicate the eigen-energies of the states.

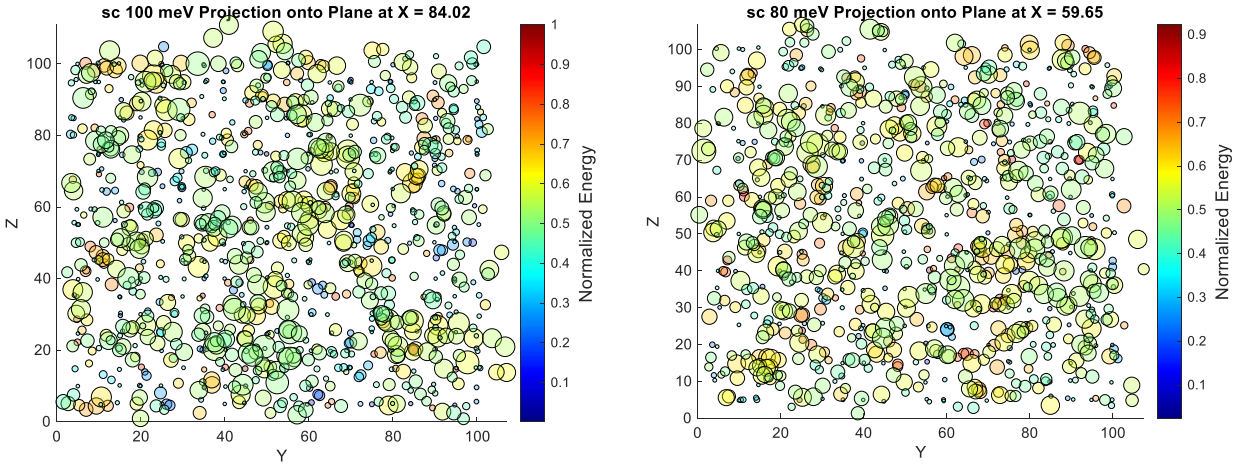

Figure 18 – Left: Projected slice of sc morphology with 100 meV disorder. Right: Projected slice of sc Morphology with 80 meV.

It is directly obvious from Figure 18 that the states are not distributed as a simple lattice anymore. This reflects the energetic and spatial correlations introduced by the random on-site energies through the tight binding model. The local energetic environment of the lattice and

the coupling through the transfer integral causes more or less localized states with eigenstates not being solely localized on one lattice site. Therefore, the center of mass of the eigenstates gets distorted from a simple lattice and reflect the energetic disorder of the system. One can hereby already observe some degree of clustering of eigenstates. This can be explained by the nature of randomness, which causes some degree of clustering since a uniform spatial distribution has lower entropy than a little bit clustering. This random clustering can even be enhanced through the interaction via the transfer integrals.

Figure 19 shows the DOS obtained from the TB calculations together with the localization length distribution for on-site disorders of 100 meV and 80 meV. The calculated DOS is fitted with a single gaussian (orange curve). The fitted disorders match the on-site disorder well with $\sigma_{DOS} = 83 \pm 3\, meV$ for sc lattice with 80 meV on-site energy disorder and $\sigma_{DOS} = 104 \pm 3\, meV$ for sc lattice with 100 meV on-site energy disorder. For the localization length distributions, each circle corresponds to the localization length α_i of eigenstate with eigenenergy E_i. The distributions follow a distribution that is similar to the DOS, but very scattered, meaning that for a given eigenenergy the localization length is not well defined but scattered around some mean value. The mean value of the localization length in a small energy interval is indicated as a continuous black line within the localization length distributions.

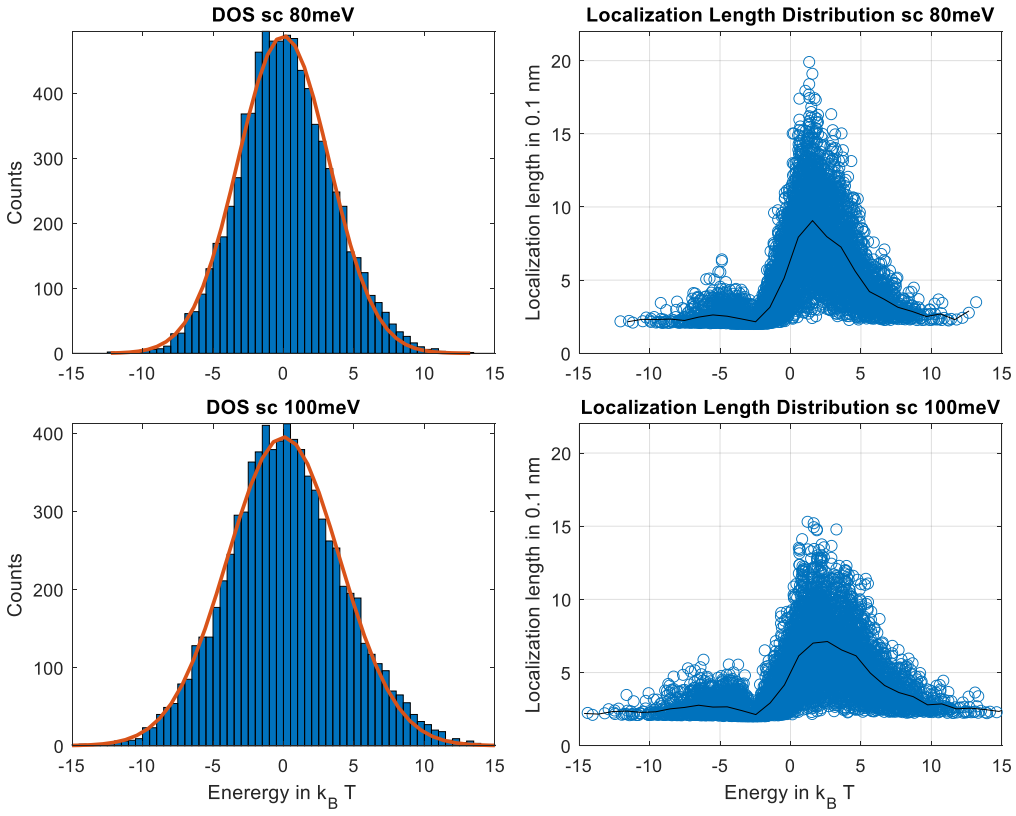

Figure 19 – Density of states and localization length distributions for simple lattice morphologies with 80 meV and 100 meV on-site energy disorder. The black line corresponds to the mean value of the localization length within a small interval around each energy.

The comparison of the localization length distributions reveals the expected behavior that higher DOS disorder causes a higher degree of localization, as can be seen by both the mean localization length curve and the peak of the distributions being both lower in the 100 meV case than in the 80meV case. The small dip at around $-2.5\,k_BT$ is probably a numerical artefact of using the numerically less stable generalized eigenvalue problem and the symmetric sc morphology, but should have a negligible influence on the further simulations.

Next, the morphology generated by the 3-phase-model is introduced. Here, again a $20 \times 20 \times 20$ box is used for the morphology generation, together with an inter-site distance of $a_{NN} = 0.5\,nm$. The aim is to obtain a morphology that is as aggregated as possible. Therefore, the following program parameters were chosen. First, long chains are considered by setting the number averaged number of repeat units per chain (In.pol_Mn) to 200, with a

weight ratio of 1 (In.pol_nr). At time $t = 0$, 10% of all chains are nucleated (In.pol_nCh0=-0.1). For growing the polymers, the energetic penalties/gains for intrachain conformation are chosen to be $(E_{straight}, E_{twist}, E_{bend}) = (0, 4, 1)$ so that twisting is penalized much with the aim of enhanced $\pi - \pi$ −stacking and bends are penalized a bit so that bending does not happen too often. The interchain conformation energies are chosen as $(E_{face-face}, E_{face-edge}, E_{edge-edge,\parallel}, E_{edge-edge,\perp}) = (-8, 8, -3, 0)$. Again, this is motivated by wanting to reward $\pi - \pi$ −stacking, penalizing face-edge orientation and rewarding lamellar stacking. The monomer faces should be aligned in z-direction by an alignment field of In.pol_F_al(1,1:3)=(0,0,2) and the monomer directions are set with an alignment field into the x and y-direction by In.pol_F_al(2:,1:3)=(2,2,0). The probability of the nucleation of new chains should be length-weighted and an over-filling factor of 7 was taken to avoid larger voids within the final morphology.

With these settings, two morphologies are generated. For the first morphology, the aggregated phase gets attributed on-site energies drawn from gaussian distribution with 80 meV disorder while the amorphous phase has 100 meV on-site energy disorder. The cutoff energy for being within an aggregate is set at the value 1/3 for the normalized interaction energy of the monomers in the morphology $\left(E_{grain} \leq \frac{1}{3}\right)$. The second morphology has 45 meV on-site energy disorder in the aggregated phase and 80 meV in the amorphous phase. The transfer integral scaling factor was chosen $\nu_0 = 10^{14}\frac{1}{s}$, with an intrachain factor of $f_{ich} = 1.3$ for couplings within a chain. The orbital parameters of the monomer sites are $(l_x, l_y, l_z) = (0.87, 0.87, 1.3) \cdot 0.1\, nm$ such that $l_x \cdot l_y \cdot l_z$ is the same as for the sc case. Since the morphology is lattice-based with constant lattice spacing but $\pi - \pi$ −stacking is usually enhanced by closer packing, this is mimicked here by enhancing the orbital length in the monomer face direction. Lastly, the Coulomb potential is set to zero again since no ions are considered here. **Figure 20** shows again a projected slab of the morphology. Inspired by the name of the program module “MakeSnake”, the two morphologies are from here on called MakeSnake 80meV/100meV (or MS 80/100) and MakeSnake 45meV/80meV (or MS 45/80). Here, in contrast to the sc morphologies, the background contains the direct morphology created by MakeSnake as squares and the colors represent the normalized interaction energy of each monomer/site, making the aggregated phases visible as more blueish.

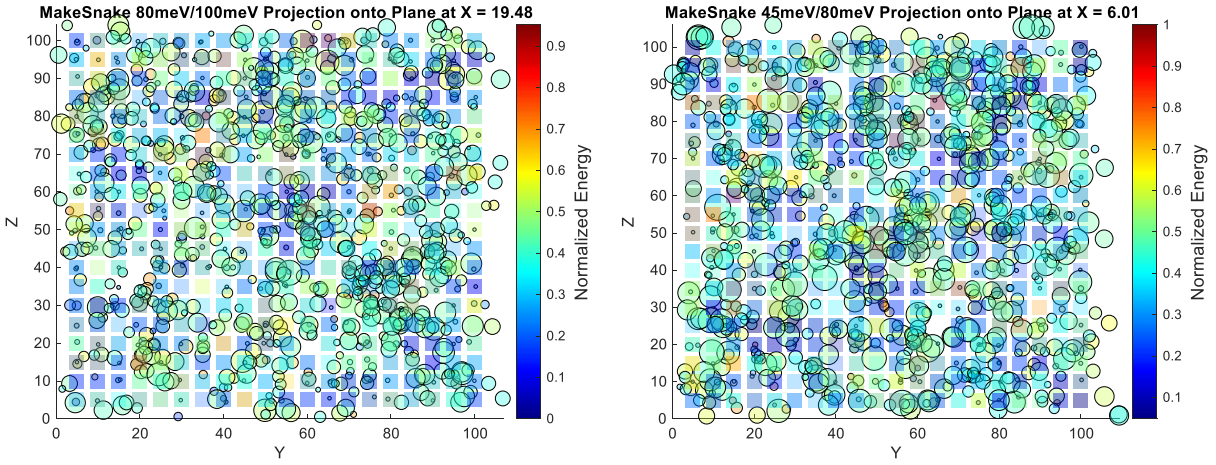

Figure 20 – Left: Projected slab of MakeSnake 80meV/100meV. Left: Projected slab of MakeSnake 45meV/80meV.

From Figure 20 one can see that the center of mass lattice approximately follows the aggregates of the MakeSnake morphologies. Within the aggregates, the state density is enhanced as well as the localization length, as one would expect. However, the achieved aggregation is not very large. The morphology rather consists out of smaller, but more interconnected aggregates.

To achieve larger aggregates, the subprogram for morphology generation via annealing is used. The fraction of guest (aggregated) sites was set to 0.4. The cohesive energy of both the host and guest being the evaporation enthalpy of the host or guest is set to $E_{coh} = 176 \frac{kJ}{mol}$. The ratio of the free energy of the host-guest interface with respect to the host-host interface is set to the factor 4. And finally, the annealing temperature is set to $T_{ann} = 4k_BT$. With these parameters the annealing process simulation is continued until either 10^5 steps are reached or the correlation radius of guest clusters (aggregates) reaches the value $15 \cdot a_{NN}$.

For the tight binding parameters, as in the previous cases, the transfer integral scaling factor was chosen $\nu_0 = 10^{14} \frac{1}{s}$ and the orbital parameters of the monomer sites are $(l_x, l_y, l_z) = (0.87, 0.87, 1.3) \cdot 0.1\, nm$ again. As no chain information is available, no additional factor is introduced. Again, no ions are considered, so $V = 0$. Two annealed morphologies are

considered, once with on-site energy disorder of 45 meV in the aggregates and 80 meV in the amorphous phase (denoted as Annealed 45meV/80meV) and relative positional disorder of the amorphous phase of $0.2 \cdot a_{NN}$, and secondly with 25 meV in the aggregated phase and 80 meV in the amorphous phase (denoted as Annealed 25meV/80meV) with no additional positional disorder of the amorphous phase. The results of the morphology are shown in **Figure 21**.

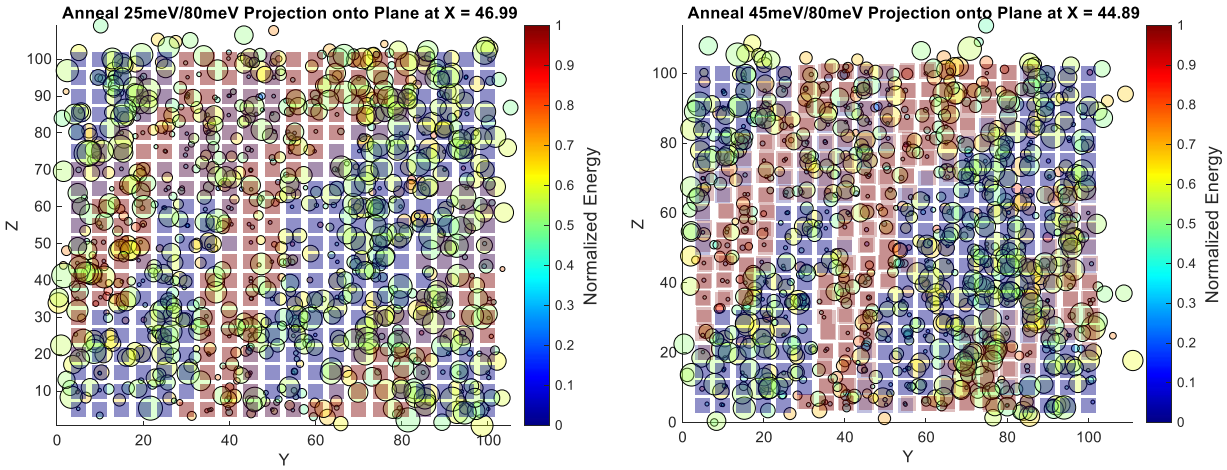

Figure 21 – Left: Projection of slab of Annealed 25meV/80meV morphology. Right: Projection of slab of Annealed 45meV/80meV morphology.

The background squares again show the generated morphology with blue being aggregates and red being the amorphous phase. The aggregates are clearly larger here, but also separated by larger regions of amorphous phases. At the same time (not seen in the projection) there may be direct contact areas between different aggregates because of their size here. As in the MakeSnake morphologies, the state density and the localization length in the aggregated phase is again larger than in the amorphous phase, as to be expected.

The results for the DOS and localization length distributions for both MakeSnake and Annealed morphologies are summarized in **Figure 22**. The DOS was fitted with a double gaussian

$$DOS(E) = A_1 \exp\left(-\frac{(E-\mu_1)^2}{2\sigma_1^2}\right) + A_2 \exp\left(-\frac{(E-\mu_2)^2}{2\sigma_2}\right) \tag{153}$$

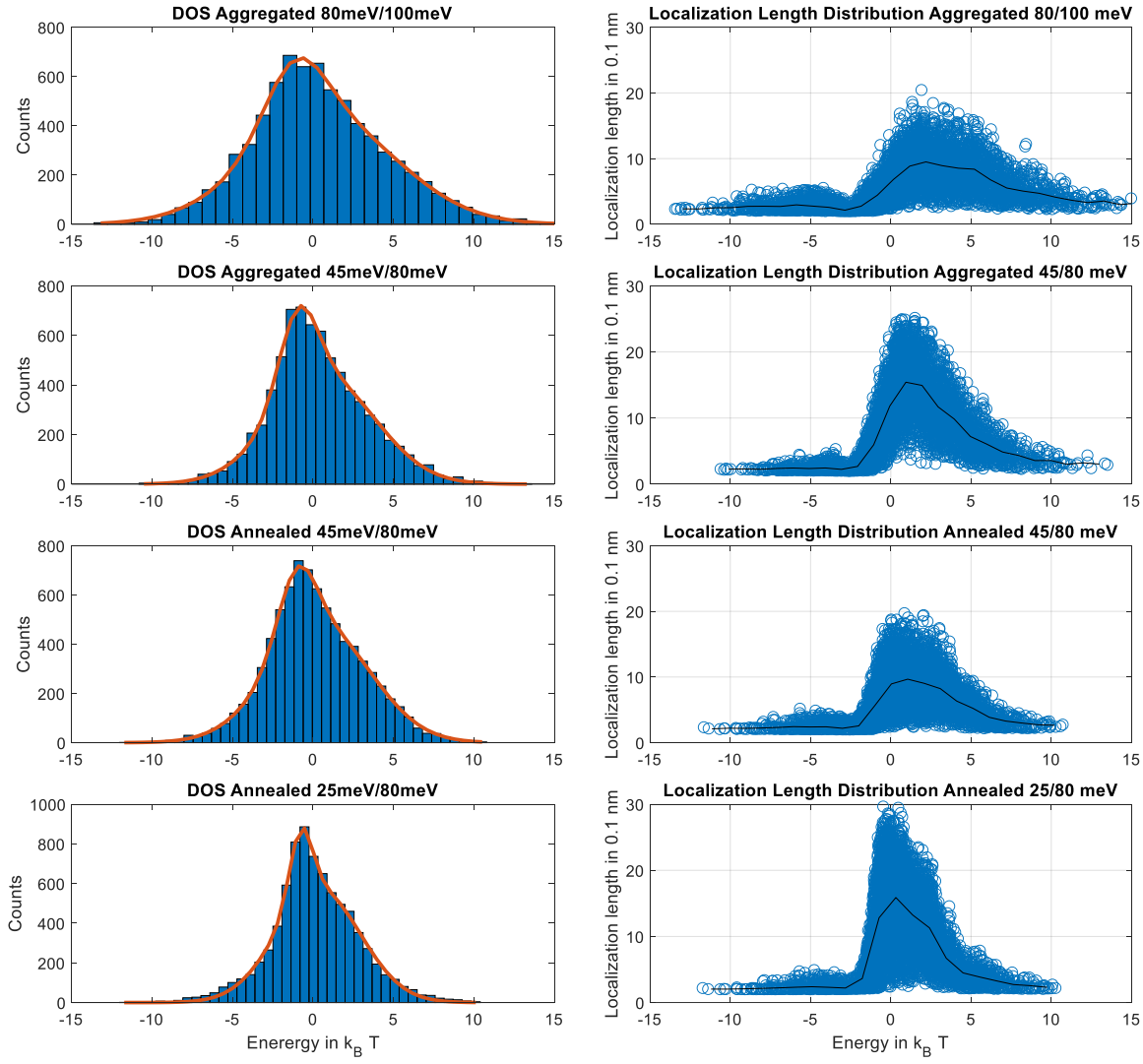

Figure 22 – Left column: DOS of Aggregated (MakeSnake) and Annealed morphologies. Orange lines are double gaussian fits. Right columns: Corresponding localization length distributions. The black line is the average curve.

Table 2 – Double gaussian fit parameters for different morphologies ($T = 300\ K$).

Morphology	A_1	μ_1/k_BT	σ_1/k_BT	A_2	μ_2/k_BT	σ_2/k_BT
MakeSnake 80meV/100meV	275 ± 40	-1.1 ± 0.2	1.9 ± 0.2	425 ± 40	0.7 ± 0.2	4.6 ± 0.2
MakeSnake 45meV/80meV	336 ± 40	-0.9 ± 0.1	1.2 ± 0.2	427 ± 30	0.7 ± 0.2	$3.2 \pm 0,2$
Annealed 45meV/80meV	290 ± 30	-1 ± 0.1	1.2 ± 0.2	468 ± 20	0.4 ± 0.1	3.2 ± 0.2
Annealed 25meV/80meV	358 ± 30	-0.7 ± 0.1	0.7 ± 0.1	570 ± 30	0.3 ± 0.1	2.6 ± 0.1

All DOS fit very well to double gaussians which are shifted in energy. The gaussians with the smaller disorders correspond to the more ordered aggregated phases, which are therefore also lower in energy than the amorphous phase which is the gaussian part with the larger disorder respectively. The disorders of the amorphous and aggregated phases approximately match the on-site energy disorders from the tight binding model input. However, the shift of the obtained means of the aggregated and amorphous phase has only a value of about 25-50 meV while experiments show higher values of 0.2-0.3 eV[89,90]. This is probably explained by the too simple modeling of the aggregated morphologies. As outlined before, it was tried to model the difference between aggregated and amorphous phase by enhancing the orbital parameter l_z in π −stacking direction to compensate the effect of closer packing in the aggregated phase. However, this has also an effect on the transfer integral of the amorphous phase, which is not desired. The shift of the means would be higher if the transfer integral would be solely enhanced in the aggregated phase. Additionally, including positional disorder in the amorphous phase could also enhance the shift, what can also be seen from the Annealed morphologies, from which Annealed 45meV/80meV has some positional disorder and Annealed 25meV/80meV not, while former has a larger shift than latter.

The MakeSnake 80meV/100meV has expectedly the lowest localization length compared to the other morphologies. The peak localization lengths are similar to the ones of the sc 80meV morphology, as one would expect from the aggregated phase. However, the width matches more the sc 100 meV distribution which comes from the amorphous phase.

From the almost identical DOS of MakeSnake 45meV/80meV and Annealed 45meV/80meV one might expect a very similar localization length distribution. However, the peak localization lengths of MakeSnake 45meV/80meV exceed the ones of Annealed 45meV/80meV significantly. This has three reasons: First, MakeSnake contains chain information, for which an intra-chain factor for the transfer integrals was introduced, enhancing the electronic coupling and therefore the localization length. Secondly, in Annealed 45meV/80meV, an additional source of (spatial) disorder in the amorphous phase was introduced, which will have a negative effect on the localization length. And lastly, the better interconnectivity of the smaller aggregates in the MakeSnake morphologies could enhance the localization length further compared to the Annealed one.

However, the localization lengths of the Annealed 25meV/80meV morphology are still expectedly the highest, since the aggregated phase has a very small disorder in the order of the thermal energy and no positional disorder in the amorphous phase is present.

With all these morphologies then kMC simulations as described in the theoretical background and methods section were performed for different electric fields applied in the z-direction. The attempt-to-hop frequency for all morphologies was set to $f_0 = 10^{14}\,\frac{1}{s}$ and the temperature was room temperature $T = 300K$. All field simulations were performed at a low free charge carrier concentration of $c_f = 0.5\%$. The results of the field-dependence of the conductivity are shown in **Figure 23**.

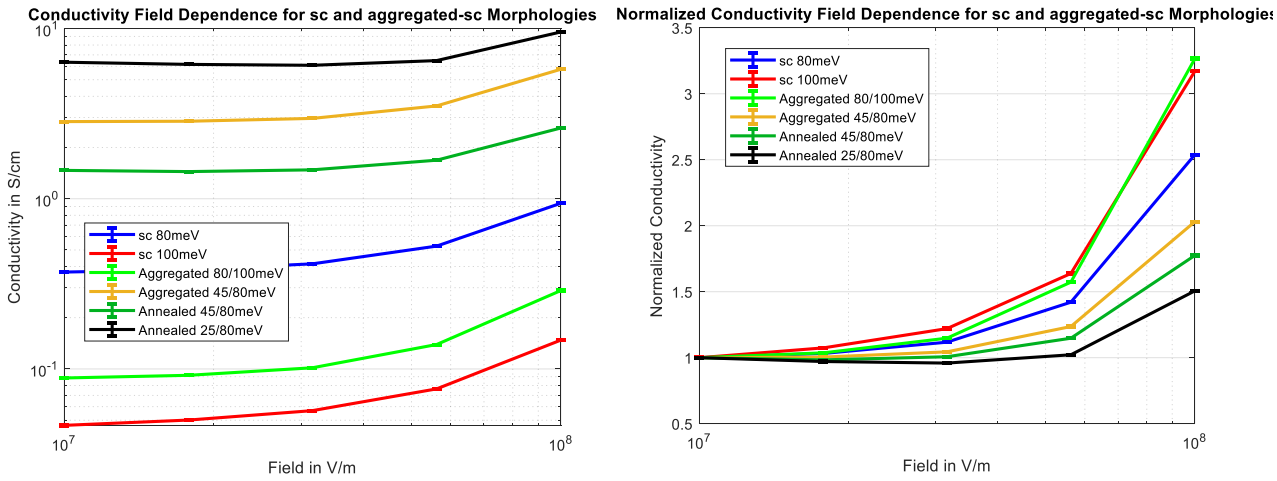

Figure 23 – Left: Field dependence of conductivity for different morphologies. Right: Field dependence of conductivity normalized to the value at lowest field.

The order of the morphologies in absolute value of the conductivity is easy to explain. The higher the (effective) disorder, the lower the conductivity. Also, the lower the mean localization length, the lower the conductivity. Latter explains why Annealed 45meV/80meV has a lower conductivity than MakeSnake 45meV/80meV albeit having almost the same DOS, since MakeSnake 45meV/80meV has the higher localization length due to the reasons explained above

However, looking at the field dependence, i.e. the slope of the conductivity curves, or by which factor the conductivity gets enhanced at the highest field compared to the lowest field simulated, the situation gets more complicated in detail. A coarse rule seen from the right plot in Figure 23 is basically the opposite trend of the order of the absolute values of conductivities. This means, the higher the effective disorder, the stronger the field dependence. However, this rule alone would not explain why MakeSnake 80meV/100meV morphology has basically the same field dependence as sc 100meV and why MakeSnake 45meV/80meV has a stronger field dependence than Annealed 45meV/80meV. This could be explained by the concept of the effective temperature. Here, a higher localization length leads to a higher field dependence. MakeSnake 80meV/100meV has a mean localization length of 0.56 nm, while sc 100 meV has a mean localization length of 0.43 nm. This difference could already suffice to enhance the field dependence of MakeSnake 80meV/100meV to compensate the effect of the lower field

dependence that the aggregates with lower disorder would imply. Hereby should also be noted that MakeSnake 80meV/100meV has even a higher mean localization length than sc 80meV. This is probably, again, due to the facts that MakeSnake has an intrachain enhancement factor not present in the sc morphologies and that the MakeSnake morphology has interconnected aggregates. The DOS fit to the DOS of MakeSnake 80meV/100meV also gives a gaussian part attributed to the aggregate of only about 50 meV disorder, enhancing the effect of delocalization in the aggregates compared to the sc 80meV case. The higher mean localization length of the MakeSnake 45meV/80meV (0.86 nm) compared to the Annealed 45meV/80meV (0.61 nm) could then also be the reason why former has a higher field dependence than the latter, despite the very similar DOS.

From here, one could ask the question, what parameter has the larger influence on the field dependence. The general trend derived from the first rule about the disorder seems to suggest here that the disorder has a higher impact on the field dependence than slight changes in the localization length.

This result should now be compared to the predictions of the classical effective temperature models. For example, Baranovskii used the temperature dependence from the GDM model

$$\sigma(T) \propto \exp\left(-c\left(\frac{\sigma_{DOS}}{k_B T}\right)^2\right) \tag{154}$$

together with the effective temperature T_{eff} instead of temperature T, in the following named Bässler's model. To be numerically consistent, also the actual temperature dependencies of each morphology are simulated and fitted to the expression $\ln(\sigma/\sigma_0) \propto -1/T^{\beta}$ (**Figure 25**), followed by substituting the temperature by the effective temperature. These two models will now be fitted to the numerically obtained field dependencies. From these fits, the localization length will be extracted as fit parameter. Also, the localization length from the direct fit of the effective temperature models to the effective temperatures from the simulations obtained from the DOOS are extracted and compared. The visual results are shown in **Figure 24** together with the obtained fit parameters in **Tables 3** and **4**.

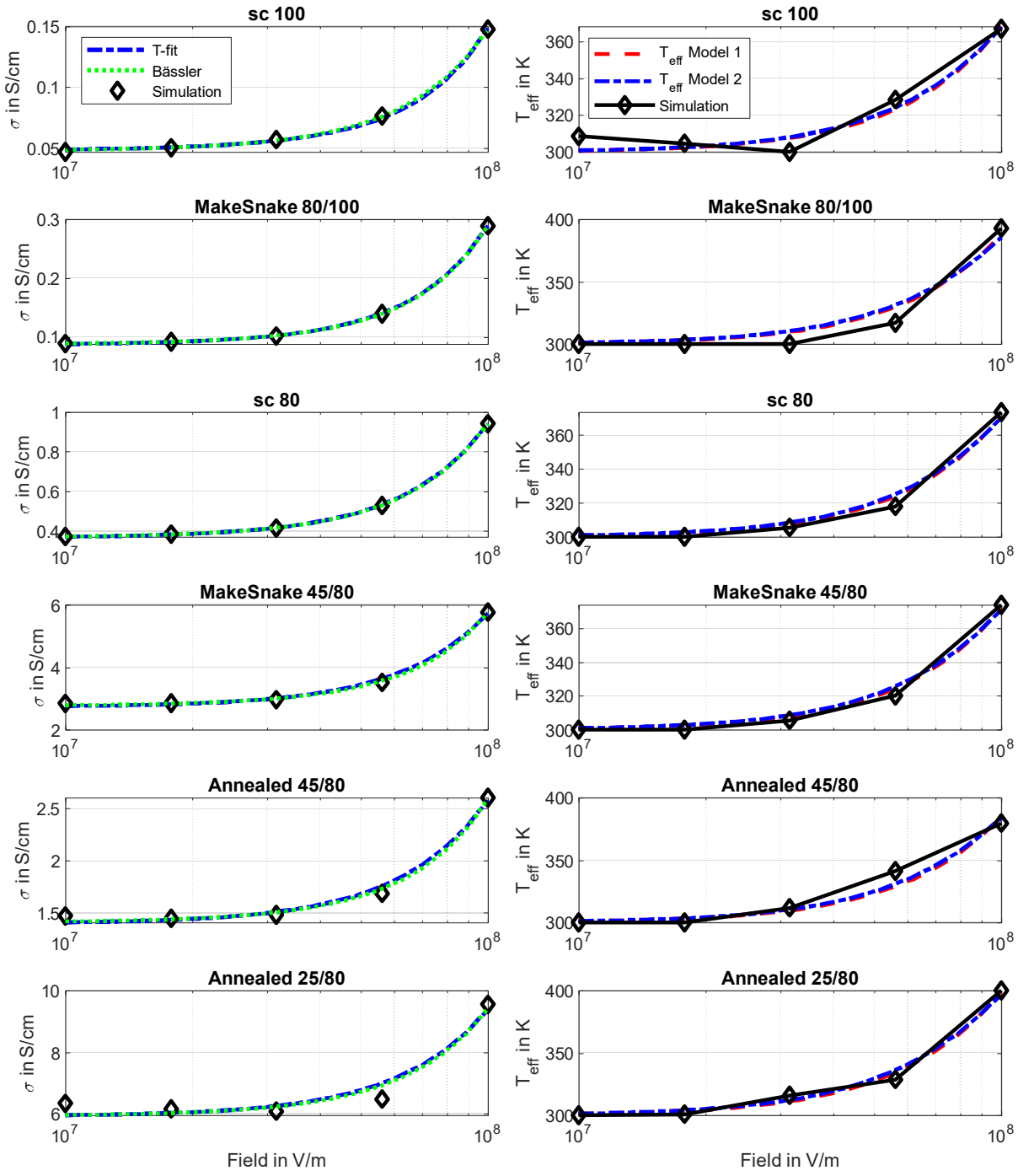

Figure 24 – Left: Fits to the field dependence of the different morphologies with the two different conductivity models. Fits were performed with effective temperature model 2. Right: Fits to the effective temperature obtained from fitting the DOOS using both effective temperature models.

Table 3 – Localization lengths from fits of $\sigma\left(T_{eff}(F)\right)$ to the simulated data for different morphologies (Figure 24, left). The last column gives the mean localization length from the $\alpha(E)$ distributions obtained from the tight binding calculations for comparison. $T_{eff}^{(2)}$ is the effective temperature model two respectively.

Morphology	Model	α from $\sigma\left(T_{eff}^{(2)}\right)$	α_{mean}
sc 100	Bässler	0.43 nm, C=0.23	
sc 100	$\sigma(T)$ Fit	0.40 nm	0.43 nm
MS 80/100	Bässler	0.35 nm, C=0.3	
MS 80/100	$\sigma(T)$ Fit	0.42 nm	0.56 nm
sc 80	Bässler	0.33 nm, C=0.42	
sc 80	$\sigma(T)$ Fit	0.41 nm	0.52 nm
MS 45/80	Bässler	0.22 nm, C=0.88	
MS 45/80	$\sigma(T)$ Fit	0.35 nm	0.86 nm
AN 45/80	Bässler	0.2 nm, C=0.85	
AN 45/80	$\sigma(T)$ Fit	0.31 nm	0.61 nm
AN 25/80	Bässler	0.17 nm, C=1.24	
AN 25/80	$\sigma(T)$ Fit	0.26 nm	0.94 nm

Table 4 – Localization length from fits of the effective temperature models 1 and 2 onto the effective temperatures obtained directly from the simulations (Figure 24, right). Mean localization length, localization length at transport energy and Fermi level from the localization length distributions from tight binding calculations for comparison in the last columns. Errors for fitting approximately $\Delta\alpha \approx 0.05\ nm$.

Morphology	α from $T_{eff}^{(1)}$	α from $T_{eff}^{(2)}$	α_{mean}	$\alpha(E_{tr})$	$\alpha(E_F)$
sc 100	0.3 nm	0.43 nm	0.43 nm	0.3 nm	0.25 nm
MS 80/100	0.33 nm	0.5 nm	0.56 nm	0.5 nm	0.25 nm
sc 80	0.3 nm	0.44 nm	0.52 nm	0.3 nm	0.25 nm
MS 45/80	0.3 nm	0.45 nm	0.86 nm	1.1 nm	0.25 nm
AN 45/80	0.33 nm	0.49 nm	0.61 nm	0.9 nm	0.25 nm
AN 25/80	0.36 nm	0.54 nm	0.94 nm	1.5 nm	0.25 nm

From **Figure 24** (right) one sees decent fits to the effective temperature data despite the partially noisy T_{eff} data from the simulations, which come from fitting the temperature and the Fermi energy in the DOOS at the same time, both being slightly correlated via the temperature dependence of the Fermi energy. The localization lengths extracted from the fits of the models to the data are shown and compared to the mean localization length in **Table 4**. The values of the second effective temperature model are more consistent in their trend and closer to the input value than the first model. Thereby, focusing on the second model, the localization lengths follow approximately the same trend as the mean localization lengths from the input. The high value of α of MakeSnake 80meV/100meV in comparison to the other morphologies for example can probably been explained by a fitting error overestimating the effective temperature data point at highest field, which also causes a dip down of the Fermi energy (**Figure 27**). Considering fitting errors, the trend is consistent. However, with decreasing effective energetic disorder, the relative deviations to the mean localization length increase significantly and cannot be explained by just the fitting error. One possible reason is that not the mean localization length is the effective localization length (if such one is even defined in this framework) but something like the mean localization length between Fermi energy and transport energy. Another possible reason is that the numerical γ −factor in the formula for the effective temperature is taken the same for every morphology ($\gamma = 0.63$), but might actually be different for each morphology. It is however not possible to elaborate this further with these simulations.

In **Figure 24** (left) one can also see good fits of both conductivity models. Both fits were performed with effective temperature model 2. The reason for the good fits for both models is the small effective temperature range of maximum 100 K and the similar functional form of the fit-functions $\ln\left(\frac{\mu}{\mu_0}\right) \propto -1/T^{\beta}$. Deviations can only be better distinguished for a larger effective temperature range.

Nevertheless, the extracted localization lengths from both fits to the $\sigma(F)$ data give a consistent trend. Expectedly, larger field dependencies of the conductivity give rise to larger fitted localization lengths, contrary to the actual localization lengths from the kMC input obtained from the tight binding calculations, which actually show the opposite trend. This is ultimately because by construction the models $\sigma\left(T_{eff}(F)\right)$ for the field dependence of the mobility or conductivity attribute the strength of the field dependence solely to the localization

length. This is in strong contrast to the simulation results, which suggest that the disorder and/or other factors like the morphology play a dominant role for the field dependence. Therefore, all effects of the energetic disorder, morphology and other possible contributions to the field dependence get reflected in the localization length. In Bässler's model, the energetic disorder is considered as $\sigma_{DOS}/k_B T_{eff}$ in the exponential function. The derivative of Equ. (154) with respect to the field, reflecting the field dependence gives a term $\sigma_{DOS}^2 \exp\left(-c\left(\frac{\sigma_{DOS}}{k_B T_{eff}}\right)^2\right)$, from which one would expect a decreasing field dependence with higher disorder. However, the kMC simulations performed here, and also in literature like in Ref.[91] implicitly show higher field dependence with increasing disorder. It seems that the temperature dependence models derived for vanishing field are not applicable directly just by substituting the temperature by the effective temperature, albeit always finding fit parameters that are able to describe the data. Also, the empirical model of Pasveer predicts a higher field dependence for higher disorder[84]. One can therefore conclude that the role of disorder and factors like morphology in the effective temperature model of the field dependence of conductivity is very much underestimated and not properly included.

One can also abstract the idea of the field dependence being determined by a field-dependent effective temperature away from certain functional forms through a determination of the effective temperature by the following 'experimental' procedure[87]. At a certain temperature T_0 the field dependence of the conductivity is measured (or here simulated). Then the ohmic conductivity is measured/simulated over a wide temperature range containing T_0. The effective temperature can then be determined by $\sigma(F, T_0) = \sigma\left(F \approx 0, T_{eff}(F)\right)$. If the field dependence is solely determined by the effective temperature in a functional form like the two effective temperature models, the localization length obtained from the corresponding fit of the effective temperature should give the same or similar localization length as the input localization lengths. The results for the temperature dependence of the ohmic conductivities are shown in **Figure 25**.

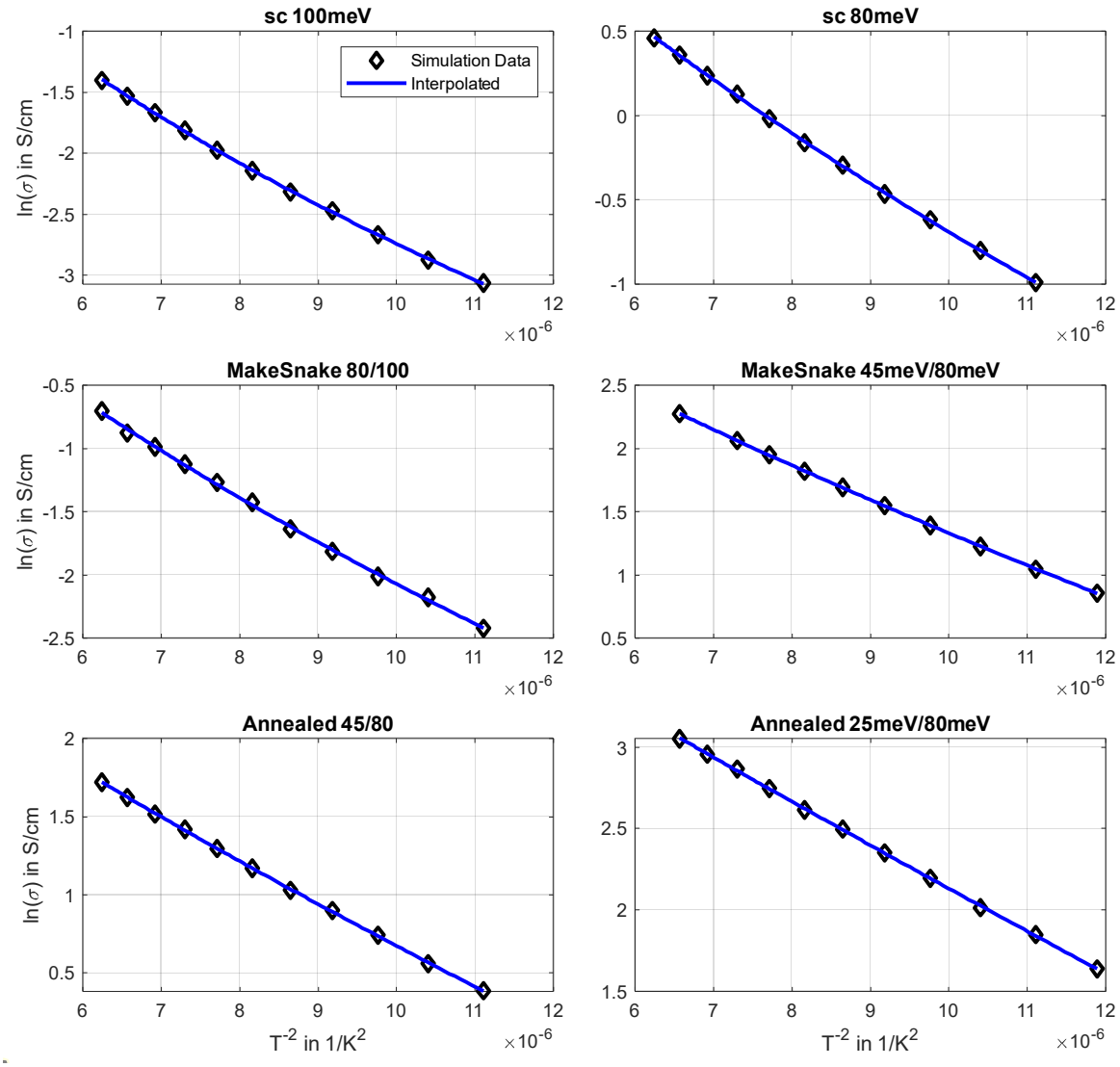

Figure 25 – Temperature dependence of different morphologies. Conductivity is logarithmic and plotted over T^{-2}. Lines are fits to $\ln(\sigma/\sigma_0) \propto -1/T^{\beta}$. Fit parameters are given in SI.

The temperature range of the simulations was from $T = 290\,K$ to $390\,K$ or $T = 300\,K$ to $400\,K$. The temperature dependence was plotted as $\log(\sigma)$ over T^{-2}. There are deviations from a straight line for most morphologies, showing therefore deviations from the $\log(\sigma) \propto -T^{-2}$ law derived for lower temperatures like in Bässler's model. Now for each field, the effective temperature is extracted as described. The results are shown in **Figure 26** and **Table 5**.

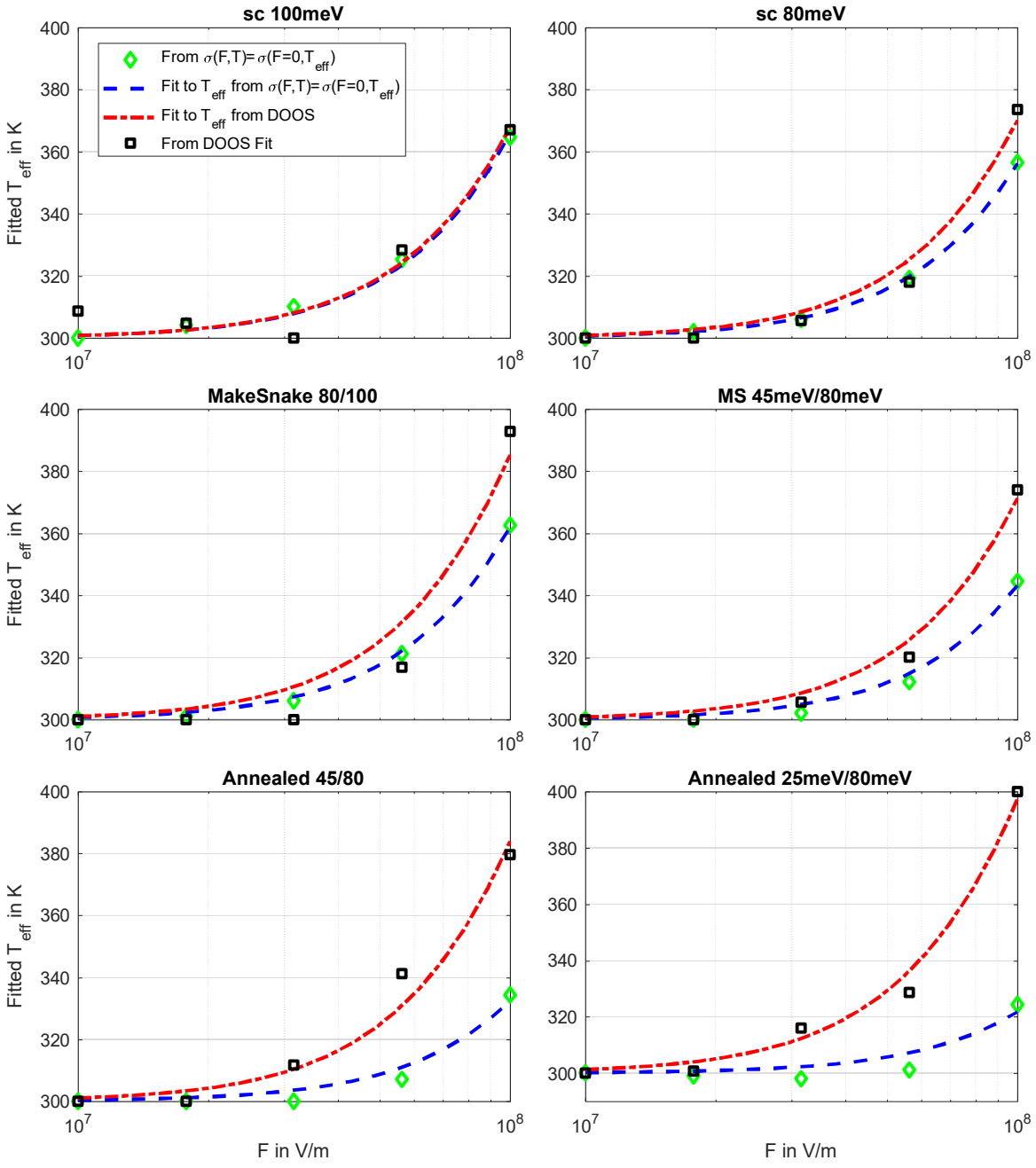

Figure 26 – Extracted effective temperature from the experimental procedure and from the DOOS from the simulations for different morphologies. All datasets are fitted with effective temperature model 2.

Table 5 – Comparison of localization lengths extracted from a fit to the field dependence of the conductivity, a direct fit to effective temperature of the simulation output and from the 'experimental' procedure (Fig. 26). The mean localization length of the input distribution is also given for comparison.

Morphology	α_{fit} from $\sigma(T_{eff}^{(2)})$	α_{fit} from fit to $T_{eff}^{(2)}$	α_{fit} from fit to $T_{eff}^{(2)}$ from $\sigma(F,T) = \sigma(F \approx 0, T_{eff})$	α_{mean}
sc 100	0.40 nm	0.43 nm	0.42 nm	0.43 nm
MS 80/100	0.42 nm	0.50 nm	0.41 nm	0.56 nm
sc 80	0.41 nm	0.44 nm	0.39 nm	0.52 nm
MS 45/80	0.35 nm	0.45 nm	0.33 nm	0.86 nm
AN 45/80	0.31 nm	0.49 nm	0.28 nm	0.61 nm
AN 25/80	0.26 nm	0.54 nm	0.23 nm	0.94 nm

While all values for the localization length in the case of sc 100meV and sc 80meV are similar for each approach, the situation is different for the other morphologies. Just like the fit with Bässler's model or the numerically fitted temperature model, the experimental approach predicts a decreasing localization length with decreasing field dependence, while the mean localization lengths from the inputs double from first to last morphology in **Table 5**. However, compared to Bässler's model (cf. Table 3), the fitted localization length of the experimental approach is significantly higher, while the values from the numerically fitted temperature model (1st column in Table 5) remain close to the experimental approach (3rd column). This first shows that the functional dependence from the effective temperature here is different from Bässler's model, which is supported by the deviations from a straight line in the plot of the temperature dependence of the conductivity. Secondly, even with the numerically correct temperature dependence being comparable to the experimental approach, a significant contribution to the field dependence besides the heating of the charge carrier distribution is missed.

From **Figure 26** it is also evident that while for the homogeneous systems sc 100meV and sc 80meV the effective temperatures obtained experimentally and by fitting the DOOS from the simulation are very close, the deviations get significantly larger for increasing aggregate size. For these inhomogeneous, aggregated systems, the experimental approach produces systematically smaller effective temperatures than the fit to the DOOS from the simulation. It therefore predicts a smaller localization length than the effective temperatures obtained from the DOOS. Inversely, if one would take the actual heating of the charge carrier distribution from the effective temperature obtained from the fit of the DOOS and reverse engineer the

field dependence via $\sigma(F,T_0) = \sigma\left(T_{Eff}(F,T_0)\right)$, one would obtain a significantly stronger field dependence. Also, the strength of the field dependence cannot solely be explained by the morphology, since otherwise the effective temperature curve of e.g. Annealed 25/80 would lie above the curve of Annealed 45/80, which is not the case. Therefore, the inhomogeneity and also the decreasing disorder counteract the heating effect. This once more indicates that indeed the effective temperature alone cannot be the determining quantity for the field dependence of organic semiconductors. At least both disorder and morphology significantly impact the field dependence.

Another contribution to the field dependence might also lie in the (position of the) transport energy, which however is also connected to the disorder and the morphology.

This can be seen from the Mott-Martens model, where the (zero field) conductivity is determined as $\sigma \propto \exp\left(-\frac{E_{tr}-E_F}{k_B T}\right)$. The transport energy and Fermi energy are shown in **Figure 27**.

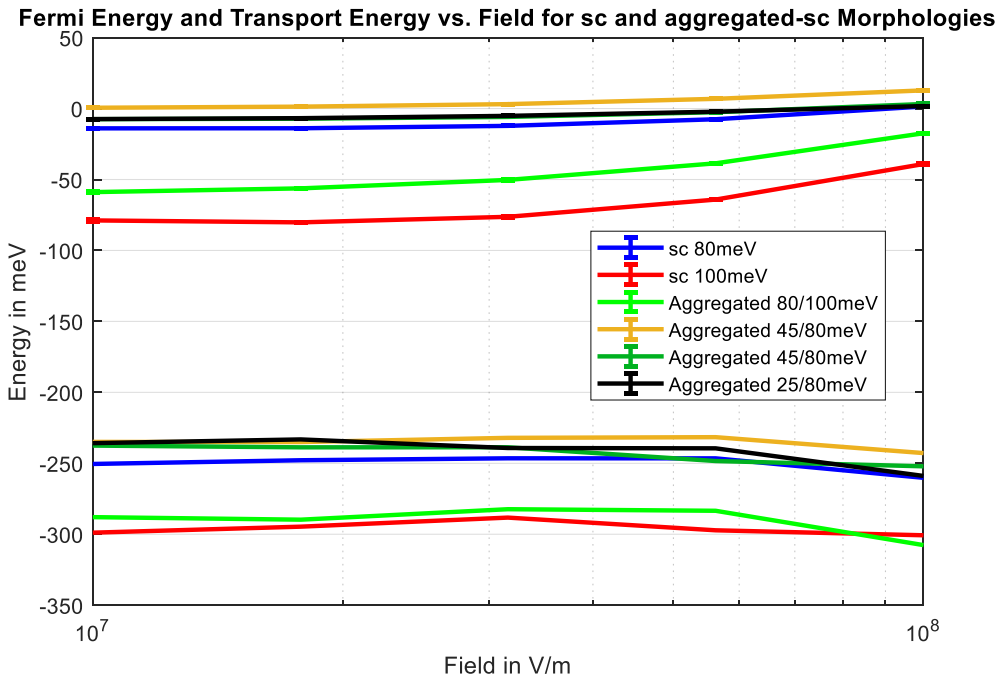

Figure 27 – Transport energies (upper curves) and Fermi energies (lower curves) for different morphologies.

The Fermi energy is less sensitive to the field (Figure 27) and the observed deviations form a constant value are more due to fitting errors in the DOOS fitting procedure. One can therefore approximately treat it as constant with field. The transport energy however is field dependent, which can be explained by the heating of the charge carriers through the field. This effect is more pronounced with higher disorder. From that alone, one would expect a decreasing conductivity, but the heating of charge carriers through the field counteracts that. The net effect could therefore be small, as can be seen in the field dependencies of the morphologies with higher disorder, which are enhanced and not reduced. However, with increasing transport energy, thus moving towards the center of the DOS, the charge carriers get more delocalized since the localization length distribution gets more delocalized towards the center. This would then lead to an enhanced field dependence.

Lastly, there are additional points to mention concerning the morphology or geometry of the OSC itself. First, most theories, just like the effective temperature model together with Bässler's model assume field-independent conduction/percolation paths. This is however not true. With increasing electric field, previously hard hops can be activated and produce shortcuts in the percolation route of charge carriers. This purely geometric effect leads to an increasing field dependence and is strongly morphology dependent. Also, most theories work in homogeneous or effective medium approaches to be able to treat the generally complicated problem analytically. This however can underestimate the morphology effects drastically, especially in highly energetically and spatially correlated systems, as it is the case here through the modelling of the OSC with a tight binding model. As last point to mention concerning the effective temperature approach is that intuitively, the field dependence cannot be solely explained by an isotropic effect which the field induced heating of charge carriers is, since an electric field is per definition anisotropic. One should therefore usually not expect, that an anisotropic effect can be solely explained by an isotropic modification.

Field Dependence of the conductivity from Molecular Dynamics Morphologies

In this section the same analysis is performed for the Molecular Dynamics morphologies of P3HT with chain lengths of 4, 8, 16 and 32 (called 4mer, 8mer, 16mer and 32mer) provided by P.S. Floris. Details on the MD simulations are given in the Theory and Methods section.

For the tight binding model, the transfer integral scaling factor was taken to be $\nu_0 = 1.5 \times 10^{14} \frac{1}{s}$. Again, no ions are considered, so $V = 0$. The diagonal disorder is throughout taken to be $75\, meV$. The critical angle between monomers within the same chain for a conjugation break was taken as 40°. The orbital parameters of the monomer sites are $(l_x, l_y, l_z) = (1.2, 1.2, 0.8) \cdot 0.1\, nm$, i.e. flattened spheres. For the different oligomers, two cases of intra-chain enhancement factors were considered, one moderate $f_{ich} = 1.3$ and one larger $f_{ich} = 10$. **Figure 28** shows a fraction of the chains of each MD morphology.

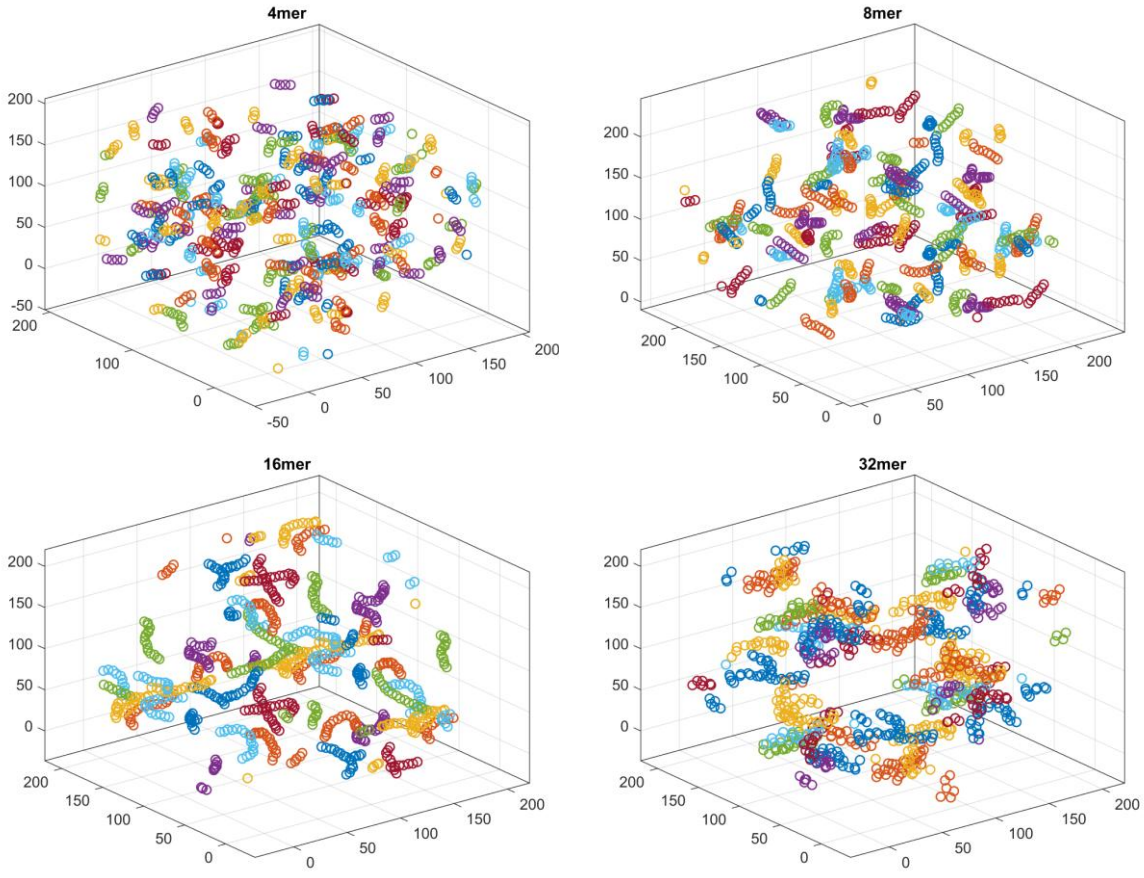

Figure 28 – Visualization of fractions of different P3HT oligomer morphologies generated by Molecular Dynamics.

The 4mer morphology consists out of homogeneously distributed chains, which are mostly very straight because of the rigidity of the backbone and the small chain length. The 8mer morphology is similar, the chain length is still short enough to have mostly straight chains due to the rigidity. The situation starts to change in the 16mer case, where the chains are long enough to bend creating U or S shaped chains mostly. In the 32mer case the rigidity is not sufficient anymore for the length of chains and steric effects cause significant spatial disorder and clumping of chains with more conjugation breaks.

The 2D projections of slices of the COM lattice for each oligomer morphology in the case of smaller intra-chain coupling are shown in **Figure 29**.

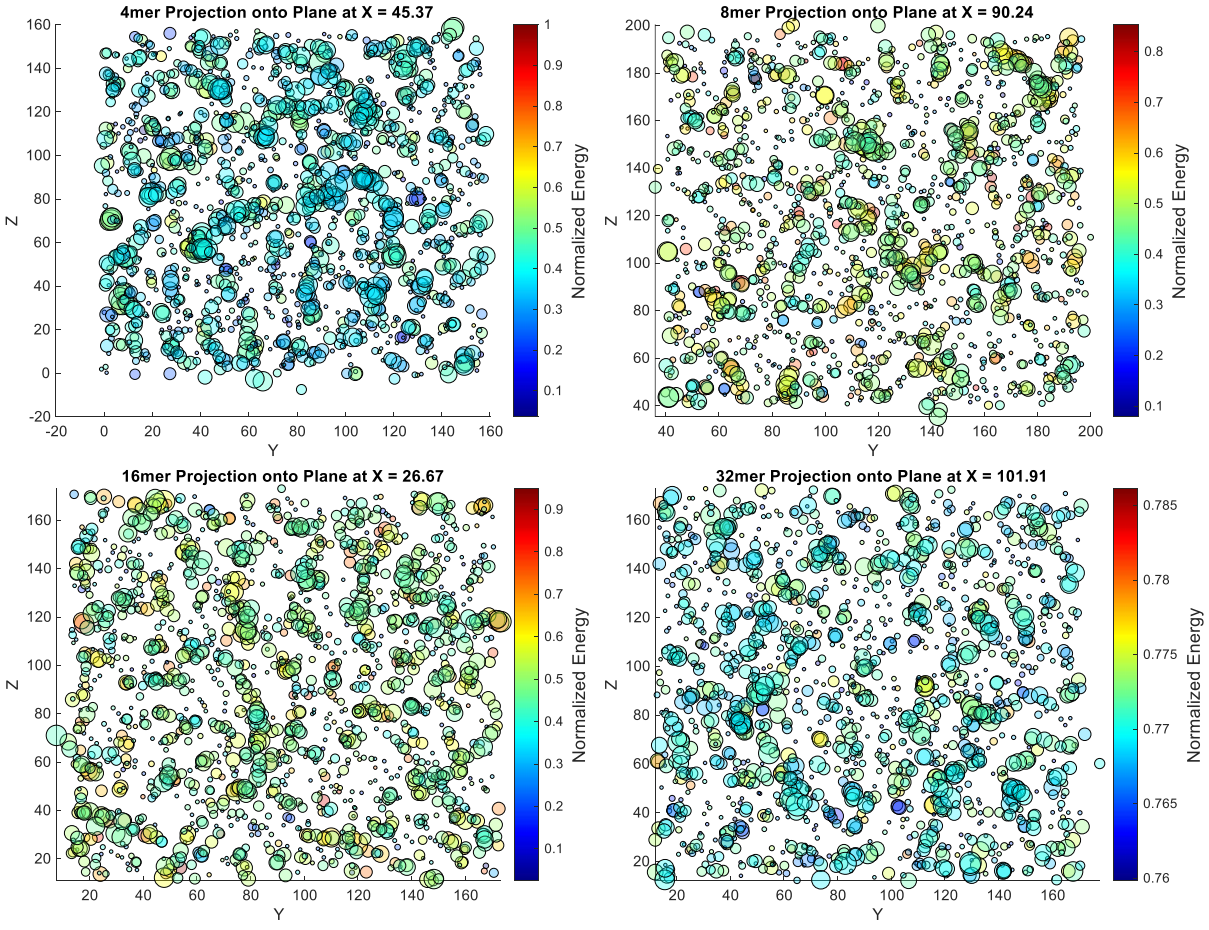

Figure 29 – Projections of slices of the COM lattices for different oligomers of P3HT for $f_{ich} = 1.3$.

The COM lattices basically show the same behavior as seen and described for the original MD morphologies, namely homogeneously distributed and randomly orientated chains.

The same holds for the high intra-chain coupling in **Figure 30**, except for the larger delocalization along the chains. It's noted here, that for the case of $f_{ich} = 10$ the 32mer morphology was not considered since some unresolved error in the data occurred.

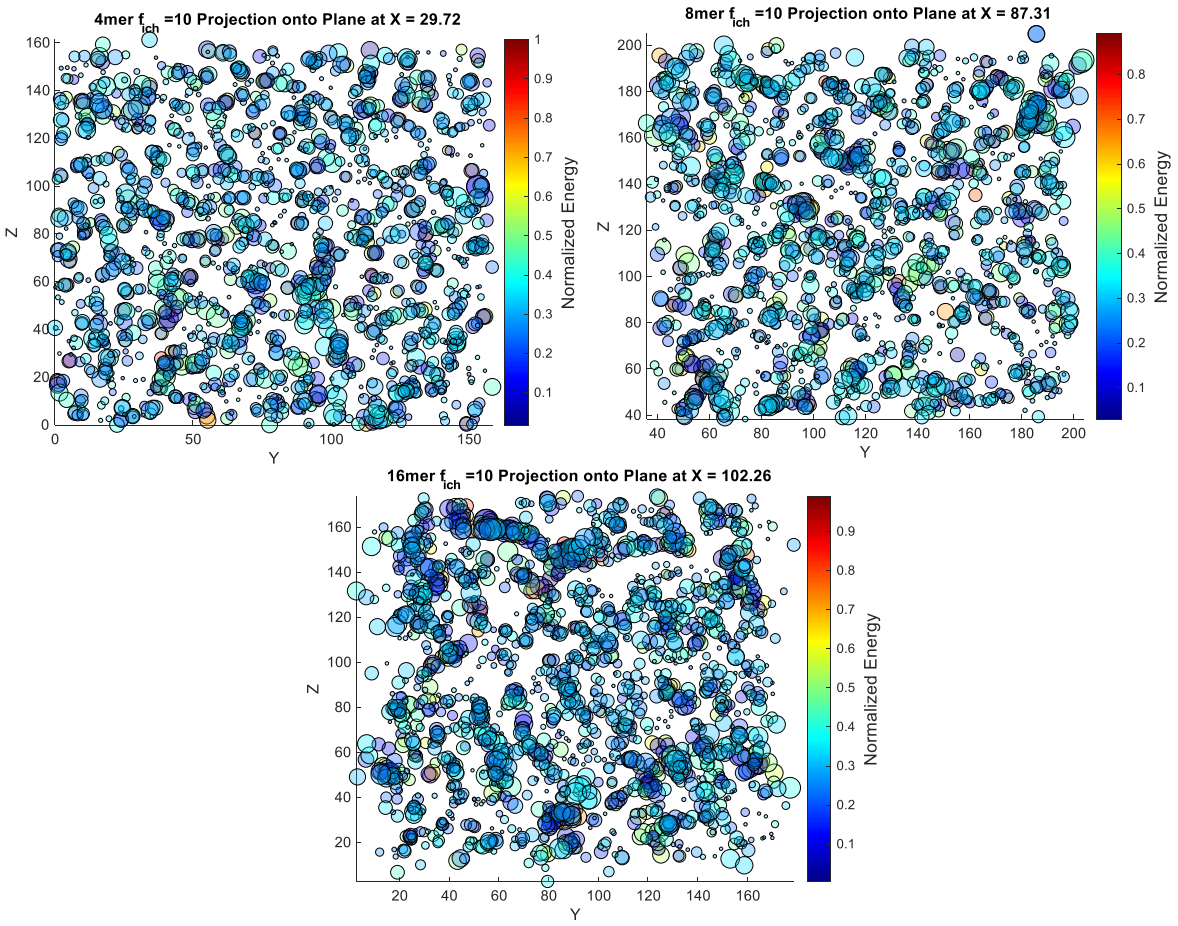

Figure 30 – Projections of slices of the COM lattices for different oligomers of P3HT for $f_{ich} = 10$.

Performing the tight binding diagonalization, the results of the therefrom obtained DOS and localization length distributions are shown in **Figure 31** for $f_{ich} = 1.3$ and $f_{ich} = 10$ in **Figure 32**. For the $f_{ich} = 1.3$ case, the DOS give gaussian distributions, all with a disorder of $\sigma_{DOS} = 80 \pm 3\ meV$. It should be noted here, again, that for the 32mer configuration some numerical artefacts occurred producing far outliers in energy. Therefore, these energies got assigned a

cutoff value of $E_{min/max} = \mp 15 k_B T$. The localization length distributions all look very similar. The mean localizations of all configurations are shown in **Table 6**.

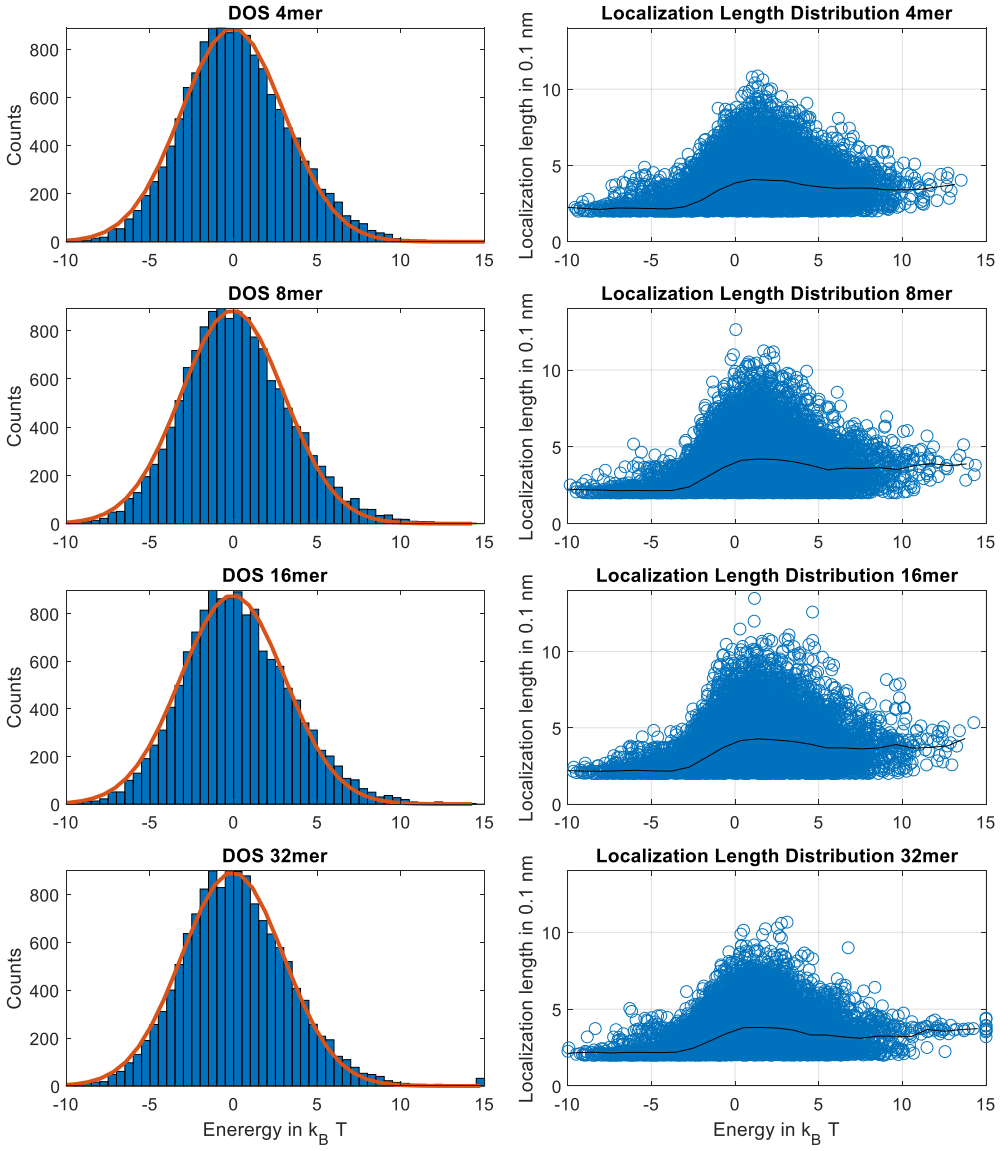

Figure 31 – Left column: DOS of the different oligomer morphologies for $f_{ich} = 1.3$. The orange curves are single gaussian fits. Right column: Corresponding localization length distributions with the mean localization curve in black.

Table 6 – Mean localization lengths of the oligomer configurations for $f_{ich} = 1.3$.

Morphology	4mer	8mer	16mer	32mer
α_{mean}	0.34 nm	0.35 nm	0.35 nm	0.3 nm
σ_{DOS}	80 meV	80 meV	80 meV	80 meV

The relatively small intra-chain enhancement factor of $f_{ich} = 1.3$ causes only a slight increase in localization length with increasing chain length. Eventually, the spatial disorder especially in the 32mer case causes a higher localization than for the other oligomers. The situation changes a little bit for the higher intra-chain coupling enhancement factor of $f_{ich} = 10$ (**Figure 32**).

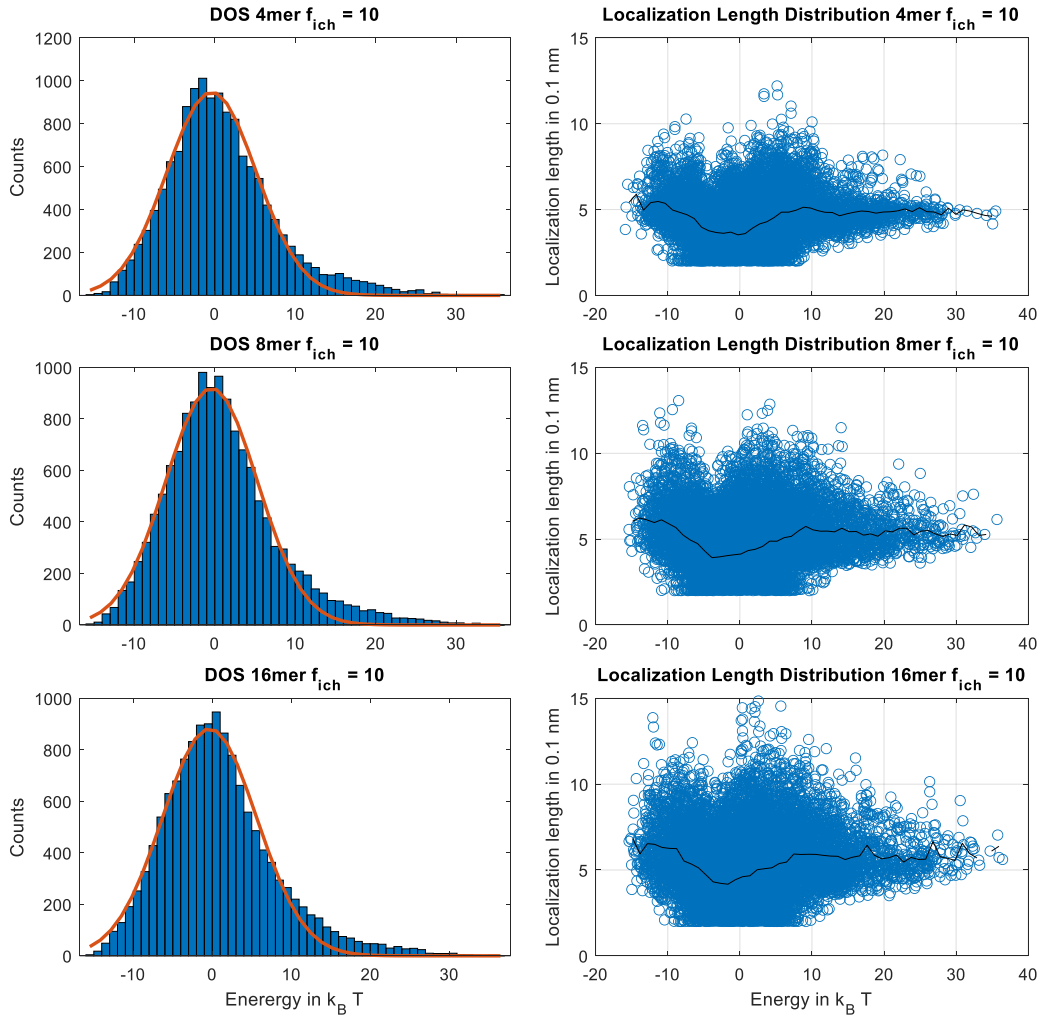

Figure 32 – Left column: DOS of the different oligomer morphologies for $f_{ich} = 10$. The orange curves are single gaussian fits. Right column: Corresponding localization length distributions with the mean localization curve in black.

Table 7 – Disorder and mean localization lengths of the oligomer configuration with $f_{ich} = 10$.

Morphology	4mer	8mer	16mer
σ_{DOS}	137 meV	142 meV	150 meV
α_{mean}	0.42 nm	0.47 nm	0.5 nm

For higher intra-chain coupling, the energetic disorder is expectedly enhanced and a small high-energy tail forms, which however is not very relevant for charge transport. The disorders increase a little bit for larger chain lengths. At the same time, the mean localization length is enhanced for longer chain lengths, explained by the higher chain length over which the wavefunction can delocalize with higher intrachain coupling, see **Table 7**. The high intrachain coupling also explains the higher delocalization of lower energy states compared to the smaller intrachain coupling case.

In the following, the field dependence results are presented. All simulations were performed at a charge carrier density of $c_f = 0.5\%$. **Figure 33** shows the results for the $f_{ich} = 1.3$ case.

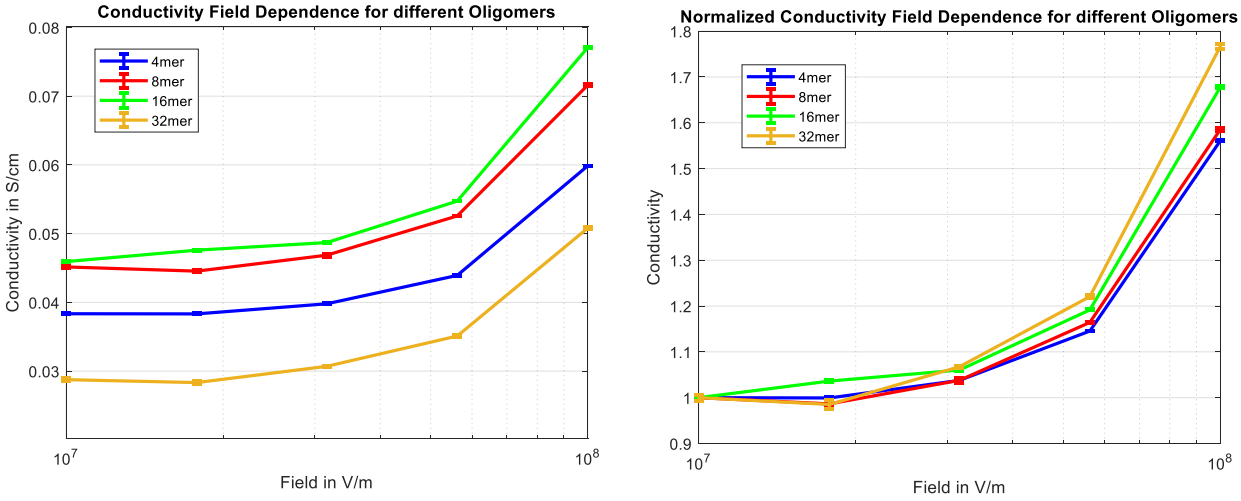

Figure 33 – Left: Conductivity field dependence of different oligomer morphologies. Right: Normalized conductivity field dependence.

While in this case, the DOS have almost the same disorder, the localization length increases slightly until a chain length of 16mer. Also, for longer chains there are for conduction more efficient intra-chain hops as long as the chains are not too deformed. From that, it is evident that also the conductivity gets larger until the 16mer. The smaller localization length and the spatial disorder of the 32mer case however leads to a decrease in conductivity. This is also due

to the artificially low traps that are induced through the energetic cutoff as mentioned above. For the field dependence one can see that it is quite similar, but increases slightly with chain length. This has again two causes. On the one hand, slightly more delocalization leads to slightly stronger field dependence with increasing chain length. In the 32mer case, there is more spatial disorder compared to the other cases, which enhances the field dependence in this case, also probably together with the artificial deep traps. This additional disorder overcompensates the effect of the slightly reduced localization length on the field dependence. This again shows that disorder, both energetic and spatial, has a higher effect on the field dependence than slight changes in localization length.

Figure 34 shows the field dependence for the $f_{ich} = 10$ case.

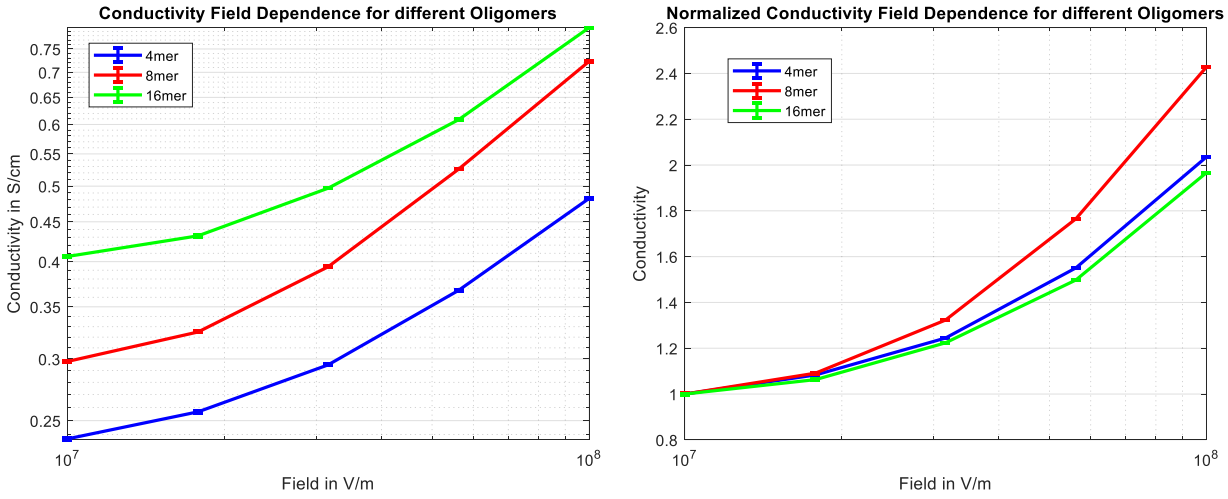

Figure 34 – Left: Conductivity field dependence of different oligomer morphologies for the $f_{ich} = 10$ case. Right: Normalized conductivity field dependence.

For this case, the situation seems unexpected. While the total conductivity is still expectedly increasing due to the increasing delocalization length with chain length, the field dependence is much different. From just disorder and localization length one would, from the two main rules considered so far, expect the 16mer case to have the highest field dependence; it however has the weakest, or basically the same as the 4mer case. I attribute this to two possible reasons. One is that the transport energy (see **Figure 35**) of the 16mer case for $f_{ich} = 10$ is deeper and more field dependent than for the other two cases. This behavior is absent in the case of $f_{ich} = 1.3$, where the differences of the different oligomers are negligible and

therefore have no influence. As discussed in the previous section, this has a negative effect on the field dependence, which here might not be fully compensated by heating to the effective temperature. It should be noted that the apparent field dependence of the Fermi energy in this case is, as before, an artefact of the fitting procedure, since the calculated Fermi energies are deeper than the lowest states of the DOS due to the high disorder.

Another possible reason might be reverse field hopping[92,93]. In the 16mer case, the chains are not as stiff anymore and are bend. The high intra-chain coupling can make hopping in the electric field direction less efficient in the chain region where the chain bends back against the field, which can have a negative effect on the field dependence.

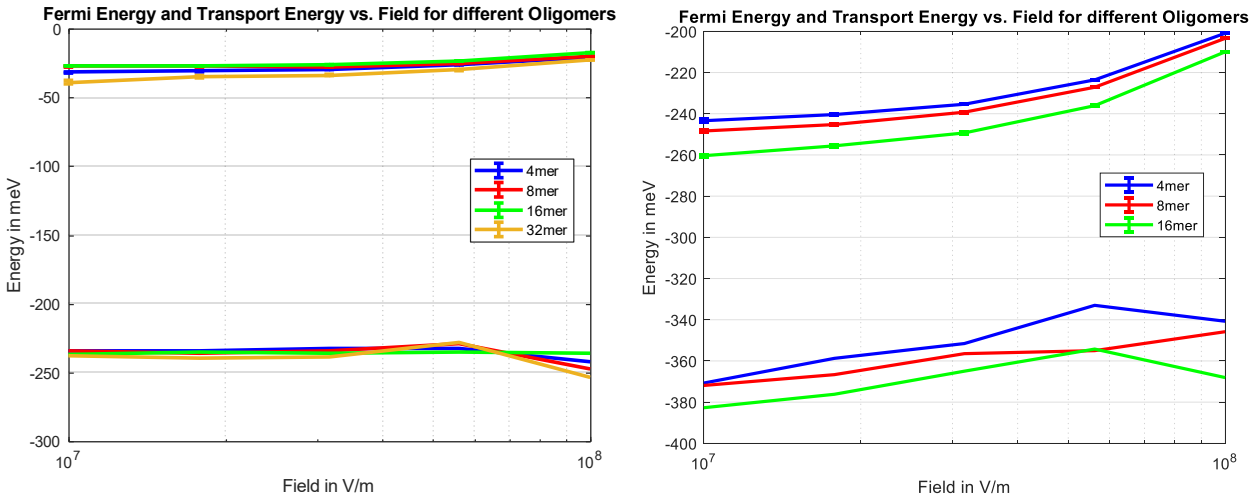

Figure 35 – Left: Transport energy (upper curves) and Fermi energy (lower curves) for different oligomer morphologies in the case of $f_{ich} = 1.3$. Right: Transport energy (upper curves) and Fermi energy (lower curves) for different oligomer morphologies in the case of $f_{ich} = 10$.

In the following **Figure 36** and **Tables 8** and **9**, the field dependencies are fitted to the field dependence models from effective temperature (left) and the effective temperatures from the DOOS fits from the simulation are fitted to the two effective temperature models (right), as done in the past section.

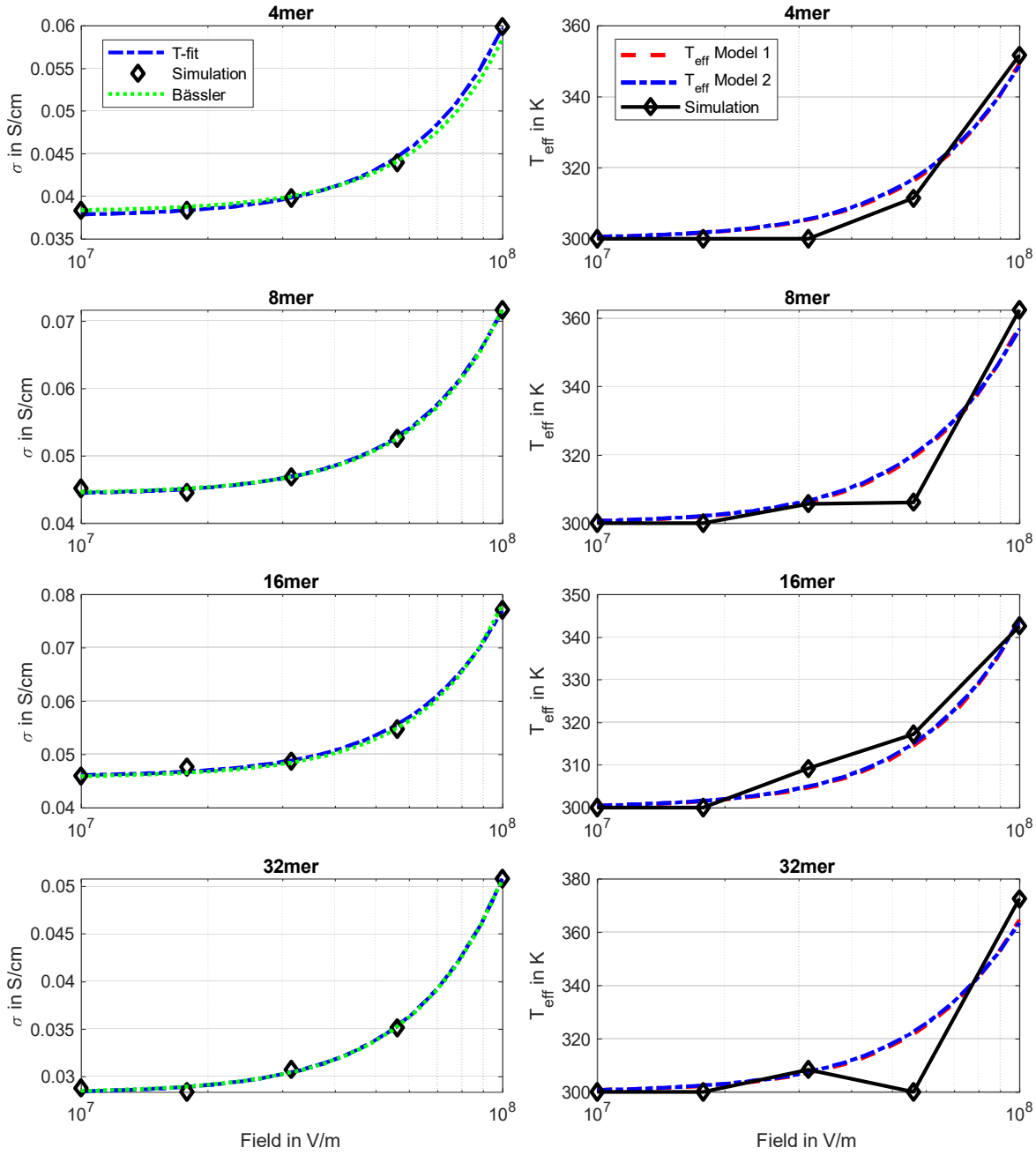

Figure 36 – Left column: Fits to the field dependence models using effective temperature model 2 on the different oligomer morphologies for $f_{ich} = 1.3$. Right column: Fits to the effective temperature from the DOOS fits in the simulation with both effective temperature models.

Table 8 – Localization lengths from fits of $\sigma\left(T_{eff}(F)\right)$ to the simulated data for different oligomer morphologies $(f_{ich} = 1.3)$ (Figure 36, left). The last column gives the mean localization length from the $\alpha(E)$ distributions obtained from the tight binding calculations for comparison. $T_{eff}^{(2)}$ is the effective temperature model 2.

Morphology	Model	α from $\sigma\left(T_{eff}^{(2)}\right)$	α_{mean}
4mer	Bässler	0.17 nm, C=0.6	
4mer	$\sigma(T)$ Fit	0.28 nm	0.34 nm
8mer	Bässler	0.22 nm, C=0.42	
8mer	$\sigma(T)$ Fit	0.29 nm	0.35 nm
16mer	Bässler	0.19 nm, C=0.62	
16mer	$\sigma(T)$ Fit	0.30 nm	0.35 nm
32mer	Bässler	0.3 nm, C=0.33	
32mer	$\sigma(T)$ Fit	0.35 nm	0.3 nm

Table 9 – Localization length from fits of the effective temperature models 1 and 2 onto the effective temperatures obtained from the simulations (Figure 36, right). Mean localization length, localization length at transport energy and Fermi level from the localization length distributions from Tight Binding calculations for comparison in the last columns. Errors for fitting approximately $\Delta\alpha \approx 0.05\ nm$.

Morphology	α from $T_{eff}^{(1)}$	α from $T_{eff}^{(2)}$	α_{mean}	$\alpha(E_{tr})$	$\alpha(E_F)$
4mer	0.24 nm	0.36 nm	0.34 nm	0.35 nm	0.25 nm
8mer	0.27 nm	0.39 nm	0.35 nm	0.35 nm	0.25 nm
16mer	0.23 nm	0.34 nm	0.35 nm	0.35 nm	0.25 nm
32mer	0.28 nm	0.42 nm	0.3 nm	0.3 nm	0.25 nm

Considering the errors in the effective temperatures from fitting the DOOS in the simulation, the values of the localization length from the fitting with model 2 agree reasonably well with the mean localization length or equally the localization length at the transport energy (**Table 9**). Only the 32mer has a higher deviation, which might be explained by higher spatial disorder and inhomogeneity, as discussed before. As encountered before, the first effective temperature model gives lower values for the localization length. The localization length obtained by fitting Bässler's model however gives poor results with more spread (**Table 8**). The

results again correlate with a varying c parameter. Higher c fitting values lead to a lower fitted localization length. The model with the numerical fits to the temperature dependence (see **Figure 38** for the simulated temperature dependencies) however give better results with values closer to the input localization lengths.

The fitting results for the $f_{ich} = 10$ case are shown in **Figure 37** and **Tables 10** and **11**.

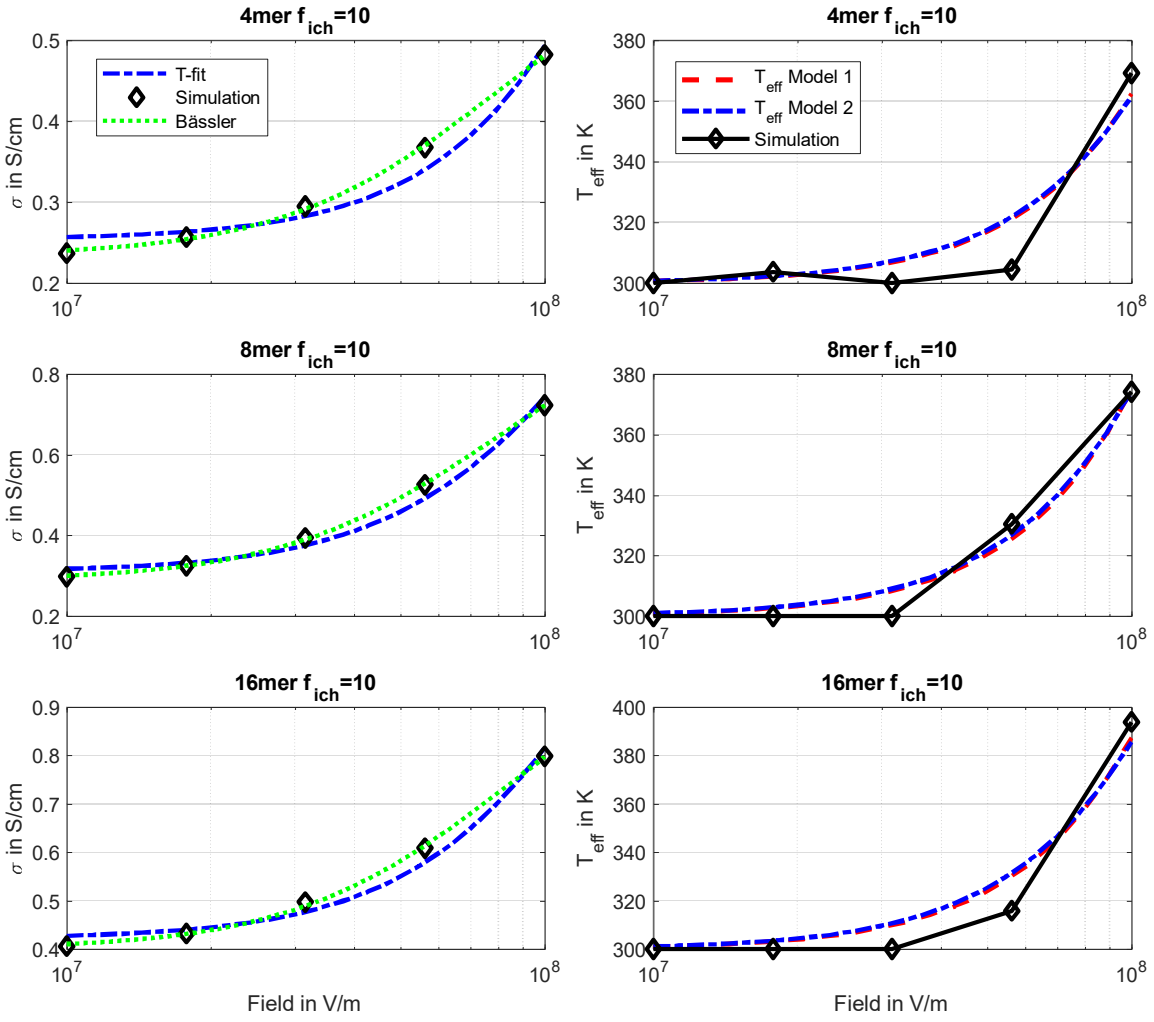

Figure 37 – Left column: Fits to the field dependence models using effective temperature model 2 on the different oligomer morphologies for $f_{ich} = 10$. Right column: Fits to the effective temperature from the DOOS fits in the simulation with both effective temperature models.

Table 10 – Localization lengths from fits of $\sigma\left(T_{eff}(F)\right)$ to the simulated data for different oligomer morphologies ($f_{ich} = 10$) (Figure 37, left). The last column gives the mean localization length from the $\alpha(E)$ distributions obtained from the tight binding calculations for comparison. $T_{eff}^{(2)}$ is the effective temperature model 2.

Morphology	Model	α from $\sigma\left(T_{eff}^{(2)}\right)$	α_{mean}
4mer	Bässler	0.97 nm, C=0.04	
4mer	$\sigma(T)$ Fit	0.64 nm	0.42 nm
8mer	Bässler	1.05 nm, C=0.04	
8mer	$\sigma(T)$ Fit	0.83 nm	0.47 nm
16mer	Bässler	0.92 nm, C=0.03	
16mer	$\sigma(T)$ Fit	0.66 nm	0.5 nm

Table 11 – Localization length from fits of the effective temperature models 1 and 2 onto the effective temperatures obtained from the simulations (Figure 37, right). Mean localization length, localization length at transport energy from the localization length distributions from tight binding calculations for comparison in the last columns. Errors for fitting approximately $\Delta\alpha \approx 0.05\ nm$.

Morphology	α from $T_{eff}^{(1)}$	α from $T_{eff}^{(2)}$	α_{mean}	$\alpha(E_{tr})$
4mer	0.28 nm	0.41 nm	0.42 nm	0.5 nm
8mer	0.31 nm	0.46 nm	0.47 nm	0.6 nm
16mer	0.33 nm	0.5 nm	0.5 nm	0.7 nm

Again, the fit parameters obtained from Bässler's model are very poor. On the one hand, the localization length is significantly overestimated. Secondly, also the c parameter is one order of magnitude lower than usually considered values and what has been obtained for all other morphologies considered here. Therefore, this model is not suitable for these morphologies. In this case however, also the values obtained for α with the model using the numerical fit to the temperature dependence (see **Figure 38** for the simulated temperature dependencies for $f_{ich} = 10$) are overestimated compared to the input values. The high intra-chain coupling seems to have a significant impact on the details of the field dependence. On the other hand, the fit values of the localization length from fitting effective temperature model 2 to the simulation data of the effective temperature match perfectly with the mean localization length

of the distributions. Next, the results from the experimental approach are compared in the following **Figures 39** and **40** and **Tables 12** and **13**.

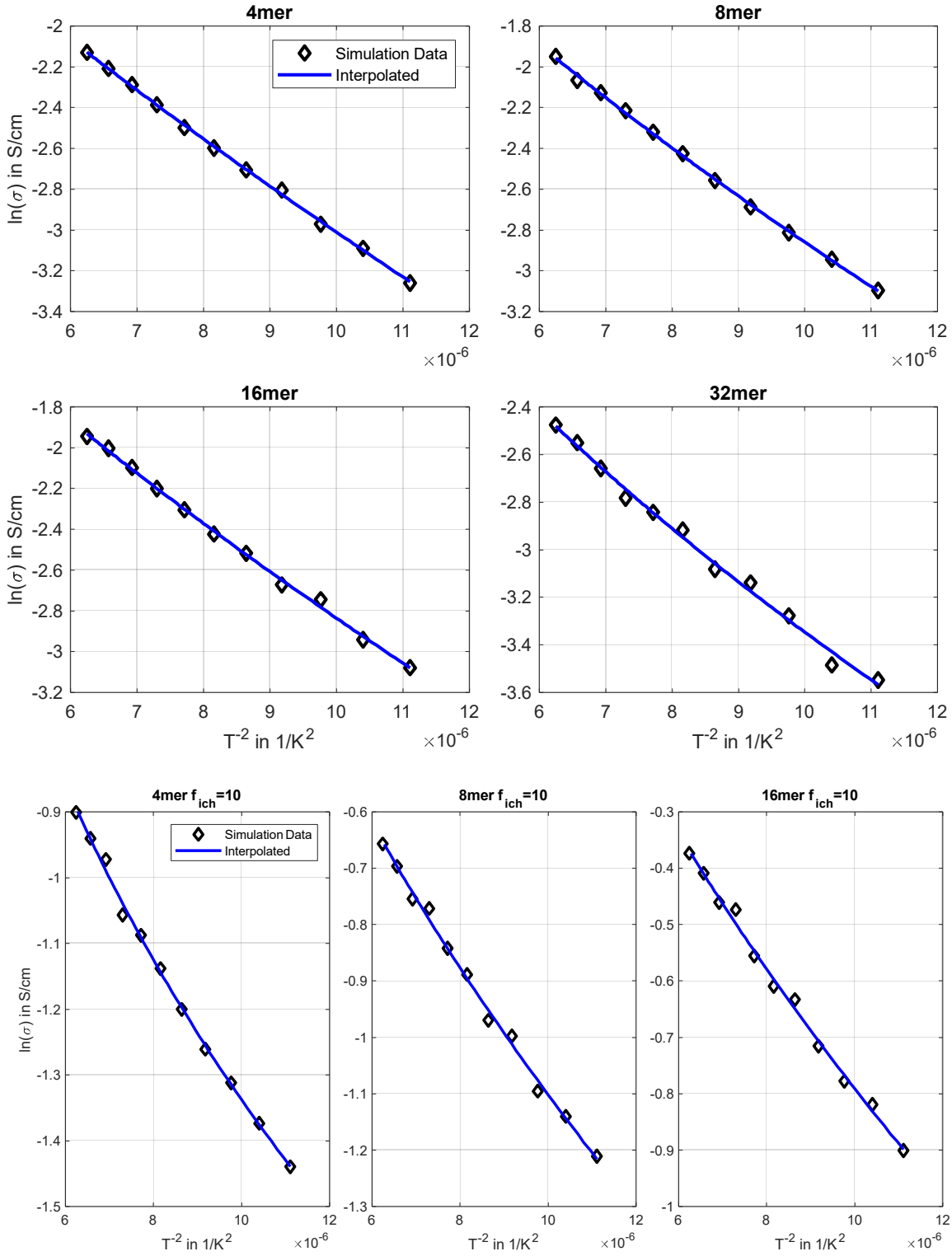

Figure 38 – Temperature dependence of different oligomers for $f_{ich} = 1.3$ and $f_{ich} = 10$.

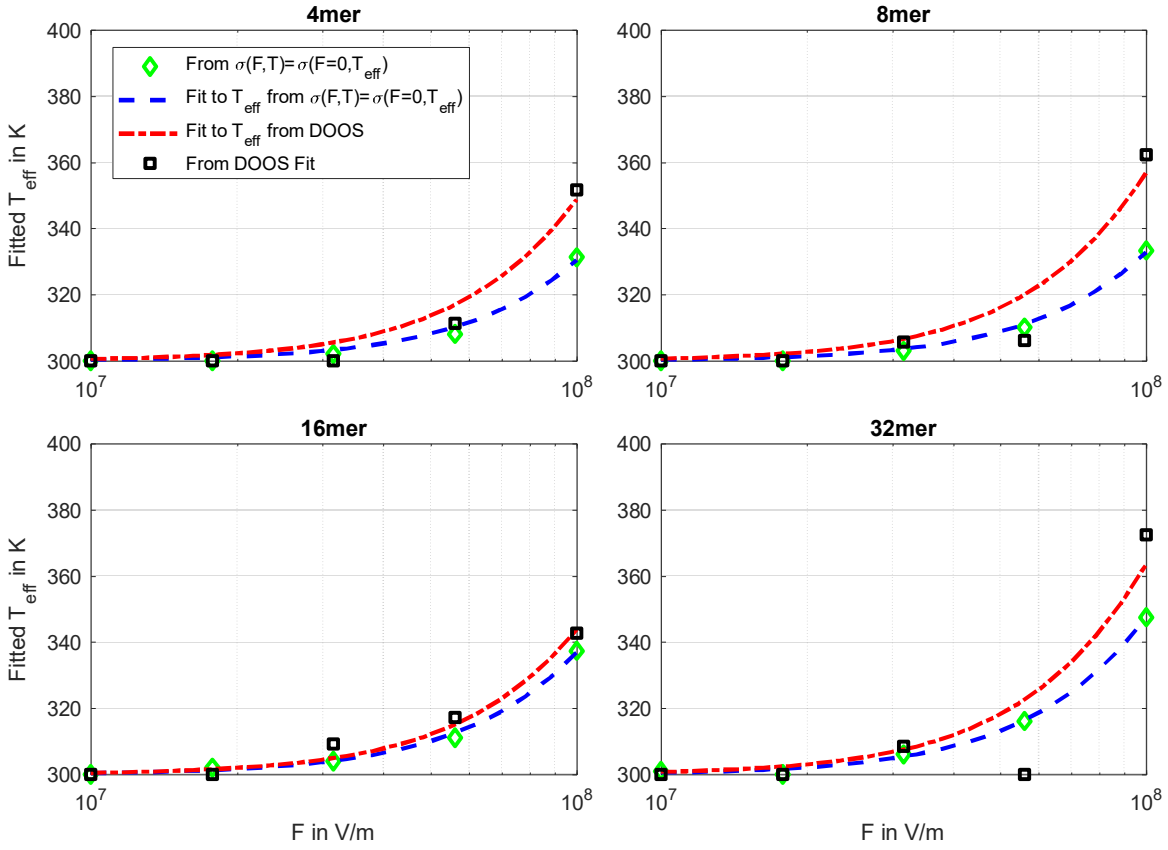

Figure 39 – Extracted effective temperature from the experimental procedure and from the DOOS from the simulations for different oligomers in the case $f_{ich} = 1.3$. All datasets are fitted with effective temperature model 2, respectively.

Table 12 – Comparison localization lengths extracted from fit to field dependence, by direct fit to effective temperature of the simulation output and the experimental procedure in the case $f_{ich} = 1.3$ (Figure 39). The mean localization length of the input distribution is also given for comparison.

Morphology	α_{fit} from $\sigma(T_{eff}^{(2)})$	α_{fit} from fit to $T_{eff}^{(2)}$	α_{fit} from fit to $T_{eff}^{(2)}$ from $\sigma(F,T) = \sigma(F \approx 0, T_{eff})$	α_{mean}
4mer	0.28 nm	0.36 nm	0.27 nm	0.34 nm
8mer	0.29 nm	0.39 nm	0.29 nm	0.35 nm
16mer	0.30 nm	0.34 nm	0.30 nm	0.35 nm
32mer	0.35 nm	0.42 nm	0.35 nm	0.30 nm

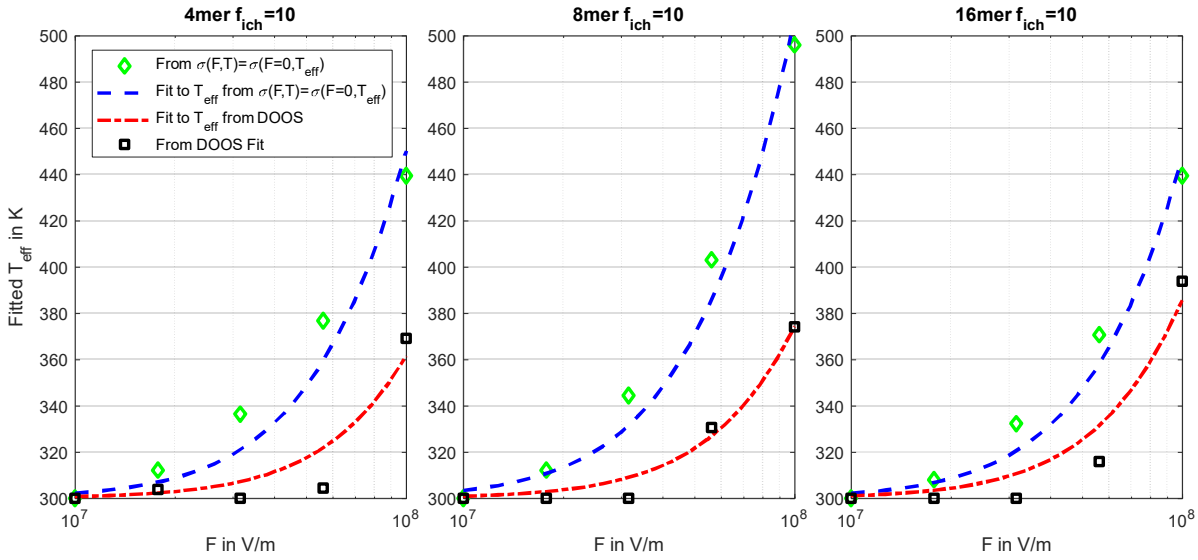

Figure 40 – Extracted effective temperature from the experimental procedure and from the DOOS from the simulations for different oligomers in the case $f_{ich} = 10$. All datasets are fitted with effective temperature model two, respectively.

Table 13 – Comparison localization lengths extracted from fit to field dependence, by direct fit to effective temperature of the simulation output and the experimental procedure in the case $f_{ich} = 10$ (Figure 40). The mean localization length of the input distribution is also given for comparison.

Morphology	α_{fit} from $\sigma(T_{eff}^{(2)})$	α_{fit} from fit to $T_{eff}^{(2)}$	α_{fit} from fit to $T_{eff}^{(2)}$ from $\sigma(F,T) = \sigma(F \approx 0, T_{eff})$	α_{mean}
4mer	0.64 nm	0.41 nm	0.71 nm	0.42 nm
8mer	0.83 nm	0.46 nm	0.89 nm	0.47 nm
16mer	0.66 nm	0.50 nm	0.70 nm	0.50 nm

The discussion is started with the case of $f_{ich} = 1.3$ (**Figure 39** and **Table 12**). Both the localization lengths of the model with the numerically fitted temperature dependence and the experimental approach give consistently the same result. However, compared to the effective temperature obtained from the DOOS fitting in the simulation, the curves lie slightly lower. This might partially be due to higher errors from the DOOS fit, but hints also towards underestimation of other factors determining the field dependence as discussed before. The polymerical structure can act as an inhomogeneity, leading to a slightly reduced field dependence. However, the additional intra-chain coupling is small, therefore the effect is

rather small, the curves and especially the points on which they are fitted are close and the obtained values of the localization length are comparable to the input. This case is therefore more comparable to the homogeneous systems sc 80meV and sc 100 meV in the last section. If now the inhomogeneity of the morphology is enhanced by considering a high intra-chain coupling, one should expect deviations. Indeed, looking at the obtained results for $f_{ich} = 10$ in **Figure 40** and **Table 13**, the differences are much more significant. While again, the model with numerically fitted temperature dependence and the experimental approach give very similar results within the error bounds, the deviations from the effective temperature obtained by fitting the DOOS is significant. Interestingly, in this case the obtained effective temperatures and therefore localization lengths are significantly higher than from the DOOS case and the input localization lengths, where latter two give the same localization length. The highest effective temperature curve is obtained for the 8mer case, consistently with the highest field dependence. This behavior is opposite to the behavior that was obtained for the more aggregated morphologies from the last chapter, where the effective temperature curves and therefore localization lengths lie under the effective temperature curve obtained from DOOS. An explanation might be the different morphological structure here. While previously considered cases are homogeneous or aggregated, here the morphology might resemble more some kind of filamental structure where inter-chain hopping is minimized while intra-chain hopping is maximized. However, in this model the delocalization is treated isotropically, but enhanced delocalization along a chain would give more anisotropic localization lengths. This could lead to slight deviations in this case, but probably not change the qualitative result. Also, the considerably higher energetic disorder in this case could again play a decisive role. In any case, the field dependence is here much more enhanced than expected by heating of the charge carrier distribution.

To sum up this chapter, the effective temperature approach fails to explain the field dependence of OSCs consistently with the given physical parameters like the localization length in simulation. Both the obtained localization lengths from the fit to the field dependence of the conductivity and the experimental approach deviate from the input values. Especially systems containing any kind of inhomogeneity like aggregation or strongly filamental morphologies can lead to significant discrepancies. In the former case, aggregation leads to a reverse trend of localization lengths with respect to the input values, while filamental structures as obtained from the MD morphologies with high intra-chain coupling give higher

localization lengths than the input values. Hereby, the influence of anisotropic delocalization for the filamental morphology should not change the qualitative result, but can be studied in future work. Additionally, the effect of disorder seems not to be properly captured by the simple effective temperature approach and also other influences on the field dependence apart from the effective temperature cannot be excluded. Therefore, the validity of the usage of the effective temperature approach can a priori not be guaranteed for all systems and can possibly lead to misinterpretations of obtained lengths scales in an experimental approach.

However, the apparent experimentally observed strong field dependence for aggregated systems at already lower fields could not be reproduced with the current model and morphologies. It is possible that the considered morphologies do not capture important morphological details besides the aggregation that lead to the observed behavior. First, the too low shift of means of the aggregated and amorphous phase in the DOS should have a significant influence on the charge transport. A more careful treatment of enhanced transfer integrals within the aggregated phase compared to the amorphous phase could partially resolve the issue. Secondly, the considered aggregated morphologies do not give rise to hopping between large delocalized aggregates. Here, the aggregated morphologies consist either of more dense small aggregates or larger aggregates separated by an also larger amorphous phase. For inter aggregate hopping, the total rate of a delocalized state within an aggregate j into other delocalized aggregates $\Gamma_{agg,j\to agg} = \sum_{i\in agg} p_{agg,j\to agg,i}$ must be much larger than the total rate into the amorphous phase $\Gamma_{agg,j\to am} = \sum_{i\in am} p_{agg,j\to am,i}$. Since the number of localized states in the amorphous phase is larger than the number of neighboring aggregates, and the aggregates wavefunction quickly localizes within the amorphous phase with decay length ξ, the amorphous phase should be relatively thin in terms of the wavefunction decay length, $\xi \approx L_{am}$, with L_{am} being the average distance between aggregates. This condition is not fulfilled for the considered aggregated morphologies. As argued in an upcoming paper (cf. list of publications, M. Shokrani et al.) to which this work contributes, hopping between delocalized aggregates could lead to an apparent effective localization length that scales the actual localization length up by a factor like $\sim d/L_{am}$ with the aggregate size d. This effective behavior could lead to an enhanced field dependence at lower fields. To prove this claim numerically however, additional simulations are needed that include the discussed and possibly also other modifications.

Charge Carrier Concentration Dependence

This chapter investigates the conductivity and Seebeck coefficient up to high charge carrier concentrations for the same morphologies that were studied in the chapter about field dependence. In a previous paper[94] experimental results have shown a previously unexplained power law dependence of the conductivity of p-type doped OSC as function of charge density at high charge densities, $\sigma \propto n^s$ with $s \geq 2$. In a semi-analytical Mott-Martens-like approach, it has been shown that this phenomenon can emerge due to partial delocalization of charge carriers. In a more rigorous approach, this result is recovered here with the simulation approach that was developed in this thesis.

All simulation parameters are the same as in the field dependence chapter but with a fixed electric field of $F = 10^7 \frac{V}{m}$ and a charge carrier concentration range of $c_f = 0.1\% - 40\%$.

Simplified Model Morphologies

The discussion starts with the simplified model morphologies again. **Figure 41** shows the charge carrier concentration dependence of the mobility and conductivity of these morphologies.

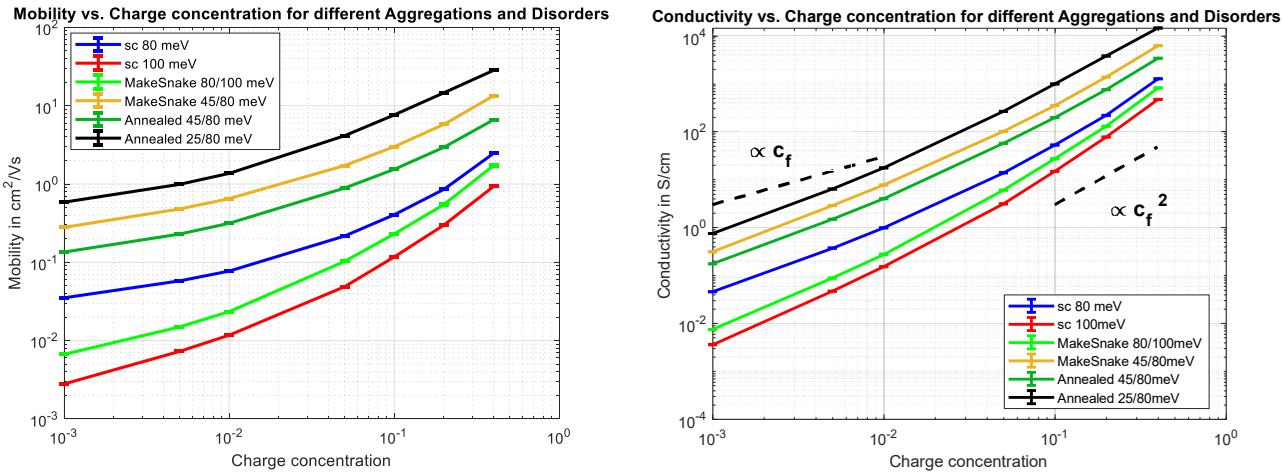

Figure 41 – Left: Mobility as function of charge carrier concentration of different morphologies in a double-log plot. Right: The same for conductivity.

The order of the morphologies of highest to lowest conductivity was already discussed in the previous chapter. The conductivity and mobility get larger with less disorder and higher localization length. The usual approximate relation $\sigma \propto n$ for low charge carrier concentrations is recovered here, the mobility gets increasingly flat for the lowest charge carrier concentrations. It would get even more flat for lower charge carrier concentrations, however, due to the limited simulation box size the lowest senseful charge carrier concentration is around $c_f = 0.1\%$ to have enough simulated charges for reasonable statistics. From Figure 41 it can be seen that the slope of the mobility, and therefore the slope of the conductivity gets increasingly higher towards higher concentrations. This effect is more pronounced for lowest conductivities, i.e. highest disorders. This leads to an approximate power law of $\sigma \propto n^3$ for the lowest conducting morphology sc 100meV and to a power law of $\sigma \propto n^2$ for the highest conducting morphology Annealed 25meV/80meV. To understand this behavior, one needs to look at the Fermi- and transport energies, which are shown in **Figure 42** and look at the localization lengths at the corresponding positions in energy in the localization length distributions **Figure 19** and **22**.

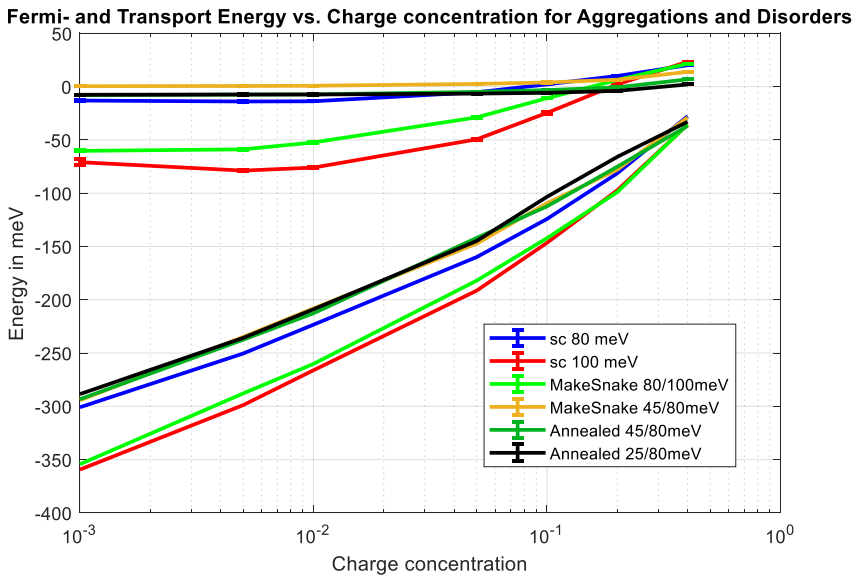

Figure 42 – Transport energies (upper curves) and Fermi energies (lower curves) as function of charge carrier concentration for different morphologies.

From the localization length distributions, one sees the onset of delocalization of charge carriers around above $-50\ meV$ to $-75\ meV$. The Fermi energies start to enter this region at around $c_f = 20\%$. For the highest disorders, the transport energy lies at the onset of delocalization. There, the localization length starts increasing already at around $c_f = 1\%$. The conductivity in the semi-analytical Mott-Martens model is proportional to the critical transfer rate between states at the Fermi energy and the transport energy

$$p(E_{tr}) = \exp\left(-R^*\left(\alpha^{-1}(E_{tr}) + \alpha^{-1}(E_F)\right) - \frac{E_{tr} - E_F}{k_B T}\right) \tag{155}$$

While the dependence on the charge carrier concentration usually mainly comes from the Fermi energy being approximately logarithmic in c_f in the classical Mott-Martens Model, in the model for energy dependent localization length one gets another contribution to the charge carrier concentration dependence from the change of effective localization length $2\left(\alpha^{-1}(E_{tr}) + \alpha^{-1}(E_F)\right)^{-1}$. Therefore, the slope s in $\ln(\sigma) = A + s \cdot \ln(c_f)$ increases if either of both localization lengths $\alpha(E_{tr})$ or $\alpha(E_F)$ starts to increase with c_f. Intuitively it is clear that a rising localization length leads to rising conductivity. Comparing the charge carrier concentrations where either of both localization lengths starts to increase to Figure 41, one sees that these are also approximately the charge carrier concentrations where the slope s

starts to increase. Since for the highest disorders the localization length already starts to rise at the transport energy, the slope gets higher earlier. At higher c_f one then gets an additional contribution from the rising localization length at the Fermi energy. Generally, the slope is dependent on the slope of the localization length distribution and the slope of the transport- and Fermi energy, i.e. how fast in energy the localization length distribution slope is climbed, and the availability of sites (DOS) at these energies. Additionally, the slope gets lower for higher total localization lengths and conductivities, since there is less gain in conductivity to get from even higher delocalization, i.e. a saturation effect. On the other hand, lower conductivities have a higher slope due to a catch-up effect. All this together explains the effect of power law dependence of the conductivity with charge carrier concentration of the different morphologies observed in Figure 41. An explanatory picture of this effect is schematically shown in **Figure 43**.

However, in the simulations the slope is a little bit lower than calculated in the semi-analytical case. The reason for that is the not well-defined localization length curve in this case. Instead of stating that every localization length at a given energy is equal as in the semi-analytical model, here we have a scattered distribution of localization lengths, such that there are also well-localized states at all energies, which lowers the slope.

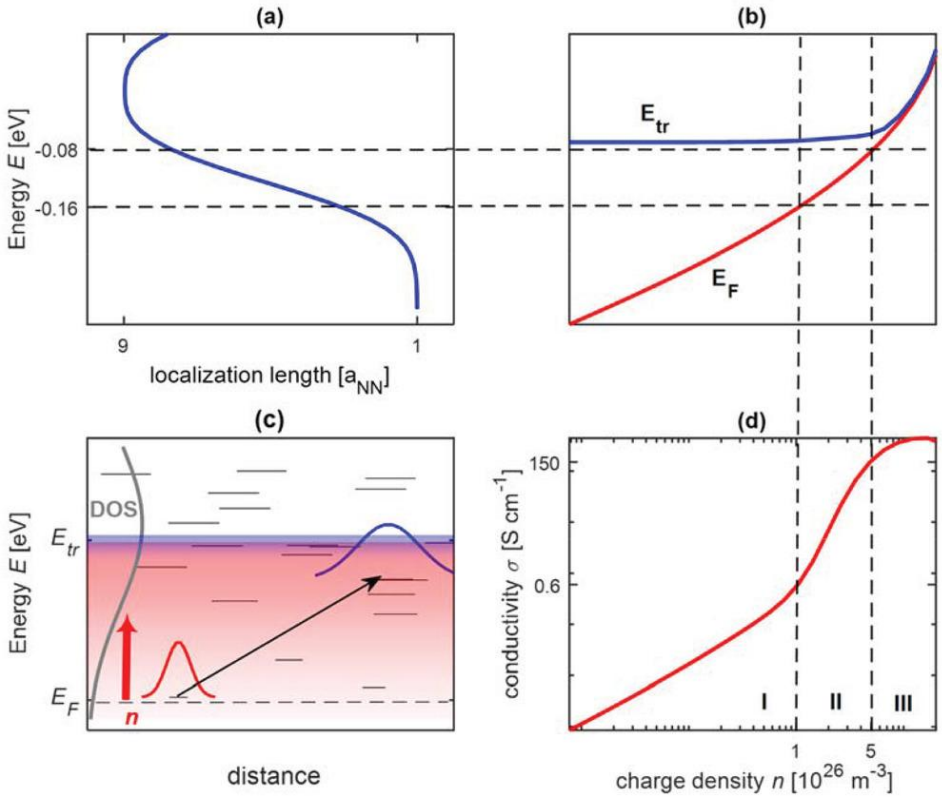

Figure 43 – Illustration of the reason for the change of slopes in the $\sigma(n)$ double-log plots Figure 41. Panel **(a)** shows the dependence of the localization length vs. site energy, which, using the charge density dependence of the Fermi and transport energies in panel **(b)** can be converted to the conductivity vs density relation in panel **(d)**. Panel **(c)** illustrates the hopping process between two sites with different energies and localization lengths, indicated by different lengths of lines and the schematic (colored) wave functions. Red and blue color gradients indicate the change of Fermi level and transport energy with charge density n (red arrow). The indicated regions I-III in panel **(d)** divide the graph into the respective regimes of linear, power-law, and saturation behavior of the conductivity. Adapted from my paper[94]. Licensed under CC BY 4.0 (https://creativecommons.org/licenses/by/4.0/).

In the next section, the Seebeck coefficient is studied. **Figure 44** shows the dependence of the Seebeck coefficient on the charge carrier concentration and on the conductivity.

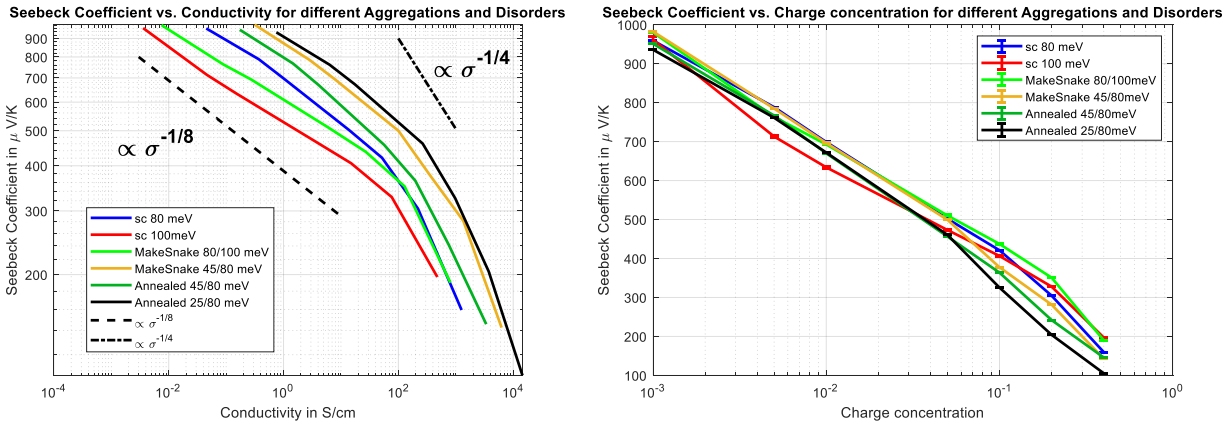

Figure 44 – Left: Seebeck coefficient as function of conductivity for different morphologies. The dotted lines are guides to the eye for the frequently observed inverse relation between Seebeck coefficient and conductivity. Right: Seebeck coefficient as function of charge carrier concentration for different morphologies.

The slope b of $\ln(S/S_0) = b \cdot \ln(\sigma)$ for lower charge carrier concentrations of all morphologies is similar, but with a different value of $-1/8$ than the experimentally often observed slope of $-1/4$. The reason for that is attributed to the form of the DOS, being a combination of gaussians. The slope of $-1/4$ is rather obtained from exponential tails in the DOS[95] that emerge due to doping in real systems. For the present simulations, no doping is considered though. This phenomenon has been observed in literature before[45].

All curves seem to be only shifted to each other according to their conductivity. From the right graph of Figure 44, one can also see that despite the significant differences in conductivity of the different morphologies, the Seebeck coefficient seems to be rather untouched. The differences between the curves of Seebeck coefficient plotted against the charge carrier concentration are only between $50\,\mu V/K$ and $100\,\mu V/K$. Previous studies like from Upadhyaya et al.[96] confirm this result. For an increasing localization length, the Seebeck coefficient therefore seems nearly untouched. The same holds for introduction of positional disorder or spatial or energetical correlations in the system. The largest but still limited effect, as can also be observed here, is the disorder of the system, where low disorders decrease the Seebeck coefficient a little bit. Thereby, the introduction of an energy dependent localization

lengths together with all the spatial and energetical correlations that are considered in the simulations of this thesis are not expected to have a large influence either. One reason for that is that the Fermi energy and transport energy are mostly influenced by the DOS and therefore by the disorder. The Seebeck coefficient is proportional to the difference of these energies. As can be seen in Figure 42, these energies move in accordance to each other for all morphologies such that their difference is largely constant, which means that the modulation of conductivity for different morphologies is to some extent decoupled from the corresponding Seebeck coefficient. This result links to the result of the first chapter, where an anisotropic localization length achieved by an increased edge-on face-on ratio could significantly increase the conductivity while letting the Seebeck coefficient considerably less affected by the morphological modification.

In the following section the corresponding results for the MD morphologies are presented.

Molecular Dynamics Morphologies

Figure 45 shows the charge carrier concentration dependence of the conductivity for the case of $f_{ich} = 1.3$.

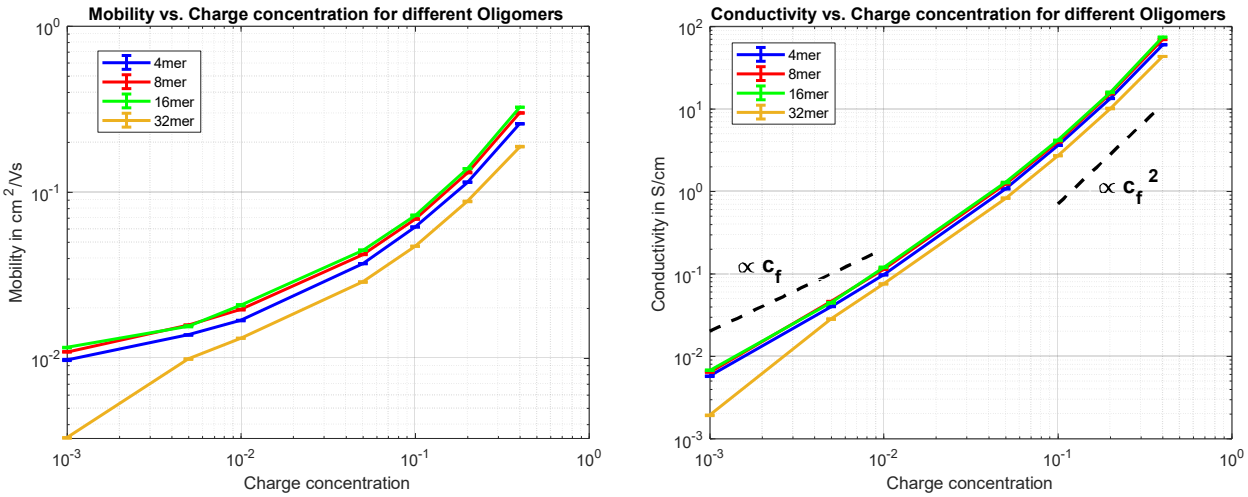

Figure 45 – Left: Mobility as function of charge carrier concentration of different oligomer morphologies in a double-log plot. Right: The same for conductivity.

The similarity of the curves for the different chain lengths and the deviation of 32mer was already addressed in the chapter about field-dependence. It should be noted that here the data point of 32mer for $c_f = 0.1\%$ is a numerical artefact and therefore be neglected. Again, a linear dependency of the charge carrier concentration at low concentrations is observed. At higher c_f, the curves are approximately quadratic with c_f. The flatter localization length distributions compared to the simplified model morphologies prevent an even higher slope in this case. The conductivities compare to experimentally observed values most realistically for $c_f = 0.1\%$ to lightly to medium doped P3HT, where values reach from $10^{-5}\, S/cm$ to $10^{-2}\, S/cm$ [97]. However, albeit the morphologies are obtained from MD simulations of P3HT, direct comparisons need to be treated with care, since the MD simulations are done for pristine, monodisperse and low molecular weight of only around $M_w = 3\ kDa$, i.e. small chain length rrP3HT. Compared to such low molecular weights, the obtained mobility is probably too high[98] such that e.g. the attempt-to-hop frequency and/or the transfer integral scaling factor needs to be chosen lower. Realistic P3HT is polydisperse with higher molecular weight[99], i.e. longer chain lengths and even the cleanest badges of rrP3HT contain a small fraction of regio-randomness. Besides that, both doping and deposition techniques have influence on the morphology, which in turn can have a significant influence on the conductivity. Also, the simulation approach here has tunable parameters like the scaling factor of the transfer integrals, the orbital parameters and the attempt-to-hop frequency in the kMC simulation. However, it would be possible to obtain a more material specific parametrization of those with ab-initio calculations as DFT.

From experiments[100] one would expect a difference in conductivity for different chain lengths of P3HT, what is however not significantly observed in Figure 45. This is mainly due to the comparatively low intra-chain coupling factor of $f_{ich} = 1.3$. Therefore, also simulations with an enhanced intra-chain coupling factor of $f_{ich} = 10$ were performed. The results are shown in **Figure 46**.

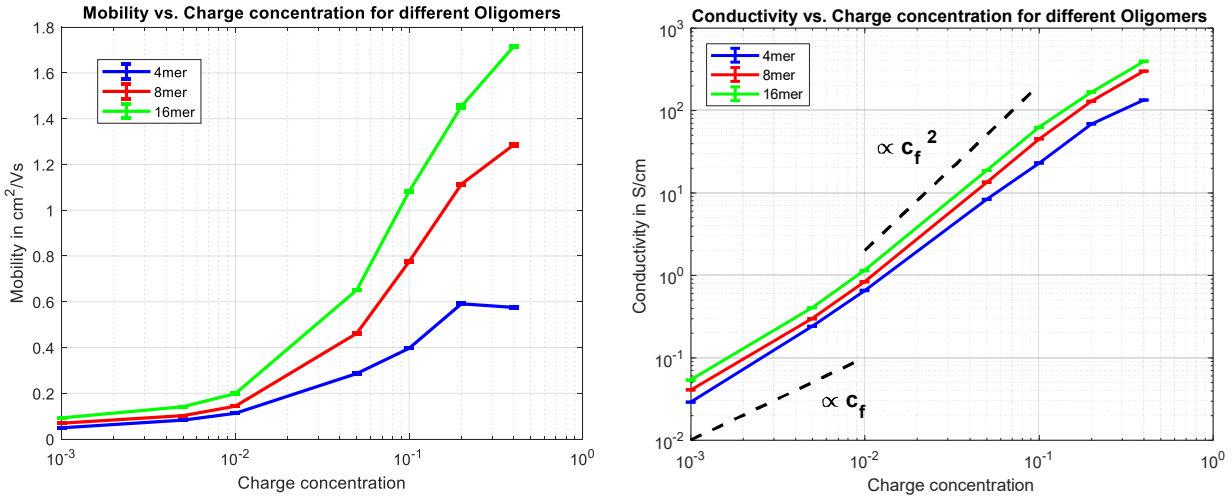

Figure 46 – Left: Mobility as function of charge carrier concentration of different oligomer morphologies for $f_{ich} = 10$ in a double-log plot. Right: The same for conductivity.

In this scenario the difference can be seen. Especially for charge carrier concentrations of $c_f > 1\%$, the mobility curves get steeper with increasing chain length. For lower charge carrier concentrations, the relative differences of the conductivity to the next higher chain length are $> 30\%$ with an increasing difference for higher charge carrier concentration. The slope of the conductivity curve at higher charge carrier concentrations however is reduced in comparison to the cases considered before. This is due to the more uniform localization length distribution of these morphologies obtained by the tight binding calculations. The overall magnitude of the conductivities increases approximately one order of magnitude compared to the $f_{ich} = 1.3$ case, highlighting the importance of intra-chain coupling for the conductivity.

In the following the Seebeck coefficient is investigated and compared to all other considered morphology cases. **Figure 47** shows the curves of Seebeck coefficient over the conductivity and the charge carrier concentration for the both cases of $f_{ich} = 1.3$ and 10.

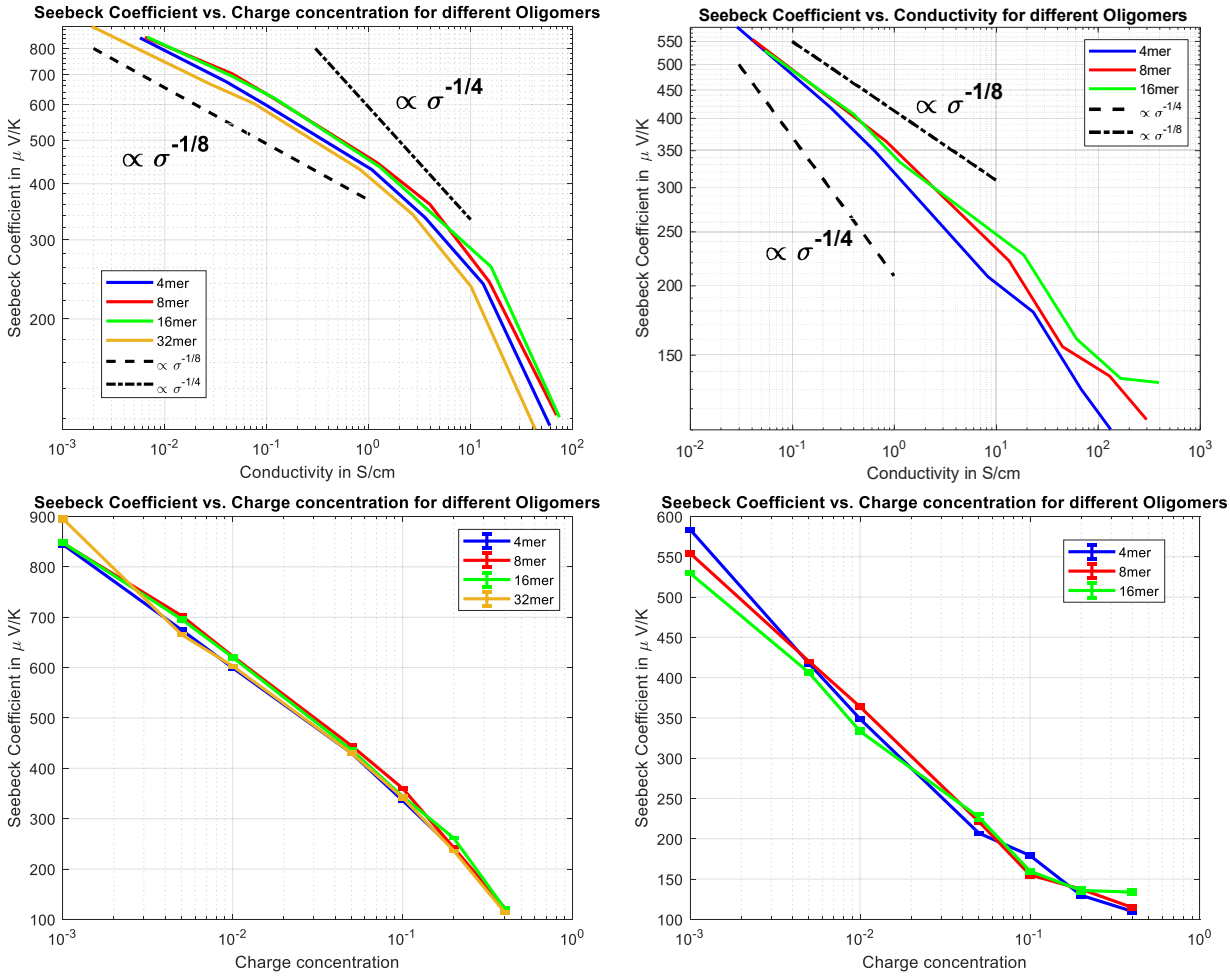

Figure 47 – Upper graphs: Seebeck coefficient as function of conductivity for the case $f_{ich} = 1.3$ (left) and $f_{ich} = 10$ (right). Lower graphs: Dependence of Seebeck coefficient on charge carrier concentration for $f_{ich} = 1.3$ (left) and $f_{ich} = 10$ (right).

For the case of $f_{ich} = 1.3$, the discussion is the same as for the model morphologies in the last section. One gets a relation of rather $S \propto \sigma^{-1/8}$ than $\propto \sigma^{-1/4}$ due to the gaussian DOS and a fall-off at around $300\ \mu V/K$. Interestingly, the fall-off is much less pronounced for the case of $f_{ich} = 10$, which may be due to the deep transport energy that did not saturate yet. Also, as expected from the conductivity as well, the dependency of the Seebeck coefficient on the charge carrier concentration is the same. However, in comparison to the simplified morphologies in the last section, the Seebeck coefficient for $f_{ich} = 1.3$ is around $100\ \mu V/K$ lower, especially the sc 80meV morphology with the same energetic disorder and DOS form. In the case of $f_{ich} = 10$ the effect is even higher, here the Seebeck coefficient reduces

drastically to only around $550\,\mu V/K$. From the higher disorder ($\approx 140\,meV$) one would rather expect a higher Seebeck coefficient. For the interested reader, the resulting influence on the powerfactors is shown in the SI. Also, the mean localization length is not considerably different from all the other cases. The only difference is the more delocalized lower energy states in the case of $f_{ich} = 10$. Looking at the transport energy of the oligomer morphologies, they interestingly lie significantly deeper than for comparable simplified morphological cases (around $-40\,meV$ for the oligomer morphologies with $f_{ich} = 1.3$ (cf. **Figure 48**) compared to around $0\,meV$ for the latter). This might be due to efficient/enhanced and lower energetic intra-chain transport for the MD morphologies compared to the other. This effect would be even more enhanced for the energetically high disordered case with an even stronger intra-chain coupling of $f_{ich} = 10$, possibly explaining the further decrease in Seebeck coefficient and would also explain the increase of conductivity over one order of magnitude despite the disorder. This is supported by the very deep transport energy in the case of $f_{ich} = 10$ in **Figure 48**.

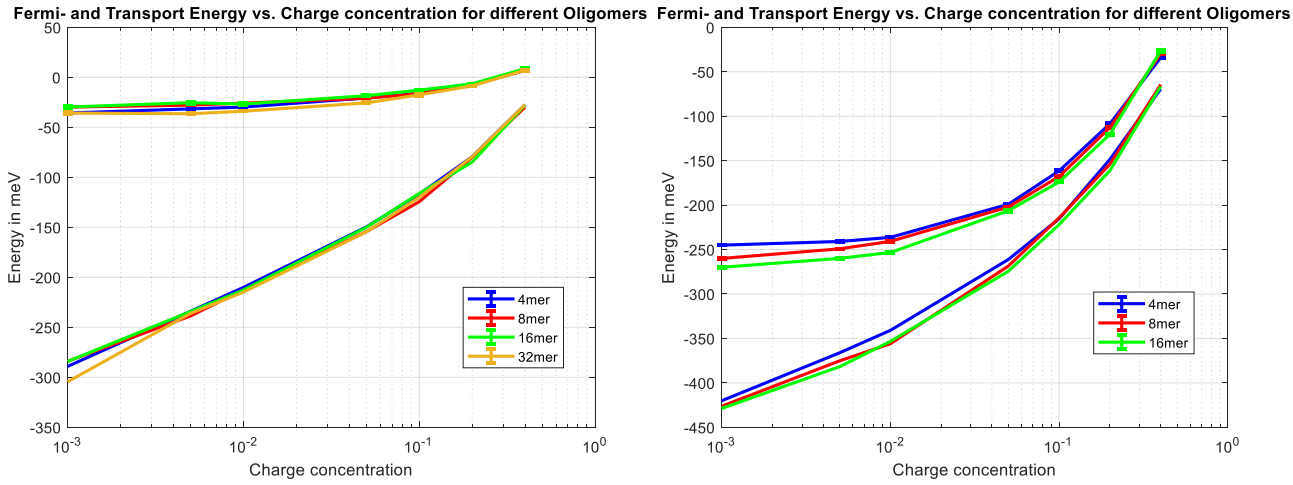

Figure 48 – Left: Transport energies (upper curves) and Fermi energies (lower curves) as function of charge carrier concentration for the case $f_{ich} = 1.3$. Right: The same for $f_{ich} = 10$.

To conclude this section, the superlinear increase in conductivity for high charge carrier concentrations could be reproduced. Different morphologies can have a huge impact in conductivity, while the Seebeck coefficient is often rather unaffected. However, a low-lying transport energy, like through efficient and highly coupled intra-chain transport in low energy states or generally a low energetic percolation/conduction path can significantly reduce the Seebeck coefficient. From a practical point of view, the effect on the powerfactor is however still dominated by the conductivity.

Density of States Renormalization for High Doping Concentrations

This chapter covers my contribution to the paper[101] about modelling of the DOS at low to intermediate doping concentrations. The following introduction summarizes the key aspects of the coworker's argumentation.

For designing thermoelectric devices, the aim is always to maximize the figure of merit $ZT = \frac{PF}{\kappa_{el}+\kappa_{lat}} = \frac{S^2\sigma}{\kappa_{el}+\kappa_{lat}}$ and therefore also the powerfactor PF. This is however a far from trivial task. As already outlined in the Theoretical Background, the well-known[81] trade-off between the Seebeck coefficient and the conductivity $S \propto \sigma^{-1/4}$ for single-material and low to intermediate doping concentrations prohibits the simultaneous increase of both parameters. This inverse relationship between Seebeck coefficient and conductivity is known to be explained and obtained by an ion-induced exponential tail in the DOS[95]. If this relationship would persist up to high doping, the powerfactor would scale as $PF \propto \sigma^{1/2}$, which would suggest as a clear design rule to maximize the conductivity. However, experimentally the inverse relationship only holds up to intermediate doping. Further increase of the doping concentration is observed to cause a roll-off in conductivity, which cannot be obtained with ion-induced exponential tails in the DOS. While one would in any case expect a maximum in conductivity at sufficiently high doping concentrations such that the Fermi level would reach the maximum of the DOS, experimentally one observes the roll-off of conductivity already at intermediate doping levels. Due to this roll-off, the Powerfactor already reaches its maximum at intermediate doping regimes, which lies around a doping level of $c_d = 10\%$ and found to define a soft upper limit of the Seebeck coefficient of around $200\ \mu V/K$, which is not obtained by the ion-induced exponential tail and no model is able to consistently cover the relevant doping regime where the Powerfactor is maximized. Using KMC simulations, the roll-off at these intermediate doping levels can only be explained when considering a gaussian DOS and free charge carriers, i.e. only carrier-carrier interaction.

To explain this, I performed TB calculations including the Coulomb potentials of counter ions. For the underlying lattice of these simulations a simple cubic lattice of size $20 \times 20 \times 20$ with a lattice spacing of $a_{NN} = 0.5\ nm$ and periodic boundary conditions was used. The orbital parameters of the site orbitals were chosen to be $(l_x, l_y, l_z) = (1,1,1) \cdot 0.1\ nm$ and the scaling factor of the transfer integrals was chosen to be $\nu_0 = 10^{14}\frac{1}{s}$ such that the next neighbor

transfer integrals are in the order of $10\ meV$. The on-site energies were drawn from a gaussian distribution of $50\ meV$ disorder. The cutoff distance for the Coulomb potentials of each ion were taken to be $2 \cdot a_{NN}$ to mimic a finite Coulomb potential depth of the ions. For each doping concentration c_d, on a fraction of $\lfloor N \cdot c_d \rfloor$ of all N lattice sites a single ion was placed, where the ion positions were randomly chosen from the available lattice sites. The calculations were then performed for five different doping concentrations. First, the dielectric constant was chosen to be $\epsilon_r = 3.6$ for all doping concentrations. The corresponding results for the resulting DOS and localization length distributions is shown in **Figure 49** and **50**.

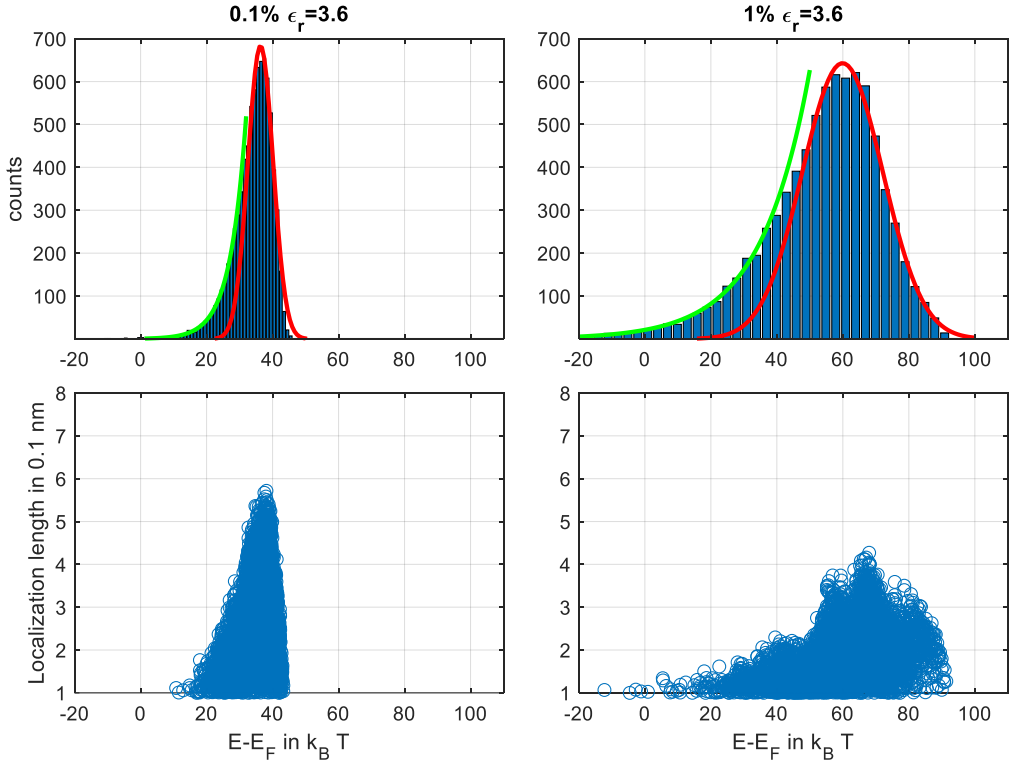

Figure 49 – Up: DOS for $c_d = 0.1\%$ and 1%. The red curves are fits to the gaussian part; the green curves are fits to the exponential part. Down: Corresponding localization length distributions.

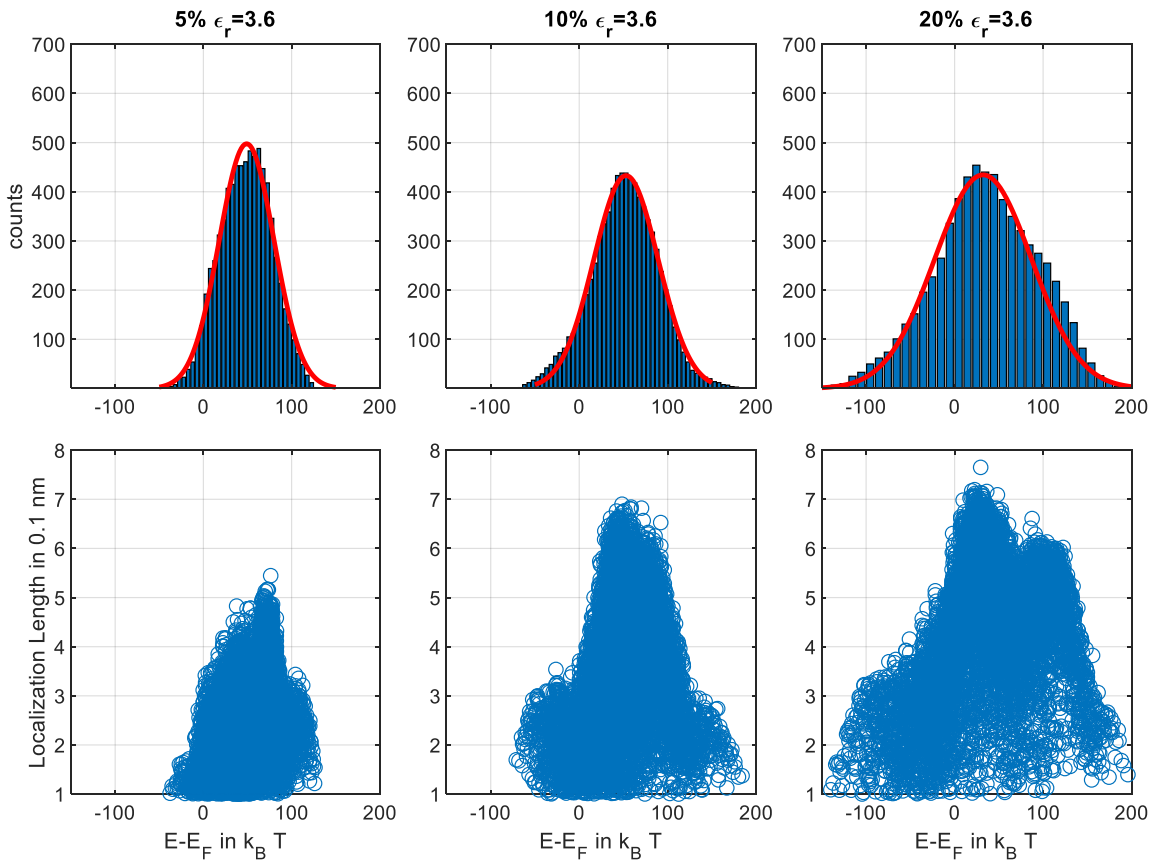

Figure 50 - Up: DOS for $c_d = 5\%,\ 10\%$ and 20%. The red curves are fits to the gaussian part. Down: Corresponding localization length distributions.

From both Figures 49 and 50 one can see that for lower doping concentrations of $c_d = 0.1\%$ and 1%, the well-established exponential is recovered. Further increasing the doping level to intermediate and higher doping levels of $c_d = 5\% - 20\%$, indeed the DOS renormalizes into a gaussian DOS again. In passing, it should be noted here that the x-scales of Figure 49 and 50 are different, which was necessary for visibility. This renormalization of the DOS can be explained by increasingly overlapping Coulomb potentials already from intermediate doping levels on, which leads to a flattening of the potential landscape formed by the overlapping Coulomb potentials of the ions. This is supported by the resulting localization length distributions. While for low doping levels, the Coulomb potentials act as traps, which introduces the low energy exponential tail, the charges get increasingly localized as seen from $c_d = 0.1\%$ and 1%. However, when the DOS renormalizes and the Coulomb potentials start to overlap and therefore flatten the potential landscape, the charges can become increasingly

delocalized as seen from the localization length distributions $c_d = 5\% - 20\%$. This further supports the claim of using free charge carrier at intermediate doping levels for kMC.

However, for constant dielectric constant of the host lattice of $\epsilon_r = 3.6$, the DOS get significantly broadened. The missing part here is that the enhanced polarizability of the lattice due to the introduction of counter ions was neglected. As outlined in the Theoretical Background, the introduction of counter ions into the lattice leads to an enhanced effective polarizability of the lattice, which in turn leads to increased screening and therefore an increased dielectric constant. To include this effect, a dynamic dielectric constant was introduced in the simulations. The chosen values of the dielectric constants for each doping level were approximated from the curve in Figure 1 in the Theoretical Background. The corresponding results of the thereby obtained DOS and localization length distributions are shown in **Figure 51** and **52**.

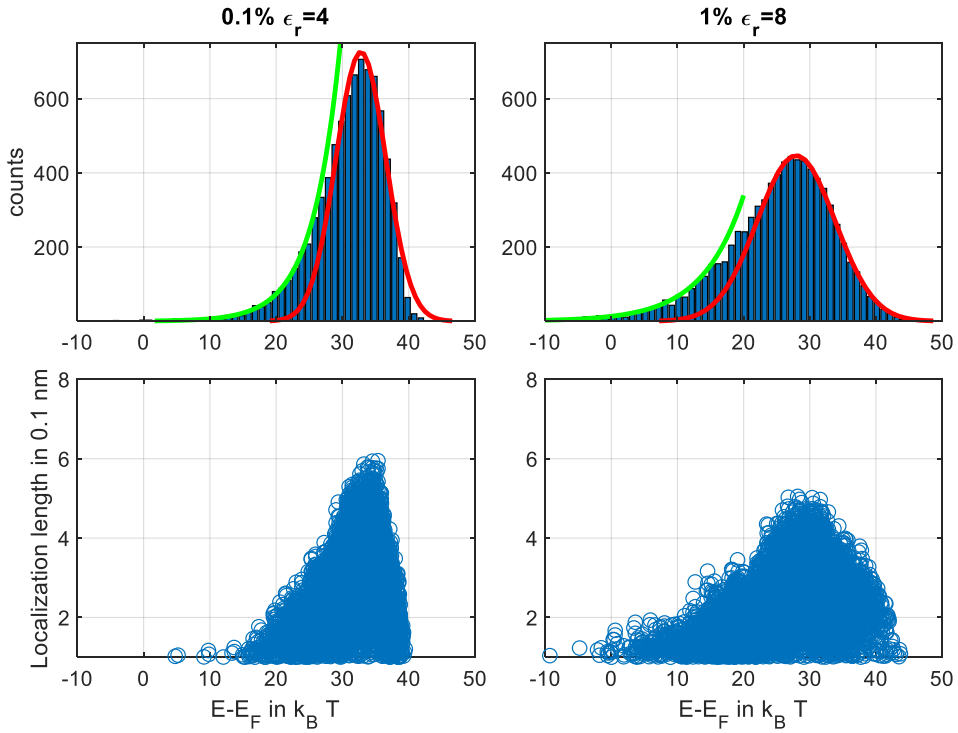

Figure 51 – Up: DOS for $c_d = 0.1\%$ and 1% for different dielectric constants. The red curves are fits to the gaussian part; the green curves are fits to the exponential part. Down: Corresponding localization length distributions.

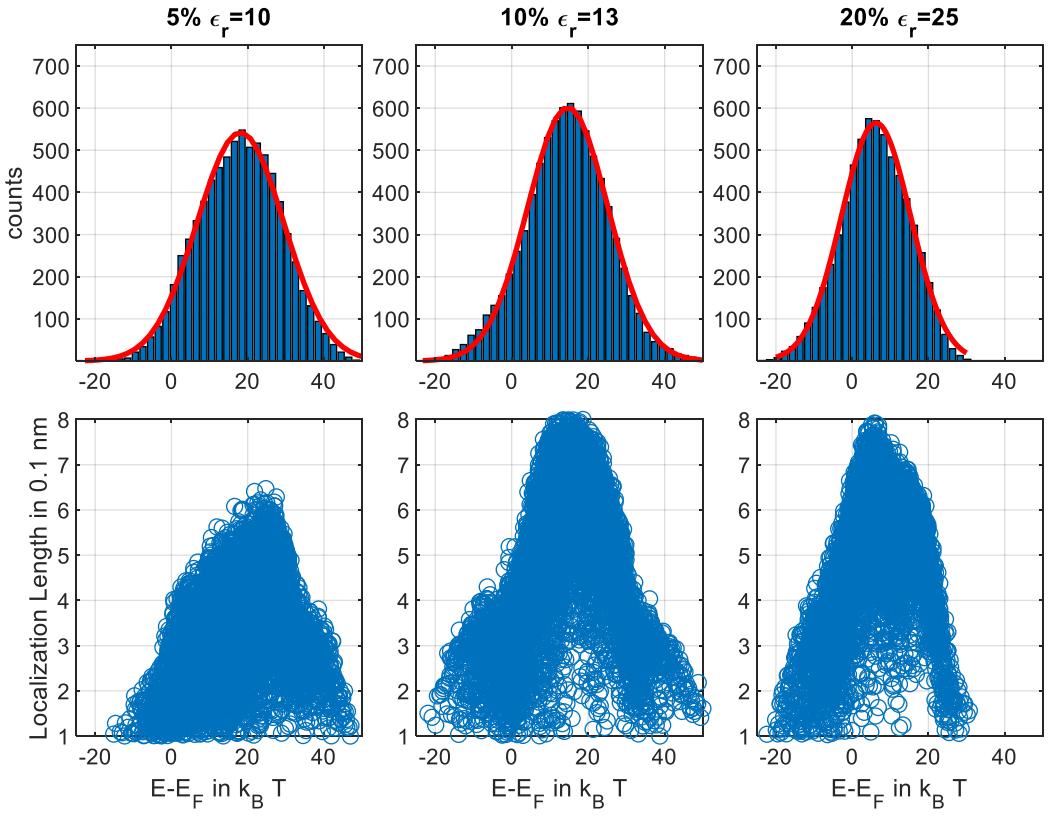

Figure 52 - Up: DOS for $c_d = 5\%,\ 10\%$ and 20% for different dielectric constants. The red curves are fits to the gaussian part. Down: Corresponding localization length distributions.

Indeed, the introduction of an increasing dielectric constant reduces the width of the DOS significantly. The introduction of increasing dielectric disorder also does not alter the qualitative behavior of the DOS, with exponential tails at low doping concentrations and renormalization of the DOS from intermediate doping concentrations on. Additionally, the increasing screening delocalizes the charges even further compared to the case of $\epsilon_r = 3.6$.

A comparison of the gaussian width of all considered cases is given in **Table 14**.

Table 14 – Fitted disorders in units of thermal energy (300 K) for constant and dynamic ϵ_r.

	$c_d = 0.1\%$ $\epsilon_r = 3.6$	$c_d = 1\%$ $\epsilon_r = 3.6$	$c_d = 5\%$ $\epsilon_r = 3.6$	$c_d = 10\%$ $\epsilon_r = 3.6$	$c_d = 20\%$ $\epsilon_r = 3.6$
σ_{DOS}/k_BT	3.8	12	31	36	54

	$c_d = 0.1\%$ $\epsilon_r = 4$	$c_d = 1\%$ $\epsilon_r = 8$	$c_d = 5\%$ $\epsilon_r = 10$	$c_d = 10\%$ $\epsilon_r = 13$	$c_d = 20\%$ $\epsilon_r = 25$
σ_{DOS}/k_BT	3.8	5.9	11	10	9

While the unscreened disorders get unphysically high, the disorders for increasing screening for increasing doping level remain limited around $10k_BT$ for the considered screenings at higher doping levels. This is however still broad, but is consistent with literature[69,102] that reports significant DOS broadening with increasing doping level.

To conclude this chapter, it should be noted that the DOS renormalization can only happen in regions in which the ions are distributed homogeneously as done here by introducing a sc lattice with one dopant per site only to ensure a spatially uniform overlapping of the Coulomb potentials with increasing doping level. If the ions are in any matter clustered or otherwise inhomogeneously distributed, the exponential tail should remain even up to high doping concentrations. It should also be mentioned that at even higher concentrations the introduced model loses validity since carrier-carrier interactions become more and more important but are not properly treated here for this high doping regime.

However, the here introduced model can both reproduce the necessary exponential tail in the DOS for low doping levels that lead to the power-law $S \propto \sigma^{-1/4}$ and explain the experimentally observed roll-off of the conductivity already at the relevant intermediate doping regime by the renormalization of the DOS into a gaussian distribution that is needed to describe the $S(\sigma)$ dependency in the relevant wide range of conductivity with kMC simulations.

Summary

In this dissertation I developed a semi-empirical tight binding model that uses model morphologies and morphologies obtained by Molecular Dynamics simulations as underlying lattice to perform kMC simulations with more realistic morphologies under the inclusion of both spatial and energetical correlations and partially delocalized charge carrier wavefunctions obtained from the tight binding calculations.

The developed model was used in combination or separately to answer different questions that were covered in the different chapters.

In the first chapter a physical explanation was given to the experimentally found significant increase in the in-plane powerfactor of thin films with a high edge-on to face-on ratio that breaks the usually observed inverse relationship between the Seebeck coefficient and the conductivity.

It was found that an increased edge-on to face-on ratio can lead to an effective delocalization of the charge carrier wavefunctions in the in-plane direction due to $\pi - \pi$ –stacking of polymer faces. This in turn leads to an anisotropic effective localization length, which leads to an increased conductivity in the in-plane direction due to enhanced tunneling rates and due to the resulting conduction path being more direct than in the isotropic case. This however does not alter the Seebeck coefficient significantly. In fact, it is even slightly increased. This was explained by occasionally higher jumps in the energy landscape induced from the more direct conduction path, while in the isotropic case the conduction path is more optimized in the energy landscape. Therefore, in the anisotropic case the transport energy is slightly increased compared to the isotropic case, which in turn leads to an increased Seebeck coefficient.

The second chapter investigates the validity of the effective temperature approach for the field dependence of the conductivity of OSCs. The question was motivated by measurements that show an increased field dependence of the conductivity already at lower fields, which would lead to an untypically high localization length using the effective temperature approach.

Hereby, different morphologies were considered reaching from homogeneous systems up to increasingly aggregated systems and filament like morphologies for polymers obtained from Molecular Dynamics simulations. For all morphologies, the actual heating of the charge carrier

distribution obtained from the DOOS and the effective temperature models that replace the temperature dependence of the ohmic conductivity with the effective temperature were compared to an experimental approach to obtain the effective temperature and thereby the localization length from temperature dependence measurements of the ohmic conductivity and field dependence measurements of the conductivity. It was found that with increasing inhomogeneities of the morphology the deviations between the models and the input localization length distributions also increase. But not only the morphology seems to have an impact on the field-dependence beyond the effective temperature effect, also disorder and possibly other parameters like delocalization of charge carriers due to the field dependence of the transport energy could have an influence on the field-dependence that is not captured in the effective temperature model. These discrepancies can lead to a misinterpretation of experimentally obtained localization lengths since all the hidden influences on the field dependence get reflected in unphysical changes in the localization length. However, to what extent what physical parameters influence the field dependence additionally could not safely be explained due to the intercorrelations of different parameters in this model that prohibit the investigation of independent changes of single parameters in the model and therefore remain an open question for future research.

In the next chapter, the experimentally observed superlinear increase of conductivity with charge carrier concentration at high charge carrier concentrations was numerically explained and recovered for different morphological set ups.

The introduction of energy dependent localization lengths from the tight binding model leads to a peaked distribution of localization lengths that is similar to the DOS. While the transport energy remains close to the DOS center, the Fermi energy rises with increasing charge carrier concentration until it reaches an energetic level at which the charges start to partially delocalize. This increase in delocalization for increasing Fermi energies lead to an additional contribution in the rising of the conductivity curve and can therefore explain the super-linear increase in conductivity.

As last point it was discussed why the experimentally observed roll-off in conductivity in the typically observed $S(\sigma)$ curves for OSCs can only be explained in a kMC model if one assumes a gaussian DOS and free charge carriers at intermediate doping levels, which is the relevant regime for optimized thermoelectric devices, while for lower doping levels ion-induced

exponential tails in the DOS are formed that are responsible for the typical inverse power-law dependence of the Seebeck coefficient and the conductivity. To answer this question, the tight binding model developed in this thesis was used including Coulomb interaction between charge carriers and ions for different doping concentrations. For low doping levels the well-established exponential tail in the DOS was reproduced. However, further increasing doping levels up to intermediate doping levels was found to renormalize the DOS back to a gaussian DOS for uniformly distributed ions. This was explained by an increasing overlap of the Coulomb potentials of the dopant ions that increasingly flatten the energetic landscape already at intermediate doping levels. This is supported by an onset of delocalization accompanied by the DOS renormalization, while for lower concentrations rather a localization due to the deep traps induced by the exponential tails takes place.

Outlook

While the developed model can give a nice bridge between computationally very expensive ab-initio calculations and simple and fast kMC models, the tight binding parametrization can still be improved under the inclusion of ab-initio calculations like DFT. While the model explicitly allows for more material specific parametrization like explicit HOMO or LUMO orbitals of monomers, here I was limited to approximations. Additionally, the localized character of OSCs allows for faster and computationally faster diagonalization for even larger systems by diagonalizing overlapping subspaces as sometimes proposed in literature. Also, the localization length obtained from the tight binding model and the IPR gives rise to only isotropic delocalization. An interesting add-on would be the treatment of anisotropic localization lengths from the model, which was technically already largely implemented by myself, but not applied in the set-up of this thesis.

From a physical point of view, especially the field dependence of OSCs remains an open question. Future research could try to disentangle the influences of parameters that could only be discussed qualitatively here to obtain a deeper understanding on the still in detail illusive field dependence of OSCs.

Acknowledgements

I wish to thank Paolo Floris for the provided Molecular Dynamics calculations and for the great collaboration. Another special thanks go to Riccardo Rurali for giving me the opportunity to conduct my research and collaborate with him and Paolo at ICMAB in Barcelona and being such a nice host. I would like to thank the state of Baden-Württemberg for the support of the bwHPC and the German Research Foundation (DFG) for funding under the reference “INST 39/1232-1 FUGG” (bwForCluster NEMO 2). I thank for the provided computational resources and their assistance. I also want to thank all my colleagues and collaborators for the fruitful scientific collaborations and discussions. And of course, big thanks to Martijn Kemerink for the nice supervision and support during my time as PhD.

List of Publications

Derewjanko, D. *et al.* Delocalization Enhances Conductivity at High Doping Concentrations. *Adv. Funct. Mater.* **32**, 2112262 (2022). (Published during Master, numerically reproduced and generalized in this dissertation in the chapter 'Charge Carrier Concentration Dependence')

Rosas Villalva, D. *et al.* Intermolecular-force-driven anisotropy breaks the thermoelectric trade-off in n-type conjugated polymers. *Nat. Mater.* (2025) doi:10.1038/s41563-025-02207-9. (Chapter 'Power Factor Optimization for Anisotropic Localization Properties')

Li, Z. *et al.* A Universal Soft Upper Limit to the Seebeck Coefficient in Organic Thermoelectrics. Preprint at https://doi.org/10.2139/ssrn.5147905 (2025) (Chapter 'Density of States Renormalization for High Doping Concentrations')

Morteza Shokrani, Felix Maximilian Graf, Anton Kompatscher, Dennis Derewjanko, Martijn Kemerink, *Manuscript in preparation.* (2025) (Partly in the chapter 'Field Dependence Simulations' and in chapter 'Field Dependent Localization' in the SI)

References

1. Akamatu, H. & Inokuchi, H. On the Electrical Conductivity of Violanthrone, Iso-Violanthrone, and Pyranthrone. *J. Chem. Phys.* **18**, 810–811 (1950).
2. Mott, N. F. Conduction in non-crystalline materials: III. Localized states in a pseudogap and near extremities of conduction and valence bands. *Philos. Mag.* **19**, 835–852 (1969).
3. Mott, N. F. Conduction in glasses containing transition metal ions. *J. Non-Cryst. Solids* **1**, 1–17 (1968).
4. Miller, A. & Abrahams, E. Impurity Conduction at Low Concentrations. *Phys. Rev.* **120**, 745–755 (1960).
5. Marcus, R. A. On the Theory of Oxidation-Reduction Reactions Involving Electron Transfer. I. *J. Chem. Phys.* **24**, 966–978 (1956).
6. Bässler, H. Charge Transport in Disordered Organic Photoconductors a Monte Carlo Simulation Study. *Phys. Status Solidi B* **175**, 15–56 (1993).
7. Lukyanov, A. & Andrienko, D. Extracting nondispersive charge carrier mobilities of organic semiconductors from simulations of small systems. *Phys. Rev. B* **82**, 193202 (2010).
8. Padula, D., Barneschi, L. & Landi, A. Multiscale Modeling of Charge Transport in Organic Semiconductors: Assessing the Validity of the Harmonic Approximation for Low-Frequency Vibrations. *J. Phys. Chem. C* **129**, 784–792 (2025).
9. Schrader, M. *et al.* Comparative Study of Microscopic Charge Dynamics in Crystalline Acceptor-Substituted Oligothiophenes. *J. Am. Chem. Soc.* **134**, 6052–6056 (2012).
10. Rühle, V. *et al.* Microscopic Simulations of Charge Transport in Disordered Organic Semiconductors. *J. Chem. Theory Comput.* **7**, 3335–3345 (2011).
11. Rühle, V., Junghans, C., Lukyanov, A., Kremer, K. & Andrienko, D. Versatile Object-Oriented Toolkit for Coarse-Graining Applications. *J. Chem. Theory Comput.* **5**, 3211–3223 (2009).
12. Rühle, V., Kirkpatrick, J. & Andrienko, D. A multiscale description of charge transport in conjugated oligomers. *J. Chem. Phys.* **132**, 134103 (2010).

13. Mladenović, M. & Vukmirović, N. Charge Carrier Localization and Transport in Organic Semiconductors: Insights from Atomistic Multiscale Simulations. *Adv. Funct. Mater.* **25**, 1915–1932 (2015).

14. Vukmirović, N. & Wang, L.-W. Overlapping fragments method for electronic structure calculation of large systems. *J. Chem. Phys.* **134**, 094119 (2011).

15. Miller, E. D., Jones, M. L. & Jankowski, E. Tying Together Multiscale Calculations for Charge Transport in P3HT: Structural Descriptors, Morphology, and Tie-Chains. *Polymers* **10**, 1358 (2018).

16. Zerner, M. C., Loew, G. H., Kirchner, R. F. & Mueller-Westerhoff, U. T. An intermediate neglect of differential overlap technique for spectroscopy of transition-metal complexes. Ferrocene. *J. Am. Chem. Soc.* **102**, 589–599 (1980).

17. Alkan, M. & Yavuz, I. Intrinsic charge-mobility in benzothieno[3,2- *b*][1]benzothiophene (BTBT) organic semiconductors is enhanced with long alkyl side-chains. *Phys. Chem. Chem. Phys.* **20**, 15970–15979 (2018).

18. Park, J. W. *et al.* The prediction of hole mobility in organic semiconductors and its calibration based on the grain-boundary effect. *Phys. Chem. Chem. Phys.* **18**, 21371–21380 (2016).

19. Deniz Özdemir, A. *et al.* Dynamic Effects on Hole Transport in Amorphous Organic Semiconductors: a Combined QM/MM and kMC Study. *J. Chem. Theory Comput.* **19**, 3849–3860 (2023).

20. Gajdos, F. *et al.* Ultrafast Estimation of Electronic Couplings for Electron Transfer between π-Conjugated Organic Molecules. *J. Chem. Theory Comput.* **10**, 4653–4660 (2014).

21. Gajdos, F. Electronic Coupling Calculations for modelling charge transport in organic semiconductors. (University College London, 2016).

22. Tan, T., Duan, L. & Wang, D. Elucidating Morphology-Mobility Relationships of Organic Thin Films Through Transfer Learning-Assisted Multiscale Simulation. *Adv. Funct. Mater.* **34**, 2313085 (2024).

23. Zheng, X. *et al.* Understanding Lattice Strain-Controlled Charge Transport in Organic Semiconductors: A Computational Study. *Adv. Funct. Mater.* **24**, 5531–5540 (2014).

24. Miller, E. D., Jones, M. L. & Jankowski, E. Tying Together Multiscale Calculations for Charge Transport in P3HT: Structural Descriptors, Morphology, and Tie-Chains. *Polymers* **10**, 1358 (2018).

25. Sanderson, S. *et al.* Understanding the performance differences between solution and vacuum deposited OLEDs: A computational approach. *J. Chem. Phys.* **156**, 214703 (2022).

26. Segatta, F., Lattanzi, G. & Faccioli, P. Predicting Charge Mobility of Organic Semiconductors with Complex Morphology. *Macromolecules* **51**, 9060–9068 (2018).

27. Balzer, D., Smolders, T. J. A. M., Blyth, D., Hood, S. N. & Kassal, I. Delocalised kinetic Monte Carlo for simulating delocalisation-enhanced charge and exciton transport in disordered materials. *Chem. Sci.* **12**, 2276–2285 (2021).

28. Willson, J. T., Liu, W., Balzer, D. & Kassal, I. Jumping kinetic Monte Carlo: Fast and accurate simulations of partially delocalised charge transport in organic semiconductors. (2022) doi:10.48550/ARXIV.2211.16165.

29. Giannini, S. *et al.* Transiently delocalized states enhance hole mobility in organic molecular semiconductors. *Nat. Mater.* **22**, 1361–1369 (2023).

30. Spencer, J., Gajdos, F. & Blumberger, J. FOB-SH: Fragment orbital-based surface hopping for charge carrier transport in organic and biological molecules and materials. *J. Chem. Phys.* **145**, 064102 (2016).

31. Ishii, H., Inoue, J., Kobayashi, N. & Hirose, K. Quantitative mobility evaluation of organic semiconductors using quantum dynamics based on density functional theory. *Phys. Rev. B* **98**, 235422 (2018).

32. Ishii, H. *et al.* Charge mobility calculation of organic semiconductors without use of experimental single-crystal data. *Sci. Rep.* **10**, 2524 (2020).

33. Zozoulenko, I. *et al.* Electronic, Optical, Morphological, Transport, and Electrochemical Properties of PEDOT: A Theoretical Perspective. *Macromolecules* **54**, 5915–5934 (2021).

34. Rolland, N., Franco-Gonzalez, J. F., Volpi, R., Linares, M. & Zozoulenko, I. V. Understanding morphology-mobility dependence in PEDOT:Tos. *Phys. Rev. Mater.* **2**, (2018).

35. Elsner, J. *et al.* Thermoelectric transport in molecular crystals driven by gradients of thermal electronic disorder. *Sci. Adv.* **10**, (2024).

36. Forrest, S. R. *Organic Electronics: Foundations to Applications*. (Oxford University PressOxford, 2020). doi:10.1093/oso/9780198529729.001.0001.

37. Fließbach, T. *Elektrodynamik: Lehrbuch zur Theoretischen Physik II*. (Springer Berlin Heidelberg, Berlin, Heidelberg, 2022). doi:10.1007/978-3-662-64889-6.

38. Hunklinger, S. *Festkörperphysik*. (De Gruyter, Berlin Boston, 2018). doi:10.1515/9783110567755.

39. Warren, R., Blom, P. W. M. & Koch, N. Molecular *p* -doping induced dielectric constant increase of polythiophene films determined by impedance spectroscopy. *Appl. Phys. Lett.* **122**, 152108 (2023).

40. Yang, X., Liu, J. & Koster, L. J. A. The Exceptionally High Dielectric Constant of Doped Organic Semiconductors. *Adv. Electron. Mater.* **11**, 2400413 (2025).

41. Comin, M., Fratini, S., Blase, X. & D'Avino, G. Doping-Induced Dielectric Catastrophe Prompts Free-Carrier Release in Organic Semiconductors. *Adv. Mater.* **34**, 2105376 (2022).

42. Atahan-Evrenk, Ş. & Aspuru-Guzik, A. Prediction and Theoretical Characterization of p-Type Organic Semiconductor Crystals for Field-Effect Transistor Applications. in *Prediction and Calculation of Crystal Structures* (eds Atahan-Evrenk, S. & Aspuru-Guzik, A.) vol. 345 95–138 (Springer International Publishing, Cham, 2014).

43. Chew, A. R., Ghosh, R., Shang, Z., Spano, F. C. & Salleo, A. Sequential Doping Reveals the Importance of Amorphous Chain Rigidity in Charge Transport of Semi-Crystalline Polymers. *J. Phys. Chem. Lett.* **8**, 4974–4980 (2017).

44. Jacobs, I. E. *et al.* Comparison of solution-mixed and sequentially processed P3HT:F4TCNQ films: effect of doping-induced aggregation on film morphology. *J Mater Chem C* **4**, 3454–3466 (2016).

45. Scheunemann, D. *et al.* Rubbing and Drawing: Generic Ways to Improve the Thermoelectric Power Factor of Organic Semiconductors? *Adv. Electron. Mater.* **6**, (2020).

46. Rosas Villalva, D. *et al.* Intermolecular-force-driven anisotropy breaks the thermoelectric trade-off in n-type conjugated polymers. *Nat. Mater.* (2025) doi:10.1038/s41563-025-02207-9.

47. Hansen, C. M. The Three Dimensional Solubility Parameter and Solvent Diffusion Coefficient: Their Importance in Surface Coating Formulation. (Technical University of Denmark, Copenhagen, Denmark, 1967).

48. Hansen, C. M. *Hansen Solubility Parameters: A User's Handbook*. (CRC Press, Boca Raton, 2007).

49. Floris, P. S., Melis, C. & Rurali, R. Interplay Between Doping, Morphology, and Lattice Thermal Conductivity in PEDOT:PSS. *Adv. Funct. Mater.* **33**, 2215125 (2023).

50. Jorgensen, W. L., Madura, J. D. & Swenson, C. J. Optimized intermolecular potential functions for liquid hydrocarbons. *J. Am. Chem. Soc.* **106**, 6638–6646 (1984).

51. Lampin, E., Palla, P. L., Francioso, P.-A. & Cleri, F. Thermal conductivity from approach-to-equilibrium molecular dynamics. *J. Appl. Phys.* **114**, 033525 (2013).

52. Hoover, W. G. Canonical dynamics: Equilibrium phase-space distributions. *Phys. Rev. A* **31**, 1695–1697 (1985).

53. Peumans, P., Uchida, S. & Forrest, S. R. Efficient bulk heterojunction photovoltaic cells using small-molecular-weight organic thin films. *Nature* **425**, 158–162 (2003).

54. Flory, P. J. Molecular Size Distribution in Linear Condensation Polymers[1]. *J. Am. Chem. Soc.* **58**, 1877–1885 (1936).

55. Derewjanko, D. Charge Transport and Localization in Organic Semiconductors. (2022).

56. Altland, A. & Simons, B. *Condensed Matter Field Theory*. (Cambridge University Press, Leiden, 2010).

57. Haverkort, M. W. Condensed Matter Theory. (2020).

58. De Andrade, P. C. P. & Freire, J. A. Effective Hamiltonians for the nonorthogonal basis set. *J. Chem. Phys.* **118**, 6733–6740 (2003).

59. Coropceanu, V. *et al.* Charge Transport in Organic Semiconductors. *Chem. Rev.* **107**, 926–952 (2007).

60. Bässler, H. & Köhler, A. Charge Transport in Organic Semiconductors. in *Unimolecular and Supramolecular Electronics I* (ed. Metzger, R. M.) vol. 312 1–65 (Springer Berlin Heidelberg, Berlin, Heidelberg, 2011).

61. Xu, K. *et al.* Ground-state electron transfer in all-polymer donor–acceptor heterojunctions. *Nat. Mater.* **19**, 738–744 (2020).

62. Hughes, M. P. *et al.* Charge Recombination Dynamics in Organic Photovoltaic Systems with Enhanced Dielectric Constant. *Adv. Funct. Mater.* **29**, 1901269 (2019).

63. Brebels, J., Manca, J. V., Lutsen, L., Vanderzande, D. & Maes, W. High dielectric constant conjugated materials for organic photovoltaics. *J. Mater. Chem. A* **5**, 24037–24050 (2017).

64. Kirkpatrick, J. An approximate method for calculating transfer integrals based on the ZINDO Hamiltonian. *Int. J. Quantum Chem.* **108**, 51–56 (2008).

65. Kubas, A. *et al.* Electronic couplings for molecular charge transfer: benchmarking CDFT, FODFT and FODFTB against high-level ab initio calculations. II. *Phys. Chem. Chem. Phys.* **17**, 14342–14354 (2015).

66. Gali, S. M. *et al.* Energetic fluctuations in amorphous semiconducting polymers: Impact on charge-carrier mobility. *J. Chem. Phys.* **147**, 134904 (2017).

67. Baranovskii, S. D. Theoretical description of charge transport in disordered organic semiconductors. *Phys. Status Solidi B* **251**, 487–525 (2014).

68. Arkhipov, V. I., Heremans, P., Emelianova, E. V. & Bässler, H. Effect of doping on the density-of-states distribution and carrier hopping in disordered organic semiconductors. *Phys. Rev. B* **71**, 045214 (2005).

69. Zuo, G., Abdalla, H. & Kemerink, M. Impact of doping on the density of states and the mobility in organic semiconductors. *Phys. Rev. B* **93**, 235203 (2016).

70. Upadhyaya, M. *et al.* Raising Dielectric Permittivity Mitigates Dopant-Induced Disorder in Conjugated Polymers. *Adv. Sci.* **8**, 2101087 (2021).

71. Moix, J. M., Khasin, M. & Cao, J. Coherent quantum transport in disordered systems: I. The influence of dephasing on the transport properties and absorption spectra on one-dimensional systems. *New J. Phys.* **15**, 085010 (2013).

72. Anderson, P. W. Absence of Diffusion in Certain Random Lattices. *Phys. Rev.* **109**, 1492–1505 (1958).

73. Abrahams, E., Anderson, P. W., Licciardello, D. C. & Ramakrishnan, T. V. Scaling Theory of Localization: Absence of Quantum Diffusion in Two Dimensions. *Phys. Rev. Lett.* **42**, 673–676 (1979).

74. Zade, S. S. & Bendikov, M. Cyclic Oligothiophenes: Novel Organic Materials and Models for Polythiophene. A Theoretical Study. *J. Org. Chem.* **71**, 2972–2981 (2006).

75. Meisel, K. D., Vocks, H. & Bobbert, P. A. Polarons in semiconducting polymers: Study within an extended Holstein model. *Phys. Rev. B* **71**, 205206 (2005).

76. Cuppen, H. M., Karssemeijer, L. J. & Lamberts, T. The Kinetic Monte Carlo Method as a Way To Solve the Master Equation for Interstellar Grain Chemistry. *Chem. Rev.* **113**, 8840–8871 (2013).

77. Coehoorn, R., Pasveer, W. F., Bobbert, P. A. & Michels, M. A. J. Charge-carrier concentration dependence of the hopping mobility in organic materials with Gaussian disorder. *Phys. Rev. B* **72**, 155206 (2005).

78. Martens, H. C. F. *et al.* Understanding the doping dependence of the conductivity of conjugated polymers: Dominant role of the increasing density of states and growing delocalization. *Phys. Rev. B* **67**, 121203 (2003).

79. Baranovskii, S. D., Cordes, H., Hensel, F. & Leising, G. Charge-carrier transport in disordered organic solids. *Phys. Rev. B* **62**, 7934–7938 (2000).

80. Wang, Y. *et al.* First-principles thermodynamic theory of Seebeck coefficients. *Phys. Rev. B* **98**, 224101 (2018).

81. Glaudell, A. M., Cochran, J. E., Patel, S. N. & Chabinyc, M. L. Impact of the Doping Method on Conductivity and Thermopower in Semiconducting Polythiophenes. *Adv. Energy Mater.* **5**, 1401072 (2015).

82. Frenkel, J. On Pre-Breakdown Phenomena in Insulators and Electronic Semi-Conductors. *Phys. Rev.* **54**, 647–648 (1938).

83. Gartstein, Yu. N. & Conwell, E. M. High-field hopping mobility in molecular systems with spatially correlated energetic disorder. *Chem. Phys. Lett.* **245**, 351–358 (1995).

84. Pasveer, W. F. *et al.* Unified Description of Charge-Carrier Mobilities in Disordered Semiconducting Polymers. *Phys. Rev. Lett.* **94**, 206601 (2005).

85. Nenashev, A. V., Oelerich, J. O., Dvurechenskii, A. V., Gebhard, F. & Baranovskii, S. D. Fundamental characteristic length scale for the field dependence of hopping charge transport in disordered organic semiconductors. *Phys. Rev. B* **96**, 035204 (2017).

86. Marianer, S. & Shklovskii, B. I. Effective temperature of hopping electrons in a strong electric field. *Phys. Rev. B* **46**, 13100–13103 (1992).

87. Abdalla, H., Van De Ruit, K. & Kemerink, M. Effective Temperature and Universal Conductivity Scaling in Organic Semiconductors. *Sci. Rep.* **5**, 16870 (2015).

88. Jansson, F., Baranovskii, S. D., Gebhard, F. & Österbacka, R. Effective temperature for hopping transport in a Gaussian density of states. *Phys. Rev. B* **77**, 195211 (2008).

89. Tsoi, W. C. *et al.* Effect of Crystallization on the Electronic Energy Levels and Thin Film Morphology of P3HT:PCBM Blends. *Macromolecules* **44**, 2944–2952 (2011).

90. Dash, A. *et al.* Spontaneous Modulation Doping in Semi-Crystalline Conjugated Polymers Leads to High Conductivity at Low Doping Concentration. *Adv. Mater.* **36**, 2311303 (2024).

91. Oelerich, J. O., Nenashev, A. V., Dvurechenskii, A. V., Gebhard, F. & Baranovskii, S. D. Field dependence of hopping mobility: Lattice models against spatial disorder. *Phys. Rev. B* **96**, (2017).

92. Conchuir, B. O., Tarantini, C., McNeill, C. R., Hüttner, S. & Zaccone, A. Chain-Assisted Charge Transport in Semicrystalline Conjugated Polymers. *J. Phys. Chem. C* **120**, 14539–14548 (2016).

93. Nardes, A. M., Kemerink, M. & Janssen, R. A. J. Anisotropic hopping conduction in spin-coated PEDOT:PSS thin films. *Phys. Rev. B* **76**, 085208 (2007).

94. Derewjanko, D. *et al.* Delocalization Enhances Conductivity at High Doping Concentrations. *Adv. Funct. Mater.* **32**, 2112262 (2022).

95. Boyle, C. J. *et al.* Tuning charge transport dynamics via clustering of doping in organic semiconductor thin films. *Nat. Commun.* **10**, 2827 (2019).

96. Upadhyaya, M., Boyle, C. J., Venkataraman, D. & Aksamija, Z. Effects of Disorder on Thermoelectric Properties of Semiconducting Polymers. *Sci. Rep.* **9**, 5820 (2019).

97. Hynynen, J., Kiefer, D. & Müller, C. Influence of crystallinity on the thermoelectric power factor of P3HT vapour-doped with F4TCNQ. *RSC Adv.* **8**, 1593–1599 (2018).

98. Joshi, S. *et al.* Thickness Dependence of the Crystalline Structure and Hole Mobility in Thin Films of Low Molecular Weight Poly(3-hexylthiophene). *Macromolecules* **41**, 6800–6808 (2008).

99. Pouliot, J., Wakioka, M., Ozawa, F., Li, Y. & Leclerc, M. Structural Analysis of Poly(3-hexylthiophene) Prepared via Direct Heteroarylation Polymerization. *Macromol. Chem. Phys.* **217**, 1493–1500 (2016).

100. Dixon, A. G. *et al.* Molecular weight dependence of carrier mobility and recombination rate in neat P3HT films. *J. Polym. Sci. Part B Polym. Phys.* **56**, 31–35 (2018).

101. Li, Z. *et al.* A Universal Soft Upper Limit to the Seebeck Coefficient in Organic Thermoelectrics. Preprint at https://doi.org/10.2139/ssrn.5147905 (2025).

102. Hase, H., Berteau-Rainville, M., Charoughchi, S., Orgiu, E. & Salzmann, I. Doping-related broadening of the density of states governs integer-charge transfer in P3HT. *Appl. Phys. Lett.* **118**, 203301 (2021).

103. Theodorou, D. N. & Suter, U. W. Shape of unperturbed linear polymers: polypropylene. *Macromolecules* **18**, 1206–1214 (1985).

104. Mattice, W. L. & Suter, U. *Conformational Theory of Large Molecules: The Rotational Isomeric State Model in Macromolecular Systems*. (Wiley, New York, 1994).

Supporting Information

Field Dependent Localization

Besides Anderson localization, there can be another localizing effect, namely Stark localization, which is a localization effect induced by an electric field. One can intuitively understand this as follows. In a regular lattice without disorder one can think of Blochwaves at zero field. Introducing an electric field induces a phase shift of the sites wavefunction proportional to its lattice position in field direction. This leads to destructive interference and therefore localization.

I therefore also tried to incorporate the electric field into the tight binding model by introducing a diagonal correction term $H_{F_i} = \langle \phi_i | e\boldsymbol{F} \cdot \boldsymbol{r} | \phi_i \rangle$. However, for unresolved reasons this led to different problems. To see the problem, the simulation results for MakeSnake 45/80meV (see main text) morphology with $\nu_0 = 2 \cdot 10^{14} \frac{1}{s}$ without periodic boundary conditions for a $20 \times 20 \times 40$ lattice are shown in **Figure S1** and **S2**.

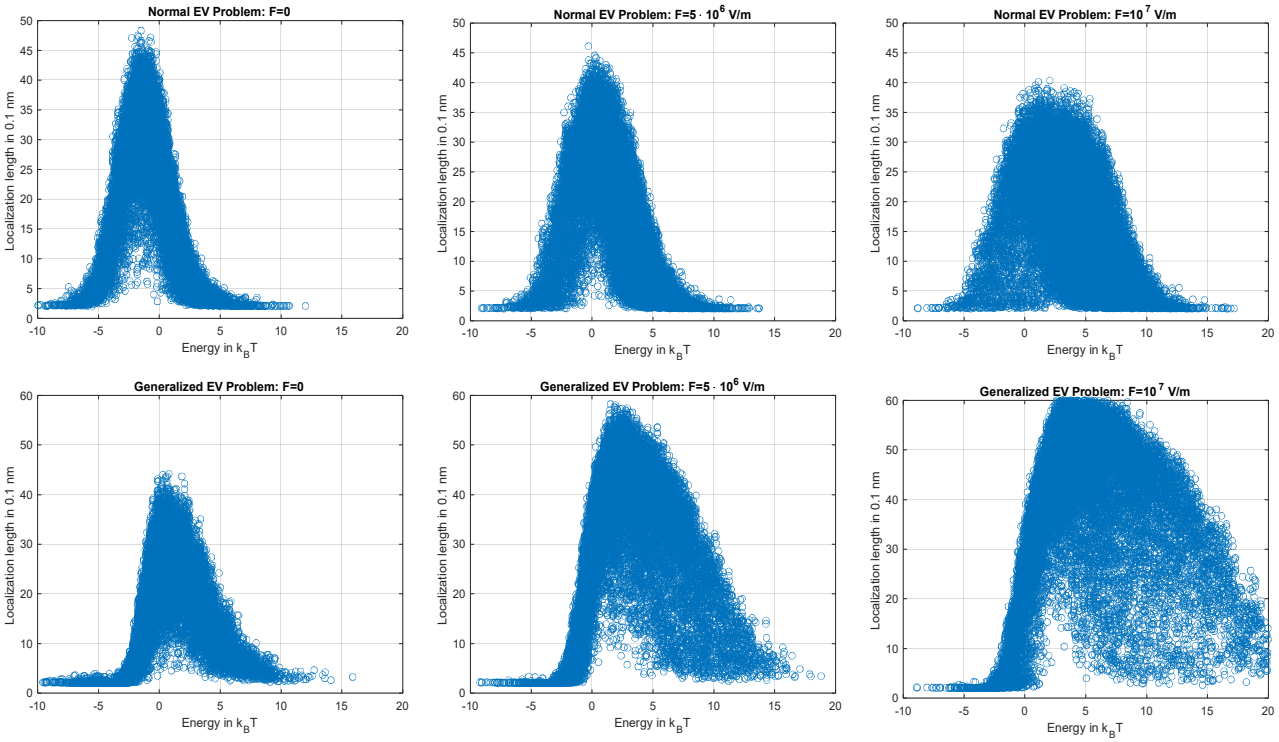

Figure S1 – Localization length distributions for different fields obtained once from the normal Eigenvalue problem (upper graphs) and once from the generalized (lower graphs).

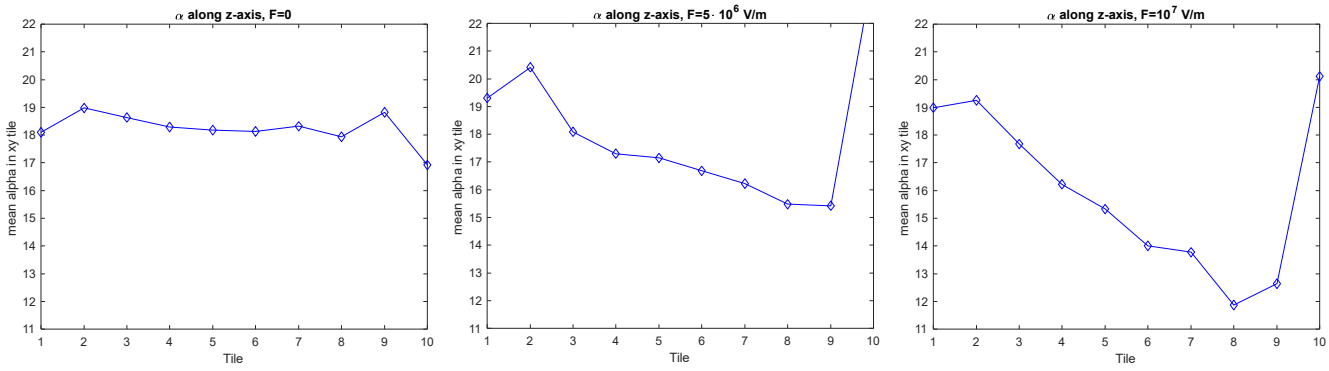

Figure S2 – Mean localization lengths within tiles in direction of the electric field for three different fields.

The first problem is that with increasing field the localization lengths form a spatial gradient in the field direction (Figure S2). This is unexpected and unphysical, since the constant field should act the same everywhere and the material is homogeneous in the sense that there is no spatial gradient. From this behavior one should take the localization length distributions with care, since this artefact can influence the distribution.

Secondly, from Figure S1 one sees that for the localization length obtained via solving the generalized Eigenvalue problem $HV = ESV$ for the Hamiltonian H, the eigenfunctions V and the overlap matrix S, the localization length does increase instead of decrease. At the same time, solving the Hamiltonian via the normal Eigenvalue problem $HV = EV$, one indeed gets a limited decrease of about 10% from zero field to $F = 10^7\ V/m$. While the generalized Eigenvalue problem should be the correct way to solve the problem it gives the opposite effect than expected from Stark localization. Unfortunately, the time was not sufficient to explore this problem further and therefore this remains an open question for future research.

Besides this problematic, one could also ask the question whether the electric field would change the wavefunction form. For this purpose, the wavefunctions of the aforementioned morphology were analyzed by fitting ellipsoids to them using PCA as described in the Theoretical Background. The anisotropy of an ellipsoid with main axes $\boldsymbol{n}_1, \boldsymbol{n}_2, \boldsymbol{n}_3$ and

corresponding axis lengths $\lambda_1, \lambda_2, \lambda_3$ can be described as a scalar from zero to one with zero meaning completely isotropic and one completely anisotropic with the following formula[103,104]

$$s = \frac{3}{2} \cdot \frac{\sum_i \lambda_i^4}{(\sum_i \lambda_i^2)^2} - \frac{1}{2} \tag{S1}$$

Arranging the results for all wavefunctions in histograms for different fields, one obtains **Figure S3**. From this, no significant influence of the electric field on the wavefunction anisotropy can be observed. Therefore, one can conclude that the Stark localization acts isotropic on the wavefunctions. A similar approach can be taken to obtain the global anisotropy of the material. Hereby, one needs calculate the gyration tensor[103,104] of all axes of all wavefunctions and diagonalize it

$$Q = \frac{1}{3N} \sum_{i=1}^{N} \sum_{j=1}^{3} \boldsymbol{n_j^i} \cdot \boldsymbol{n_j^{iT}} \tag{S2}$$

If the eigenvalues of Q are $\lambda_1, \lambda_2, \lambda_3$, then the global anisotropy can again be calculated via Equ. (S1). Evaluating this quantity here for different fields, one also does not obtain any changes and the global anisotropy is in every case basically zero.

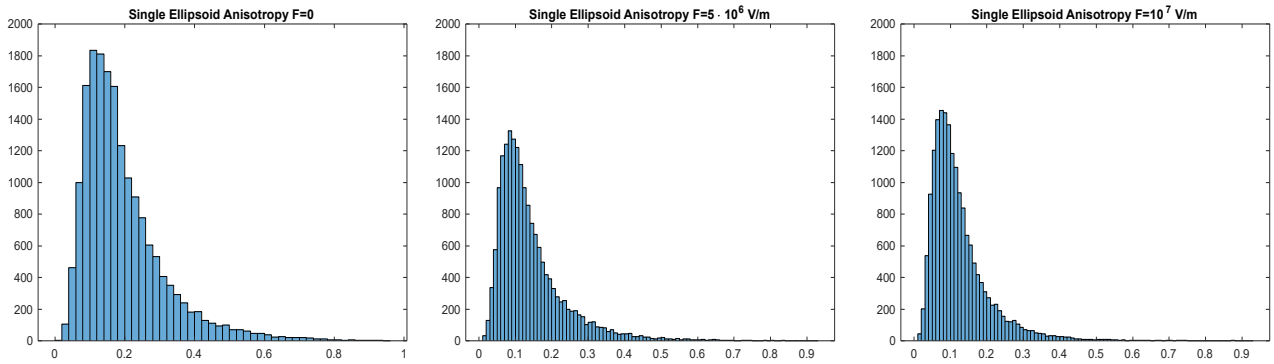

Figure S3 – Histograms of wavefunction anisotropies for different fields. The x-value zero means isotropic, the value one means completely anisotropic.

Comparison of Localization Measures

In the Theoretical Background the idea of a generalized IPR was presented that uses Voronoi tessellation. Here shortly, the two different models (the one used in this thesis and the proposed generalization) are compared for the 8mer morphology. The result is shown in **Figure S4**.

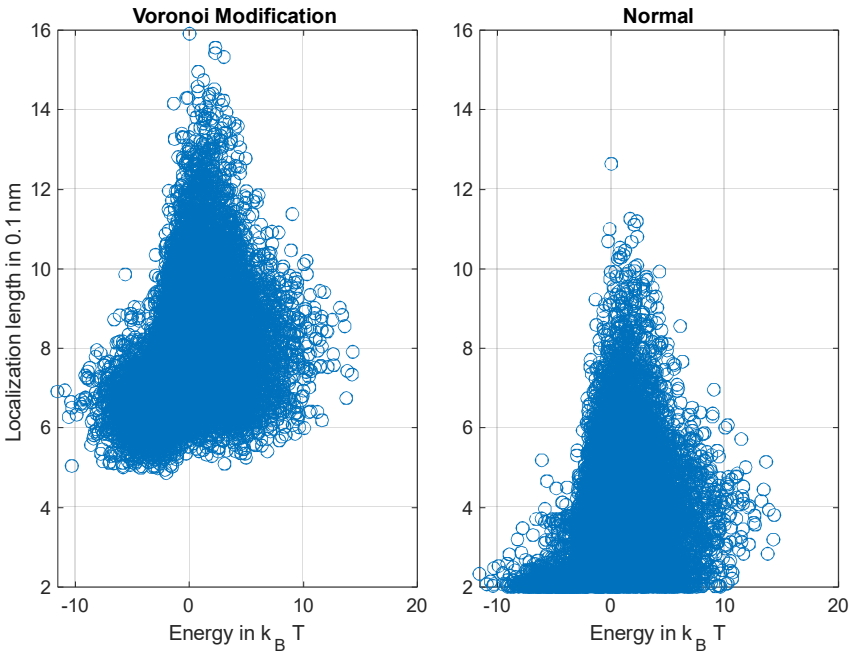

Figure S4 – Comparison of Localization length distributions using the IPR with the Voronoi modification (left) and the model used in this thesis (right).

One can see that apart from a shift upwards, the modification has a similar form of distribution as the localization length distribution obtained via the model used in this thesis. The modification therefore seems to predict higher localization lengths, but one should bear in mind that in this modification no shift was performed to model the physically lowest localization length as the orbital localization instead of some inter-site distance.

Powerfactors

The powerfactors $PF = S^2\sigma$ for each considered morphology is shown in the following **Figure S5**.

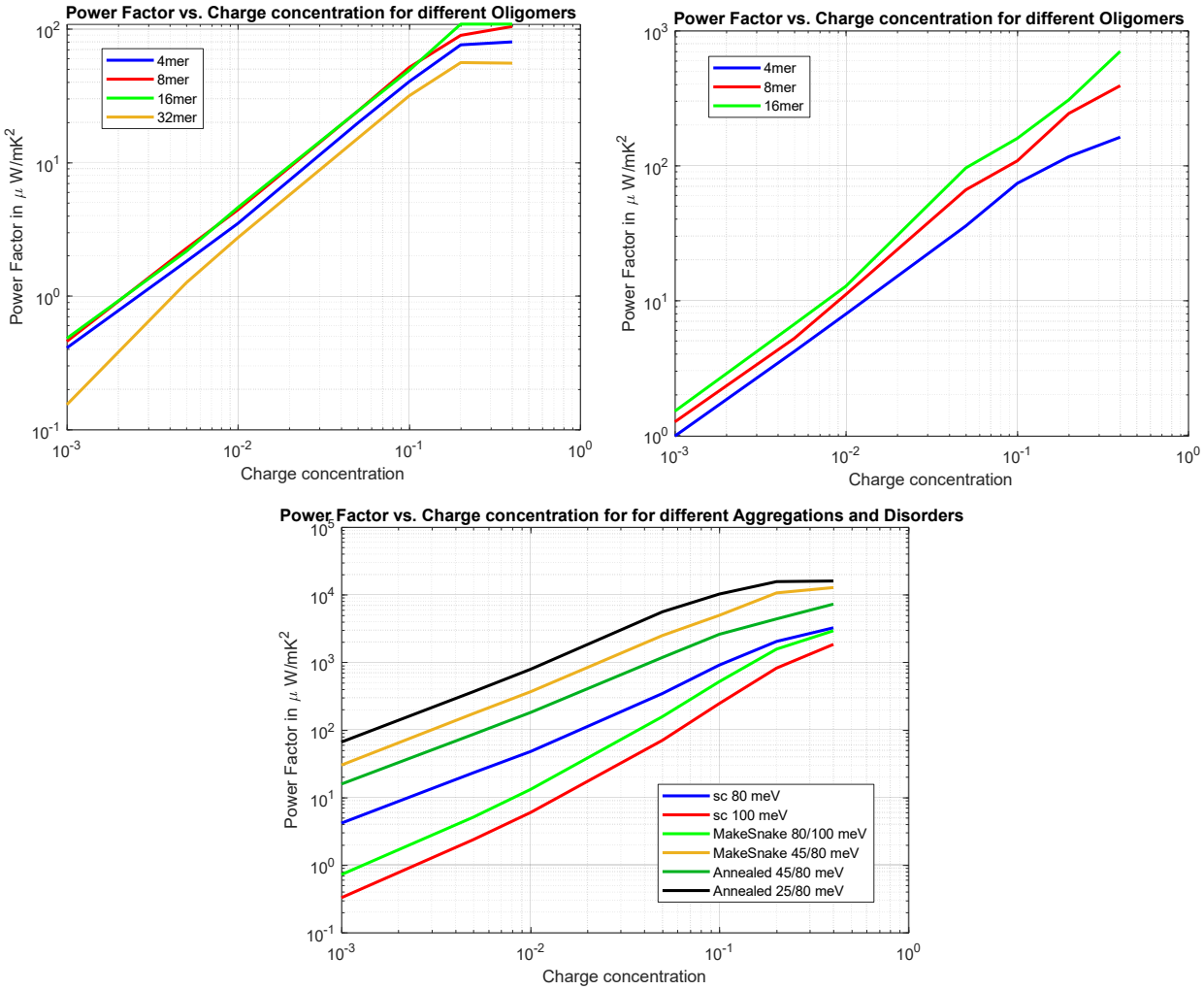

Figure S5 – Powerfactors of the different considered morphologies. Upper left: MD morphologies for $f_{ich} = 1.3$. Upper right: MD morphologies for $f_{ich} = 10$. Lower: Powerfactors for the different simplified morphologies.

Generally, it can be seen that the saturation of the powerfactor sets in for a little bit higher charge carrier concentration than at the sometimes obtained $c_f = 10\%$. The picture here is a little bit more differentiated. Higher disorder leads to a saturation at higher charge carrier concentrations. As outlined in the main text, this is due to the low-lying transport energy that reaches saturation only at higher charge carrier concentrations. However, it should also be

noted that in these simulations no Coulomb interactions due to counter-ions were considered. Comparing the MD morphologies, the increased intra-chain coupling leads to lower Seebeck coefficient but has a higher influence on the conductivity such that the effect gets overcompensated for the resulting powerfactor. Hence, the powerfactor is increased for enhanced intra-chain coupling for the same morphology. Experimentally this could be achieved by enhanced delocalization of the polymer backbone, e.g. by high aromaticity. However, chemical modifications can lead to substantial morphological and other modifications of physical parameters, so this design-rule should be taken with care. Comparing the simplified and partially aggregated morphologies, the differences in the powerfactor arise almost solely from the differences in conductivity, since the Seebeck coefficient is only marginally affected due to the reasons outlined in the main text.

Temperature Dependence Fit Parameters

For the fit of the temperature curves, the fit function $\sigma = \sigma_0 \cdot \exp\left(-\left(\frac{T_0}{T}\right)^{\beta}\right)$ was used. The following Table S1 gives the obtained essential fit parameters, the characteristic temperature T_0 and the temperature exponent β.

Table S1 – Fit parameters of the temperature dependence of the conductivity.

Morphology	T_0 in K	β
16mer $f_{ich} = 10$	645 ± 4550	0.99 ± 1.5
8mer $f_{ich} = 10$	750 ± 5418	0.94 ± 1.3
4mer $f_{ich} = 10$	$(5.5 \pm 14.2) \cdot 10^6$	0.22 ± 1.0
32mer $f_{ich} = 1.3$	1394 ± 11586	0.97 ± 1.5
16mer $f_{ich} = 1.3$	772 ± 2372	1.35 ± 0.9
8mer $f_{ich} = 1.3$	846 ± 2043	1.27 ± 0.5
4mer $f_{ich} = 1.3$	663 ± 1357	1.5 ± 0.5
Annealed 45/80	707 ± 813	1.52 ± 0.2
MakeSnake 80/100	2123 ± 6783	0.97 ± 0.7
Annealed 25/80	576 ± 702	1.8 ± 0.2
sc 80	1406 ± 1812	1.1 ± 0.3
sc 100	14549 ± 22534	0.6 ± 0.3
MakeSnake 45/80	811 ± 555	1.4 ± 0.1

While the fitted lines fit reasonable, the errors on the fit parameters are significant. This is due to the small temperature range and the flexibility of the fit function. However, the temperature exponent lies within a reasonable range considering the fitting errors and the exact functional form is not crucial for the analyses in the main text.

GESAMTFAKULTÄT FÜR MATHEMATIK,
INGENIEUR- UND NATURWISSENSCHAFTEN

COMBINED FACULTY OF MATHEMATICS,
ENGINEERING AND NATURAL SCIENCES

RUPRECHT-KARLS-
UNIVERSITÄT
HEIDELBERG

Eidesstattliche Versicherung gemäß § 8 der Promotionsordnung für die Gesamtfakultät für Mathematik, Ingenieur- und Naturwissenschaften der Universität Heidelberg / Sworn Affidavit according to § 8 of the doctoral degree regulations of the Combined Faculty of Mathematics, Engineering and Natural Sciences at the Heidelberg University

1. Bei der eingereichten Dissertation zu dem Thema / The thesis I have submitted entitled

   Morphology- and Delocalization-Based Charge Transport Simulations Combining Tight Binding Modelling and Kinetic Monte Carlo Simulations

   handelt es sich um meine eigenständig erbrachte Leistung / is my own work.

2. Ich habe nur die angegebenen Quellen und Hilfsmittel benutzt und mich keiner unzulässigen Hilfe Dritter bedient. Insbesondere habe ich wörtlich oder sinngemäß aus anderen Werken übernommene Inhalte als solche kenntlich gemacht. / I have only used the sources indicated and have not made unauthorised use of services of a third party. Where the work of others has been quoted or reproduced, the source is always given.

3. Die Arbeit oder Teile davon habe ich ~~wie folgt~~/bislang nicht[1)] an einer Hochschule des In- oder Auslands als Bestandteil einer Prüfungs- oder Qualifikationsleistung vorgelegt. / I have not yet/have already[1)] presented this thesis or parts thereof to a university as part of an examination or degree.

   Titel der Arbeit / Title of the thesis:……

   Hochschule und Jahr / University and year:……

   Art der Prüfungs- oder Qualifikationsleistung / Type of examination or degree:……

4. Die Richtigkeit der vorstehenden Erklärungen bestätige ich. / I confirm that the declarations made above are correct.

5. Die Bedeutung der eidesstattlichen Versicherung und die strafrechtlichen Folgen einer unrichtigen oder unvollständigen eidesstattlichen Versicherung sind mir bekannt. / I am aware of the importance of a sworn affidavit and the criminal prosecution in case of a false or incomplete affidavit

Ich versichere an Eides statt, dass ich nach bestem Wissen die reine Wahrheit erklärt und nichts verschwiegen habe. / I affirm that the above is the absolute truth to the best of my knowledge and that I have not concealed anything.

…….. ……

Ort und Datum / Place and date — Unterschrift / Signature

[1)] Nicht Zutreffendes streichen. Bei Bejahung sind anzugeben: der Titel der andernorts vorgelegten Arbeit, die Hochschule, das Jahr der Vorlage und die Art der Prüfungs- oder Qualifikationsleistung. / Please cross out what is not applicable. If applicable, please provide: the title of the thesis that was presented elsewhere, the name of the university, the year of presentation and the type of examination or degree.

The German text is legally binding.